MICROCOPY RESOLUTION TEST CHART

NATIONAL BUREAU OF STANDARDS-1963-A

THE EFFECTS OF STREAMWISE CONCAVE CURVATURE
ON TURBULENT BOUNDRY LAYER STRUCTURE

AD A122303

by

Albert H. Jeans and James P. Johnston

Report MD-40

DTIC
ELECTE
DEC 1 0 1982

A

Thermosciences Division
Department of Mechanical Engineering
Stanford University
Stanford, California

June 1982

FILE COPY

92 12 10 023

REPORT DOCUMENTATION PAGE	READ INSTRUCTIONS BEFORE COMPLETING FORM

1. REPORT NUMBER	2. GOVT ACCESSION NO.	3. RECIPIENT'S CATALOG NUMBER
AFOSR-TR- 82-1015	AD-A111,303	

4. TITLE (and Subtitle)	5. TYPE OF REPORT & PERIOD COVERED
THE EFFECTS OF STREAMWISE CONCAVE CURVATURE ON TURBULENT BOUNDARY LAYER STRUCTURE	INTERIM
	6. PERFORMING ORG. REPORT NUMBER

7. AUTHOR(s)	8. CONTRACT OR GRANT NUMBER(s)
A H JEANS J P JOHNSTON	F49620-80-C-0010

Massachusetts Inst of Tech Cambridge, MA 02139

10. PROGRAM ELEMENT, PROJECT, TASK AREA & WORK UNIT NUMBERS
61102F 2307/A4

11. CONTROLLING OFFICE NAME AND ADDRESS	12. REPORT DATE
AIR FORCE OFFICE OF SCIENTIFIC RESEARCH/NA BOLLING AFB, DC 20332	June 1982
	13. NUMBER OF PAGES 157

14. MONITORING AGENCY NAME & ADDRESS(if different from Controlling Office)	15. SECURITY CLASS. (of this report)
	UNCLASSIFIED
	15a. DECLASSIFICATION/DOWNGRADING SCHEDULE

16. DISTRIBUTION STATEMENT (of this Report)

Approved for Public Release; Distribution Unlimited.

17. DISTRIBUTION STATEMENT (of the abstract entered in Block 20, if different from Report)

18. SUPPLEMENTARY NOTES

19. KEY WORDS (Continue on reverse side if necessary and identify by block number)

TURBULENT STRUCTURE
CONCAVE CURVATURE
BOUNDARY LAYER
FLOW VISUALIZATION

20. ABSTRACT (Continue on reverse side if necessary and identify by block number)

Concave curvature has a relatively large, unpredictable effect on turbulent boundary layers. Some, but not all previous studies suggest that a large-scale, stationary array of counter-rotating vortices exists within the turbulent boundary layer on a concave wall. The objective of the present study was to obtain a qualitative model of the flow field in order to increase our understanding of the underlying physics. A large free-surface water channel was constructed in order to perform a visual study of the flow. Streamwise components of mean velocity and turbulence intensity were measured using

DD FORM 1473 EDITION OF 1 NOV 65 IS OBSOLETE
1 JAN 73

A hot film anemometer. The upsteam boundary was spanwise uniform with a a momentum thickness to radius of curvature of 0.05. Compared to flat wall flow, large-scale, randomly distributed sweeps and ejections were seen in the boundary layer on the concave wall. The sweeps appear to suppress the normal mechanism for turbulence production near the wall by inhibiting the bursting process. The ejections appear to enhance turbulence production in the outer layers as the low speed fluid convected from regions near the wall interacts with the higher speed fluid farther out. The large-scale structures did not occur at fixed spanwise locations, and could not be called roll cells or vortices.

THE EFFECTS OF STREAMWISE CONCAVE CURVATURE

ON TURBULENT BOUNDARY LAYER STRUCTURE

by

Albert H. Jeans

and

James P. Johnston

Report MD-40

Accession For
NTIS GRA&I ☑
DTIC TAB ☐
Unannounced ☐
Justification_____

Distribution/
Availability Codes
Dist | Avail and/or
     | Special
A

Heat Transfer and Turbulence Mechanics Group
Thermosciences Division
Department of Mechanical Engineering
Stanford University
Stanford, California 94305

June 1982

Acknowledgments

ABSTRACT

Concave curvature has a relatively large, unpredictable, effect on tur-
bulent boundary layers. Past studies of turbulent boundary layers on
concave walls have emphasized quantitative, single-point measurements
which have yielded similar information about the general features of
this flow. For example, skin friction and turbulence levels increase
when the boundary layer goes from a flat wall to a concave wall. How-
ever, there is disagreement over the cause of these results. Many
recent studies have supported the idea that a large-scale array of
counter-rotating vortices exists within the concave turbulent boundary
layer, similar to the Taylor-Görtler vortices in laminar boundary layers
on concave walls. Some investigators have found stationary, large-scale
spanwise variations in mean velocity and skin friction. However, in
other studies these large-scale variations were not found. Even among
those who did find stationary, large-scale variations, there are some
inconsistencies in the relative size and spacing of the variations com-
pared with the boundary layer thickness and the radius of curvature, the
two most reasonable length scales. Furthermore, the effects of concave
curvature on the basic elements (e.g. streaks and bursts) of the bound-
ary layer structure have not been studied. At the start of the present
study, no adequate picture of the overall flow field existed.

The objective of the present study was to obtain an adequate qualita-
tive model of the flow in order to increase our understanding of the

underlying physics and thereby guide future work. A large, free-surface
water channel was constructed in order to perform visual and quantita-
tive studies of the flow. The size and design of this water channel
enabled us to perform detailed, extensive, visual surveys of the flow
field by using dye injected through wall slots and by marking the flow
with hydrogen bubbles. Profiles of mean velocity and turbulence inten-
sity were also obtained.

Large-scale structures consisting of randomly distributed ejections
and sweeps were found to dominate the boundary layer on the concave
wall. The sweeps appear to suppress turbulence production near the wall
by inhibiting the normal flat surface bursting process. The ejections
appear to enhance turbulence production in the outer portion of the
boundary layer as the lower speed fluid convected from regions near the
wall interacts with the higher speed fluid farther out.

Interpretation of the flow visualization was aided by a computer
simulation of a simpler, hypothetical flow field. The results of the
simulation helped qualify the visual observations and provided a basis
on which to build a more realistic picture of the flow field.

The streamwise velocity was measured using a computer-controlled hot
film anemometer. Profiles of mean velocity and turbulence intensity show
the flow upstream of the start of curvature to be a normal turbulent
boundary layer with acceptable spanwise uniformity and a momentum thick-
ness Reynolds number of 1300. Spanwise surveys in the curve and in the
recovery region downstream of curvature show no evidence that the
large-scale structures observed visually tend to occur in preferred

locations. Boundary layer profiles reveal a fuller mean velocity profile and an increase in turbulence intensity, especially in the outer flow. Although logarithmic regions are evident in profiles taken in the curved section, these "quasi-logarithmic" zones appear to be unrelated to the usual Law of the Wall and migrate away from the wall as the flow develops.

Additional insight into the flow physics was provided by visualizing a transitional boundary layer along the concave wall. Taylor-Görtler vortices were observed along with a secondary instability in the form of a horseshoe vortex street. These observations demonstrated a possible mechanism for turbulence production in the outer flow for the case of turbulent boundary layers.

As a result of this study, a qualitative picture of the flow field is proposed which accounts for the observed characteristics of turbulent boundary layers on concave walls.

CONTENTS

LIST OF FIGURES

LIST OF TABLES

NOMENCLATURE

c_f skin friction coefficient, $\dfrac{\tau_w}{\frac{1}{2}\rho U_0{}^2}$

h core height of simulated vortices

H shape factor, θ/δ, or alternately channel or tunnel height (dimension in z direction)

r radial coordinate, $R_0 - y$

R radius of curvature

R_0 radius of curvature of concave test wall

Re_t momentum thickness Reynolds number, $\dfrac{\theta U_0}{\nu}$

u velocity component in the x direction

u' fluctuating part of u, $u-U$

u^+ non-dimensional velocity, U/u^*

u^* friction velocity , $\sqrt{\dfrac{\tau_w}{\rho}}$

U time mean of u

$\langle U \rangle$ sampled mean of u

U_0 freestream velocity

U_n radius normalized mean velocity, $U\left(\dfrac{R_0 - y}{R_0}\right)$

U_{pw} potential velocity at the wall

v velocity component in the y direction

w velocity component in the z direction

W   channel or tunnel width (dimension in the y direction)

x   streamwise or longitudinal coordinate along test wall

y   coordinate normal to test wall, y=0 at test surface

y^+ non-dimensional distance from wall, $\dfrac{yu^*}{\nu}$

z   transverse or spanwise coordinate

δ boundary layer thickness

δ^* displacement thickness, $\displaystyle\int_0^\delta \left(1 - \frac{U}{U_0}\right)dy$

κ Von Karman constant

λ spanwise spacing of streaks

λ^+ non-dimensional streak spacing, $\dfrac{\lambda u^*}{\nu}$

Λ wavelength of large-scale variations in flow properties

μ viscosity

ν kinematic viscosity, μ/ρ

Π Coles profile parameter, $1-\kappa\dfrac{\delta^* U_0}{\delta u^*}$

ρ density

τ_W wall shear stress

θ momentum thickness, $\displaystyle\int_0^\delta \frac{U}{U_0}\left(1 - \frac{U}{U_0}\right)dy$

GLOSSARY

As the study of the structure of turbulent flows has progressed, many words and phrases have evolved to describe various elements or characteristics of the flow. Obviously, clear definitions are needed in order to communicate the particular attributes of a given flow. What follows is a glossary of some of the terms used in the present work. Many of the definitions follow those of Kline & Falco (1979).

breakdown | An abrupt event in which the streak oscillations terminate in the formation of a large region containing a wide range of small scales.

bursting | The set of processes beginning with the lifting of streaks and terminating at the end of the mixing region.

coherent structure or eddy | A confined region in space and time in which definite phase relationships exist among flow variables.

ejection or outflow | A coherent structure moving away from a wall.

large-scale | Having a size of the order of the boundary layer thickness.

longitudinal vortex | A region of fluid, highly extended (aspect ratio greater than 10:1) in the flow direction, with relatively high streamwise vorticity. Typical fluid particles near the core perform several revolutions during their stay within the vortex.

medium-scale	Having a size in wall layer (y^+) coordinates between 50 and 300.
mixing region	Region after a breakdown in which chaotic motions affect a large propagating region.
roll cell	A large-scale, slowly revolving body of fluid without a strong vortex-like core.
small-scale	Having a size in wall layer (y^+) coordinates between 1 and 10.
streak	A low-speed (relative to the mean) region in the viscous sublayer, highly extended (aspect ratio greater than 10:1) in the flow direction.
streak lifting	Outward movement of fluid in a streak to a point outside viscous sublayer.
sweep or inflow	Large-scale inward (towards the wall) motion of faster moving fluid, producing local acceleration in the flow field.
Taylor-Görtler vortices	A stationary array of large-scale, counterrotating, longitudinal vortices lying next to a wall whose driving mechanism is a centrifugal instability due to flow curvature.
viscous sublayer or wall layer	Region where y^+ is less than 7-10.

Chapter I

INTRODUCTION

1.1 GENERAL MOTIVATION

Surfaces with concave curvature occur in many flow situations of practical importance. A concave surface is one in which the center of curvature lies outside of the body, in the flow, as shown in Fig. 1. Some examples are shown in Fig. 2. They include the pressure sides of turbine blades or wings and portions of ducts and nozzles. Often the boundary layers on such surfaces are turbulent. Previous studies, including So & Mellor (1975), Meroney & Bradshaw (1975), and Hoffmann & Bradshaw (1981), have found large local variations in boundary layer parameters; spanwise variations of 20% in skin friction and 100% in momentum thickness, even for cases of mild curvature (δ/R as low as 1%), are not uncommon. The more efficient design of concave surfaces has been hampered by our inability to predict the large effects concave curvature has on turbulent boundary layers. The lack of adequate predictive methods is due, in part, to a gap in our understanding of the physics of the flow.

The work described here is part of a larger, ongoing program at Stanford to study and gain a better understanding of the effects of curvature on the hydrodynamics and heat transfer in turbulent boundary layers. The study of turbulent boundary layers on convex walls was well advanced at the time the current study was undertaken. Simon & Moffat

Figure 1: Geometry of a concave surface.

Figure 2: Examples of flows with concave curvature.
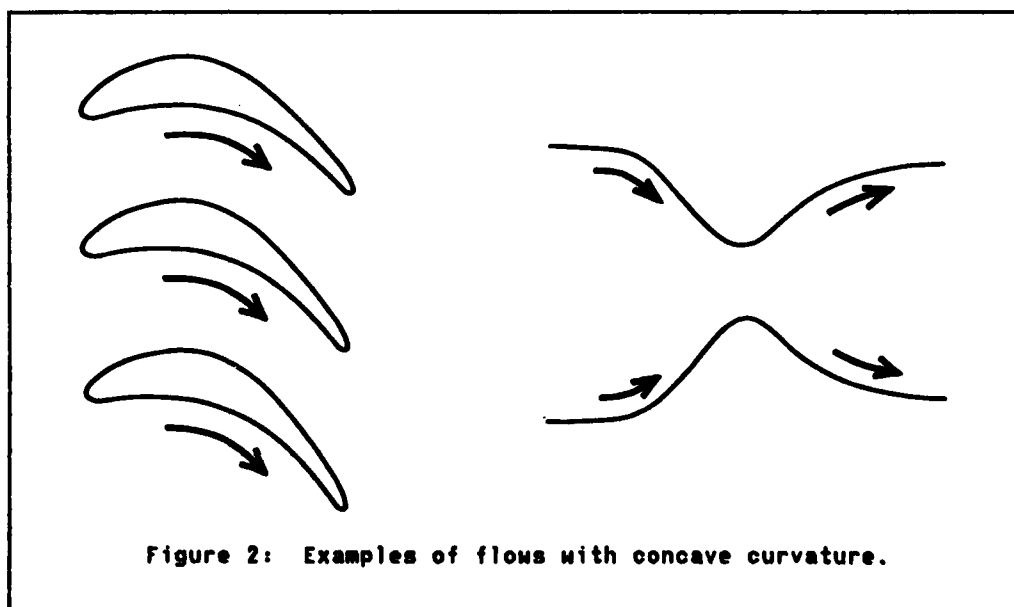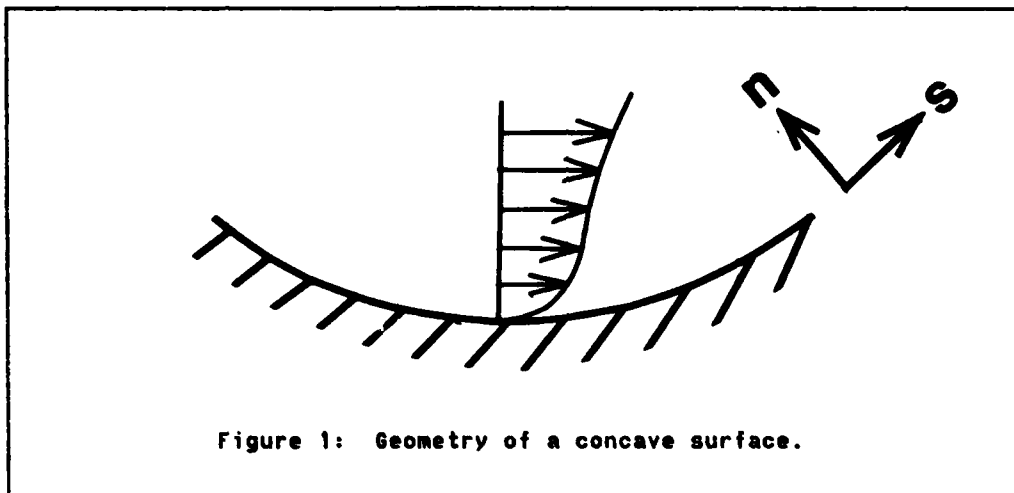
(1979) and Gillis & Johnston (1980) had taken detailed heat transfer and hydrodynamic measurements in boundary layers on convex surfaces. They had also successfully modelled the effects of convex wall curvature by

suitably modifying the boundary layer code STAN5. No previous work on concave walls had been done at Stanford. Related studies had been done on the effects of system rotation on turbulent channel flow by Johnston et al (1972).

A review of the literature revealed a lack of direct visual observation of turbulent flows over concave walls. Physical models of the flow structure were limited to sketchy analogies between this flow and the corresponding laminar flow with its Taylor-Görtler longitudinal vortices. The effects of concave curvature on the streaks and bursts found in normal flat plate boundary layers were unknown. Yet, the quantitative data showed a need for an overall picture of the flow field in order to clarify the interpretation of the available results. We therefore decided to concentrate on visual studies in order to develop a qualitative model of the flow structure. This qualitative model can then be used to guide later, more quantitative studies and thus, ultimately, to aid attempts to predict the flow. These steps: (i) a qualitative model from visual studies as a basis for (ii) the design of quantitative experiments for use in (iii) a model for use in prediction have proven to be fruitful in the study of many complex turbulent flows.

1.2 LITERATURE SURVEY

Until 1970, relatively little research had been done on the effects of concave curvature on turbulent boundary layers. However, the last decade has seen a large increase in work in this field. Table 1 presents a summary of past work, with an emphasis on presenting and comparing the structural characteristics of the flow found by different investigators.

- 3 -

TABLE 1

Past studies of turbulent flow over concave surfaces.

	Date	Re_θ	H/W	H/δ	δ/R	Var.	Λ
Wilcken	1930	4600-7400	6.5-6.8	13-14	0.10-0.25	none	
Wattendorf[1]	1935	5000	18.0	36	0.10	none	
Eskinazi & Yeh[1]	1956	6900	15.5	31	0.05	none	
Tani	1962	11300	2.0[3]	120	0.002	N/R	const.
Patel	1968	6200	5.0	28	0.06	50% dp	26_θ
Johnston, Halleen, & Lezius[2]	1972	700-2100	2.8	6	0-0.25	N/R	W
Ellis & Joubert[1]	1974	?	13.2	26	0.016-0.08	N/R	
So & Mellor	1975	4300	8.0[4]	40	0.067	35% u, 100% δ, 100% θ	irregular
Meroney & Bradshaw	1975	7800	6.0	33	0.008	20% c_f, 30% δ, 100% θ	δ
Ramaprian & Shivaprasad	1977	3600	2.5	76	0.013	none	
Hunt & Joubert[1]	1979	6000	13.2[3]	26	0.02	5% u	.8W-1.6W
Smits, Young, & Bradshaw	1979	6000	6.0	36	0.08	20% c_f, 100% θ	26
Rao	1979	1500 3700 6000	1.5[4] 1.5[4] 1.5[4]	23 13 6	0.024 0.054 0.078	65% u 45% u 20% u	const. >6 max.
Shizawa et al	1981	1080 1360	4.0 6.0	20 70	0.039 0.017	100% θ, 65% p 100% θ, 35% p	20_θ 20_θ
Hoffmann & Bradshaw[5]	1981	4000-6000	6.0	33	0.008	30% c_f, 50% δ, 100% θ	2.86

Table 1, cont.

Legend:

u = mean velocity
δ = local boundary layer thickness
$δ_o$ = boundary layer thickness at start of curvature
θ = momentum thickness
$Re_θ$ = momentum thickness Reynolds number at start of curvature
c_f = skin friction coefficient
p = total pressure
H = height of channel
W = width of channel
Var. = maximum reported spanwise variation in properties, expressed as peak-to-peak percent of minimum value.

λ = approximate wavelength of spanwise variations
N/R = Observed but no data reported
dp = Preston tube pressure difference

Notes:
[1] Fully developed channel flow. δ = W/2, θ = W/20.
[2] Fully developed rotating channel flow. δ/R = ωδ/U.
[3] Attempt made to minimize streamwise pressure gradient.
[4] Attempt made to minimize secondary flow.
[5] Vortex generators in settling chamber.

- 5 -

Rayleigh (1917) first deduced that flow on concave surfaces, in this case inviscid flow with circular symmetry, is unstable to radial disturbances. He assumed conservation of angular momentum and performed an energy calculation. He considered two lumps of fluid with equal masses, $m_1 = m_2 = m$ moving in circular paths with radii r_1 and r_2. The energy of the two masses is

$$E = \tfrac{1}{2}(m_1 v_1^2 + m_2 v_2^2)$$
$$= \tfrac{1}{2} m(v_1^2 + v_2^2). \tag{1.1}$$

He then interchanged the positions of the two lumps. In the absence of friction, conservation of angular momentum dictates that $vr = k$, a constant, for each lump of fluid. The new velocities for each lump, denoted by $()'$ become

$$v_1' = \frac{k_1}{r_2} \tag{1.2}$$

$$v_2' = \frac{k_2}{r_1}. \tag{1.3}$$

The difference in energy works out to be

$$E' - E = \frac{m}{2}\left\{ \left[k_1^2 \left(\frac{1}{r_2^2} - \frac{1}{r_1^2} \right) \right] + \left[k_2^2 \left(\frac{1}{r_1^2} - \frac{1}{r_2^2} \right) \right] \right\}$$

$$= \frac{m}{2}(k_2^2 - k_1^2)\left(\frac{1}{r_1^2} - \frac{1}{r_2^2} \right). \tag{1.4}$$

Let us arbitrarily choose r_1 to be less than r_2. If $r_1 < r_2$ then the sign of $E' - E$ is the same as $k_2 - k_1$. Three possible cases can be considered:

1. If $k_1 = k_2$ as in potential flow, there is no change in the energy. This is the case of neutral stability.

2. If $k_1 < k_2$ as in the boundary layer on a convex surface, then the energy of the system is increased by the interchange of the two lumps of fluid. Presumably, a system tends to lower its energy state. Hence, if $k_1 < k_2$, then the two lumps resist being interchanged and the system is stable.

3. If $k_1 > k_2$ as in the boundary layer on a concave surface, then system can lower its energy by interchanging the two fluid elements. The system is therefore unstable.

Although Rayleigh's analysis provides a rationale for anticipating instabilities, it is far too limited to be useful in actual flows, where viscosity plays an important role.

Early experimental studies by Wilcken (1930) and Wattendorf (1935) obtained only mean pressure and velocity measurements in curved channels. From these measurements mixing lengths and eddy viscosities were calculated. Wilcken investigated turbulent boundary layers developing on concave walls and found that the mixing length he calculated was about 4 times that for a comparable flat plate. Wattendorf, using fully developed channel flow, also found an increase in mixing on the concave wall as well as a midchannel profile which reached a constant angular momentum distribution, another sign of vigourous mixing. Higher skin friction is also evident from an examination of his velocity profiles close to the concave wall.

After 1935, published experimental work on curved turbulent flows ceased for about two decades. In the meantime, Görtler (1940, 1954)
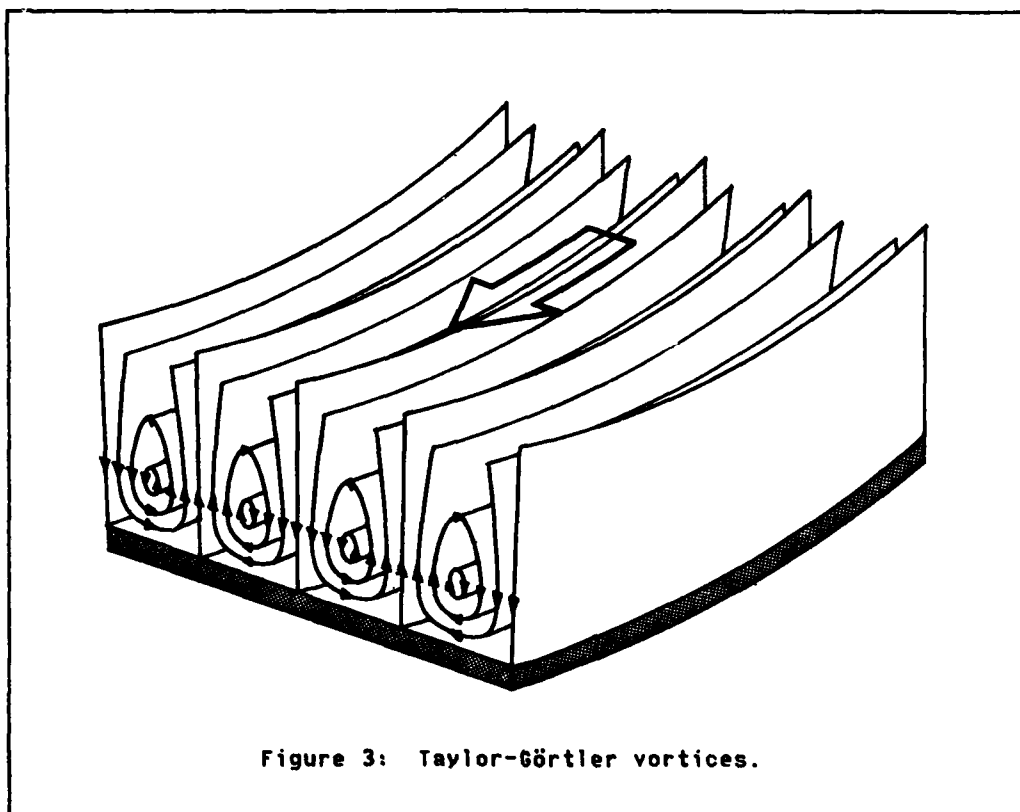
Figure 3: Taylor-Görtler vortices.

performed a viscous stability analysis of laminar boundary layers on

concave walls.   He superimposed small disturbances in the form of

counter-rotating longitudinal vortices (as shown in Fig. 3) on the mean

flow, linearized the equations, and solved the resulting eigenvalue

problem. He found that vortices with a wide range of wavelengths could

be amplified and that the parameter

$$G = Re_t \sqrt{\frac{2\theta}{R}}$$ \hfill (1.5)

governed the onset of amplification. The vortices have since been called

Taylor-Görtler vortices in recognition of Görtler's work on an

adaptation of the problem of flow between concentric cylinders first solved by G. I. Taylor. It was another 10 years before Taylor-Görtler vortices were actually observed by Gregory & Walker (1950).

Eskinazi & Yeh (1956) resumed the experimental investigation of fully developed channel flow. Using hot wire anemometers, they measured mean and turbulent quantities as well as spectra. They obtained good general agreement with Wattendorf's results. Their data and considerations of the turbulent energy equations showed that turbulent fluctuations are amplified on the concave wall. As with previous experimental research- ers, no large-scale disturbances were expected or looked for.

Tani (1962) is generally credited with being the first to find evi- dence of large-scale structures in a turbulent boundary layer on a con- cave wall. Stationary, spanwise periodic variations in velocity were detected near the surface of a test wall with mild curvature inserted in a wind tunnel. Unfortunately the investigation was very limited, and little was done to elaborate on the nature of the structures. An attempt was made by Tani to apply the Görtler stability parameter (see above) to the turbulent flow by using an eddy viscosity rather than the kinematic viscosity.

Patel (1968) also made limited measurements on a concave wall. He detected large-scale, stationary variations in the pressure as he tra- versed the span with a Preston tube. Variations as high as 50% (peak-to-peak) were reported with a spanwise wavelength about twice the initial boundary layer thickness. In addition, the same spanwise profile was present at two streamwise locations, 135° and 173° into the curve.

Studies by Johnston et al (1972) investigated the qualitatively similar situation of flow in a rotating channel. A rectangular channel with nominally two-dimensional, fully-developed duct flow was rotated about an axis outside the channel and perpendicular to the flow. Flow visualization using dyes and hydrogen bubbles revealed large-scale motions on the destabilized side which penetrated far into the core. The positions of the "roll cells", as they were called, were not fixed, but varied with time. The "short time" average roll cell wavelength was comparable to the channel width.

Bradshaw (1973) did a comprehensive review of all previous work pertaining to the effects of streamline curvature on turbulence. Among the many topics covered was the analogy between certain configurations of laminar curved and buoyant flows. For turbulent flows, Bradshaw presented the following argument: A fluid element in a buoyant flow with a density ρ' higher than the mean density ρ experiences a vertical acceleration of $-\rho'g/\rho$. A fluid element in a curved flow with a velocity u higher than the mean velocity U experiences an outward acceleration (in excess of the acceleration attributable to curvature of the mean flow) of

$$\frac{[(U+u)^2-U^2]}{R} \approx \frac{2Uu}{r}. \tag{1.6}$$

The connection between the two situations comes when one notes that in a variable density shear layer the correlation coefficient between density and velocity variations has been experimentally found to be as high as 0.9 [D. S. Johnston (1959)]. Hence, in both cases the fluid element experiences an excess body force proportional to the fluctuating

- 10 -

property, and the correlation data insures that the results will be comparable.

In the mid-seventies, there was a dramatic increase in the amount of research being done on concave flows. Ellis & Joubert (1974) mentioned the persistence of some spanwise velocity variations in their study of developing turbulent boundary layers. The variations could not be eliminated despite "gross duct distortions and deliberate attempts to induce asymmetric flow." However, detailed investigation of the variations was not undertaken.

So & Mellor (1975) performed a careful study in which they controlled secondary flows due to end wall boundary layers by using wall jets. They also tailored the shape of the convex wall to minimize the streamwise pressure gradient on the concave wall. A stationary pattern of velocity variations was found; velocities at 30° of turning varied by up to 35% (peak-to-peak). However, there was no well-defined periodicity in the variations. By the 100° mark the spanwise variations in mean velocity had settled down to 8%. Boundary layer thickness was reported to vary by a factor of 2 over a spanwise distance of half the minimum local boundary layer thickness at both the 30° and 100° stations. Traverses of turbulence quantities were made at the spanwise locations of mean velocity maxima and minima. Measurements of streamwise turbulence intensity showed a peak at $y/\delta=.4$ at 30° for all spanwise locations. A smaller peak at $y/\delta=.8$, was also detected but only at the mean velocity minima locations at 110°. Other turbulence quantities also indicated increased turbulent activity at positions away from the wall. Skin friction was

- 11 -

inferred from Clauser plots. The authors expressed some reservations regarding the validity of the technique in the regions of curved flow since the usual logarithmic regions in the mean velocity profiles were almost nonexistent in the curved wall profiles. c_f was found to increase with streamwise distance along the concave wall with no significant spanwise variation. A value of $c_f=0.0054$ was reported at 110° (compared with $c_f=0.00351$ upstream of the curve).

At the time So & Mellor were doing their studies, Meroney & Bradshaw (1975) performed a similar study using a constant width channel with mild ($\delta/R=.008$) curvature. They too found irregular but repeatable large-scale variations in the spanwise velocity profile and 35% variations in boundary layer thickness across the wavelength of a typical "roll". They estimated that the average wavelength of the rolls was close to the local average boundary layer thickness. The stability and irregularity of the roll positions was attributed to upstream flow conditions. Turbulence intensity measurements again showed increased activity away from the wall although the peaks found by So & Mellor were absent.

Ramaprian & Shivaprasad (1977) also studied the case of mild curvature, but they found no spanwise variations in flow properties. The authors admitted the low aspect ratio of their apparatus (2.5) may have inhibited the growth of large-scale structures.

Fully-developed curved duct flow was investigated by Hunt & Joubert (1979). The radius of curvature was relatively large in order to obtain a "perturbed straight flow". Nevertheless, careful measurement of the

velocities in the core revealed a stationary structure which they attributed to longitudinal vortices (the velocity variations were less than 5%). The wavelength of the main structure was approximately 1.6W (W=channel width), but measurements of friction velocity indicated weaker structures in between the main ones, so the wavelength could have been closer to 0.8W.

Smits, Young, & Bradshaw (1979) studied the effects of short regions of high curvature where the flow was impulsively turned 20° and 30°. They found a pattern of spanwise variations in skin friction and other properties which persisted virtually unchanged almost 60 boundary layer thicknesses downstream of the end curvature. Peak-to-peak variations in velocity and skin friction were 10 to 20% of the mean; the wavelength was about twice the local boundary layer thickness. They found that the positions of the spanwise variations appeared to depend on the wind tunnel screens.[1] All of their results, including measurements of Reynolds stresses and triple products, seemed consistent with the presence of longitudinal vortices.

Prabhu & Rao (1980) studied the effects of strong, extended curvature for several different inlet boundary layer thicknesses. Particular attention was paid to eliminating secondary flows due to the endwalls through the use of fences. Stationary spanwise variations as high as 30%

----

[1] Other investigators, including Tan-atichat (1982), and Jayaraman & Reynolds in current work at Stanford have found that, in general, significant nonuniformities can be introduced by mesh screens, depending on how they are selected and mounted in wind and water tunnels. Design criteria for the screens used in the present study may be found in Appendix A.

- 13 -

(peak-to-peak) of the potential wall velocity[2] were measured. However, the pattern of variations did not change appreciably even when the inlet boundary layer thickness was varied by a factor of two. The pattern also persisted unchanged as the boundary layer developed downstream.

Shizawa et al (1981) performed the first (to our knowledge) flow visualization study of turbulent boundary layers on concave walls using the smoke wire technique. Large-scale structures were visible as agglomerations of smoke, and the wavelengths, for two different curvatures, were about 20 times the local momentum thickness. Limitations of the visualization technique prevented the investigators from obtaining more detailed information about the structure of the disturbances. However, momentum thickness was observed to vary by a factor of two across the span, and velocity vectors were inclined up to 4^0 away from the nominal streamwise direction for flow near the concave wall.

In an attempt to impose some periodicity on the spanwise variations for a more systematic study of their effects, Hoffmann & Bradshaw (1981) placed vortex generators on the walls of the settling chamber of their wind tunnel (the same wind tunnel used by Meroney & Bradshaw). Before installing the generators, the spanwise skin friction profile in the curve was found to vary erratically with variations in amplitude up to 20%. The skin friction profile was virtually identical to the one measured by Meroney. The generators were then installed and different spacings investigated. A spacing of 1.46 resulted in the maximum downstream

----

[2] The potential wall velocity is the the calculated velocity of a fluid
  particle at the wall, having the same angular momentum as fluid in the
  potential core.

- 14 -

amplification of the disturbances. The spanwise profiles obtained under

this condition of maximum amplification took on a well-defined periodic-

ity. The upstream variations in skin friction increased from about 5%,

for the no-generator condition, to 10%, with the generators set for max-

imum amplification. Similarly, skin friction variations in the curve

increased from 10% to 30%. A comprehensive set of measurements including

triple products was then taken with the generators set for maximum

amplification. Final discussion of these results by the authors is pend-

ing (private communication, P. Bradshaw, 1981).

Later studies by Bippes & Görtler (1972), Aihara & Sonoda (1981), and

Aihara & Koyama (1981) on laminar boundary layers concentrated on the

development of the Taylor-Gortler vortices along concave walls. These

references also contain other information and bibliographies on laminar

flows. Of relevance to the present study are observations, especially

detailed by Aihara & Koyama (1981), that the upwash region between pairs

of vortices develops a secondary instability in the form of a horseshoe

vortex street. Blackwelder (1981) has drawn analogies between this phe-

nomenon and the bursting process in normal turbulent boundary layers.

A full review of past work on the structure of turbulent boundary

layers on flat walls will not be presented here. Cantwell (1981) gives a

good summary of the current state of knowledge of turbulent flows, and

Savill (1979) highlights the evolution of the physical model for plane

turbulent boundary layers. Although many of the questions regarding the

flow physics remain unanswered, certain structural features are gener-

ally agreed upon. A concise summary taken from Cantwell (1981) follows:

"There appear to be four main constituents of the organized
structure. Nearest the wall is a fluctuating array of stream-
wise counter-rotating vortices... The vortices densely cover
all parts of the smooth wall. Slightly above the streamwise
vortices but still quite close to the wall is a layer that is
regularly battered by bursts that involve very intense small-
scale motions of energetic fluid. The outer layer is also
occupied by intense small-scale motions. These are found pri-
marily on the upstream-facing portions of the turbulent-non-
turbulent interface; the backs of the bulges in the outer part
of the layer. The outer small-scale motions are part of an
overall transverse rotation with a scale comparable to the
thickness of the layer."

A variety of models have been proposed to explain these features and how

they come about; the field is still a subject of current research. Per-

tinent results will be recalled from the literature as needed in the

discussion of results of our study.

Several conclusions can be drawn from the past work. First, recent

investigations indicate a strong tendency for large-scale transverse

motions to develop in a turbulent boundary layer on a concave wall, even

for cases of weak curvature. The precise nature of these disturbances

has not been made clear by prior research; however, many experimenters

tend to attribute the disturbances to a kind of turbulent Taylor-Görtler

vortex system. The wavelength of the disturbances tends to be on the

order of twice the local boundary layer thickness. In no case do the

naturally occurring disturbances display a well-defined periodicity.

The pattern of observed disturbances seems to depend on the specific

characteristics of the apparatus employed since no simple scaling laws

are evident which relate the flow properties to the disturbances. The

failure of the earlier experiments to detect large-scale variations,

despite evidence of strong mixing in mean velocity profiles, and the

several recent results demonstrating the importance of inlet conditions,

raise further questions concerning the true nature of the flow field. Despite extensive single point measurements in this class of flows, little has been done to survey the instantaneous flow field on a global scale, for example by using flow visualization, to clarify the physics of the flow.

1.3 SPECIFIC OBJECTIVES

In order to answer some of the questions raised by the review of the literature above, the following objectives for the study were formulated:

1. Design and construct a large water channel facility whose primary purpose is to allow detailed visual study of turbulent boundary layers on concave walls with moderate curvature ($\delta/R=0.05$).

2. Obtain mean velocity data to qualify the apparatus and quantify some of the more commonly used boundary layer parameters such as momentum thickness and shape factor. Obtain turbulence data as equipment permits.

3. Conduct detailed visual surveys of the flow field upstream of curvature in the curved region, and in the recovery region, employing dye injection through the wall to visualize the flow close to the wall and the hydrogen bubble technique for flow farther out. Determine the effects of concave curvature on flow structures.

4. Develop a qualitative physical model of the flow which explains its observed characteristics.

Chapter II

EXPERIMENTAL METHODS

2.1 FACILITY DESCRIPTION

In order to perform the investigation, a completely new flow facility
was designed and constructed.[3] A photo of the finished apparatus is
shown in Fig. 4 and a schematic of the curved channel in Fig. 5.
Because we designed the water channel with a great deal of flexibility
in mind, detailed design calculations and parts specifications are
described in the Appendices for the benefit of future investigators who
may wish to modify the rig.

2.1.1 General Construction

The facility is a large free surface water channel with plexiglas walls
braced by steel frames. Water enters and leaves through steel inlet and
outlet plenums. The actual test walls are inserted into the main struc-
ture so that water stands on both sides of the test walls. This design
frees the test walls of the loads imposed by the large volumes of water
and enables the walls to retain their shape once they are placed and
adjusted in position.

----

[3] Design and construction of the facility was initially divided among
three students: I designed the curvature water channel and probe tra-
verse, John Simonich took care of sump modifications, the water treat-
ment system, and the mobile instrument platform, and Brian Gyles han-
dled the straight water channel and the plumbing.   The reader should
consult Simonich's thesis for additional design details.

Figure 4: Water channel facility, curved channel in background.
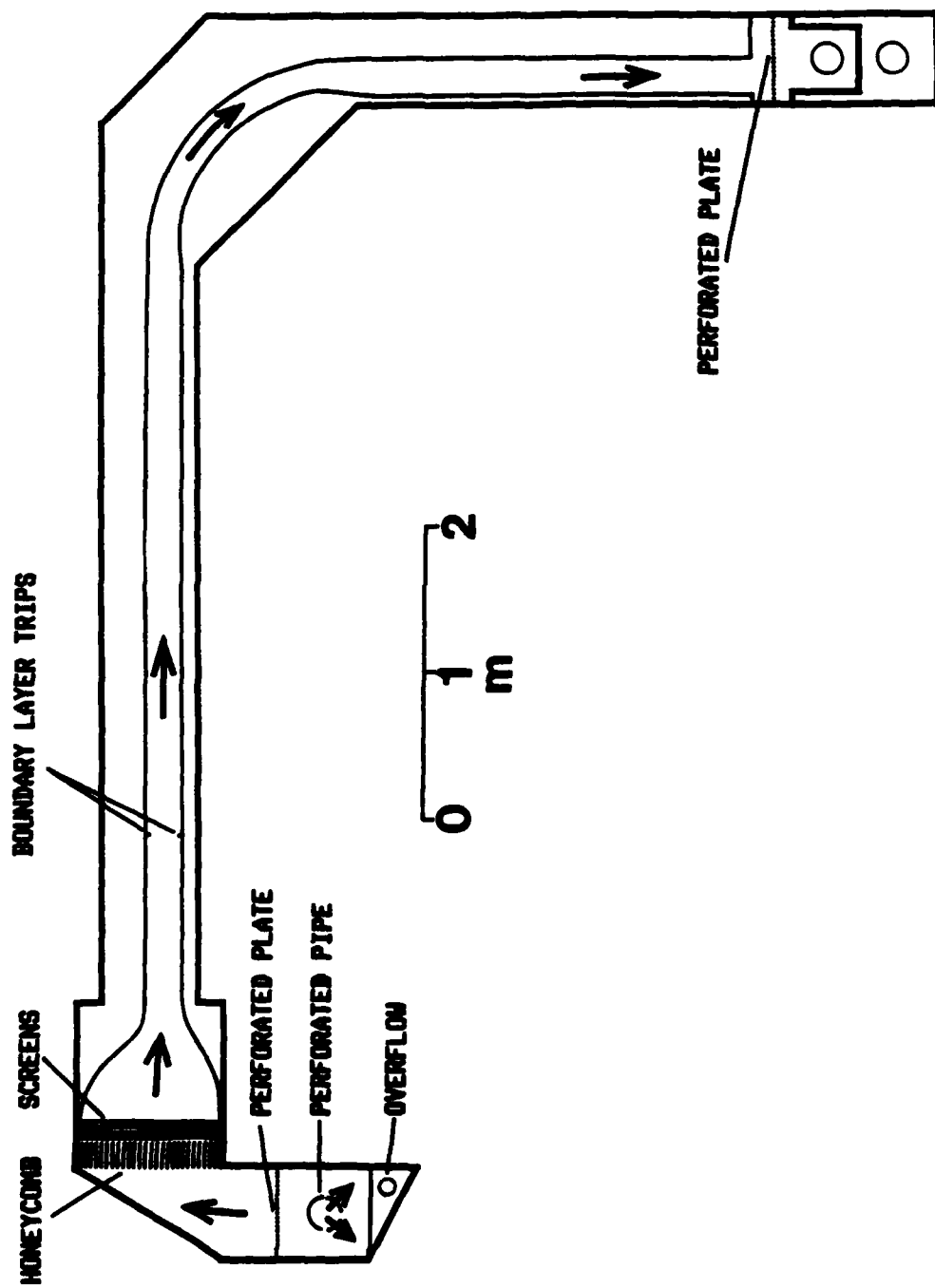
Figure 5: Schematic of concave flow facility.

HONEYCOMB SCREENS

BOUNDARY LAYER TRIPS

PERFORATED PLATE

PERFORATED PIPE

OVERFLOW

PERFORATED PLATE

0 1 2
m

2.1.2 Inlet

Water is pumped from an underground sump by a 7.5 hp deep-well impellor pump. It enters the rig through a vertical perforated pipe. Two disc valves and a bypass leg are used to control the flow rate. A constant height skimmer overflow in the inlet plenum removes much of the surging due to the pump and makes it easier to maintain the water at a fixed height. The flow is then passed through a perforated plate, diffused, and turned. The pressure drop across the perforated plate is of the order of 100 velocity heads in order to remove the larger eddies. A honeycomb panel and four fine mesh screens are used to take out the smaller eddies and reduce the turbulence levels in the flow. A two-dimensional 4:1 contraction ratio nozzle accelerates the flow up to the nominal speed of 15 cm/s.

In the present study, laminar boundary layers leaving the nozzle were tripped 110 cm downstream of the nozzle exit by 0.47 cm (3/16") square rods. The wall opposing the test surface was designed to minimize the streamwise pressure gradient which would otherwise develop due to the blockage effect of the boundary layers.

2.1.3 Test Section

488 cm (16 ft) downstream of the nozzle, the flow is turned in a 90°, 136 cm radius bend. The opposite wall was designed to minimize the streamwise pressure gradient on the curved test surface due to pressure gradients owing to streamline curvature and boundary layer blockage. Following the curve is a 244 cm (8 ft) long recovery region.

2.1.4 Exit

At the end of the recovery section another perforated plate is used to keep the effects of the nonuniform flow in the outlet plenum from propagating upstream. It was not necessary for the present study to use a honeycomb flow straightener prior to the perforated plate at the channel exit. A specially designed valve in the outlet plenum controls the flow back into the sump while at the same time preventing the entrainment of air into the water as it returns to the sump.

2.1.5 Filtration and Air Control

The water was continuously filtered by a diatomaceous earth swimming pool filter, operating in an independent side loop (see Fig. 6). A cavitating nozzle and a vacuum pump deaerated the water, eliminating the fine "mist" of bubbles usually present. These bubbles would have otherwise obscured the hydrogen bubbles used for flow visualization and also prevented the use of hot film anemometers. The water was chlorinated to a level about twice that recommended for swimming pools to prevent algae growth. The pH of the water was not controlled.

2.1.6 Instrumentation

A mobile instrument platform was designed[*] and constructed to run along rails attached to the tops of the channel frames. This platform carries the probe traverse in the streamwise direction. The speed of the platform is monitored by a photodiode which senses the rulings on a tape scale glued to one of the rails.

----

[*] For design details see thesis of J. Simonich.
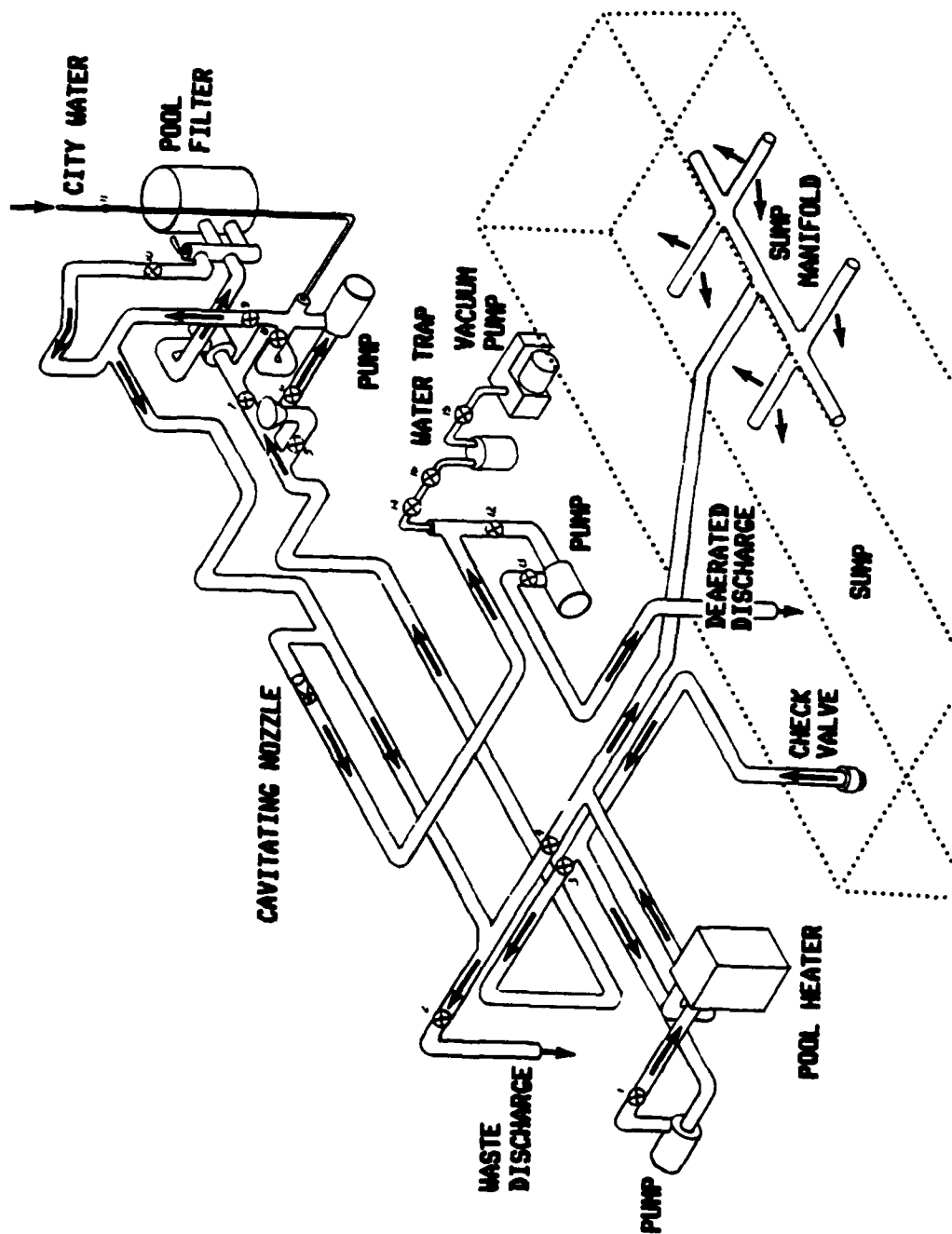
Figure 6: Water treatment piping plan, not to scale.

CITY WATER

POOL FILTER

PUMP

WATER TRAP

VACUUM PUMP

PUMP

CAVITATING NOZZLE

DEAERATED DISCHARGE

SUMP

SUMP MANIFOLD

CHECK VALVE

WASTE DISCHARGE

PUMP

POOL HEATER

A two-axis probe traverse was developed to position probes anywhere in a crossplane to the flow. Stepper motors drive the two axes and are remotely controlled by an indexer. Provisions in the construction of the indexer allow computer control. An interface for a DEC MINC-11 micro-computer was designed and built for the indexer. Details concerning the hardware, electronics, and software of the traverse may be found in Appendix B. A picture of the instrument platform with the traverse is shown in Fig. 7.

Figure 7: Mobile instrument platform with probe traverse.
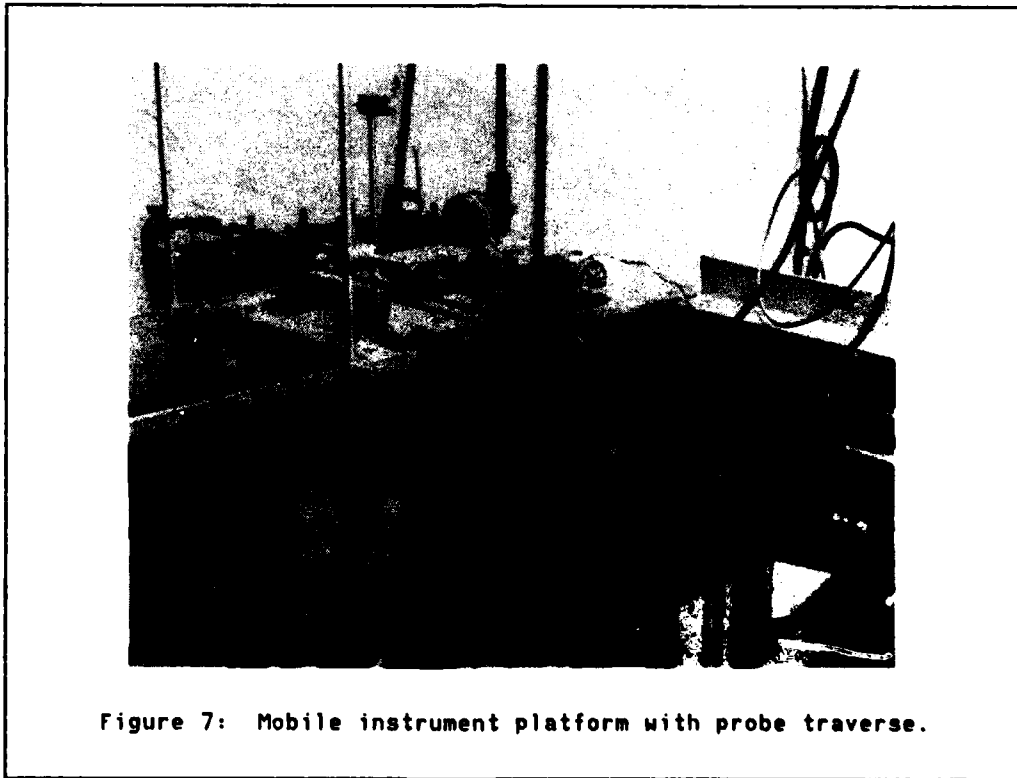
2.2 FLOW VISUALIZATION TECHNIQUE

Two techniques were used to visualize the flow: dye injection and hydrogen bubble generation.
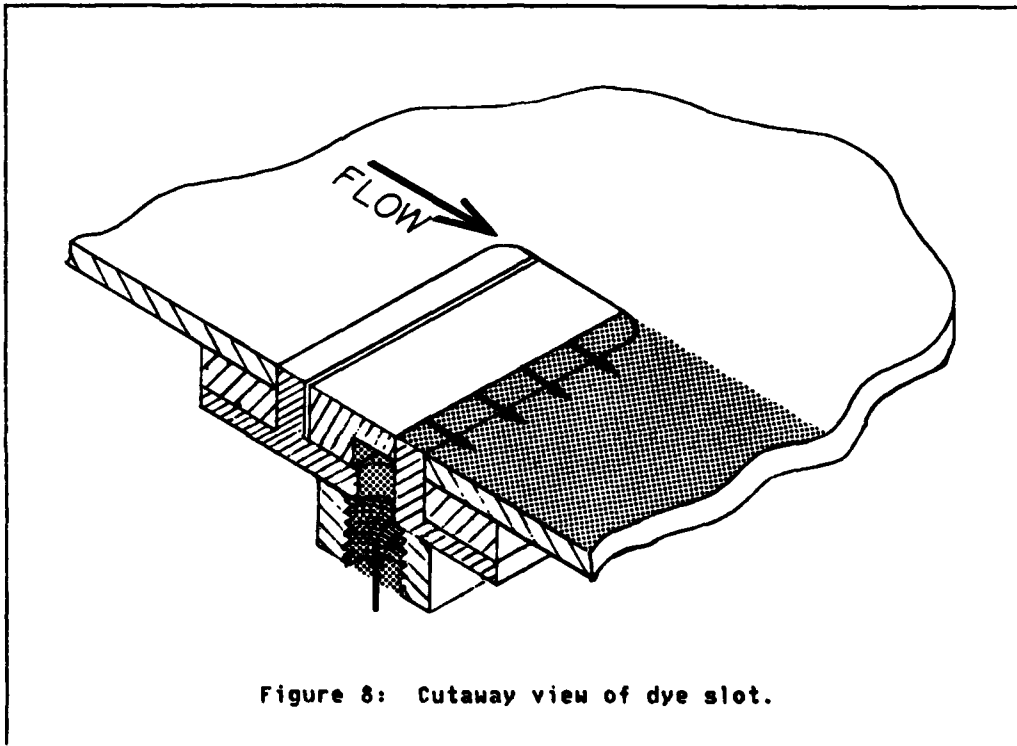
Figure 8: Cutaway view of dye slot.

In the design of the test wall, we included several pairs of dye slots in order to inject dyes into the viscous sublayer (see Fig. 8). Dyes injected into the sublayer through wall slots to visualize the boundary layer structure were first employed by Rundstadler, Kline, & Reynolds (1963) in their pioneering work on turbulent boundary layer structure. In the present study, each dye slot was 30 cm long; the width

of the slot was adjustable and typically set to about 0.02 cm. The slots
were arranged in pairs, with about 20 cm between each pair, in an
attempt to track flow structures over a greater streamwise extent. Each
slot in a pair was fed a different color of dye from a plastic bottle
(ordinarily used for medical procedures) suspended about half a meter
above the water's surface. Small aquarium valves controlled the feed
rate of dye to the slots. The dye consisted of food coloring diluted
with water along with a small amount of isopropyl alcohol to make it
neutrally buoyant and algae resistant. Tests were run with the slots
turned on and then off. These tests indicated that for modest feed rates
(0.15 ml/s, 0.3 cm/s through the slot), the injection of dye had no
qualitative effect on the flow. Dyes contaminating the water supply were
gradually bleached out by the chlorine added to the water for algae pre-
vention.

We also used a modified syringe with a 20 gauge hypodermic spinal
needle to inject dyes at other locations for quick checks of the flow
field.

The dyes were illuminated from the back, through the transparent
plexiglas test surface, by banks of high intensity fluorescent tubes.[5]
High-speed (ASA 400) black and white, and color reversal films (Kodak 4X
and VNF 7250) were used to photograph the flow.

----

[5] The 60 cycle fluctuation of the light intensity made it necessary to
adjust the shutter speeds on our cameras to 1/60 s or slower to avoid
shadows and inconsistent exposures.

To visualize the flow far from the wall, we used the hydrogen bubble technique. This method of visualization was invented by Clutter & Smith (1961) and subsequently used and refined by several Stanford investigators including Schraub et al (1965). A platinum wire electrode 76 microns (3 mils) in diameter and 30 cm long was mounted on a suitable holder and placed in the flow. When energized to a potential of about 125 volts relative to another electrode placed downstream, fine hydrogen bubbles were generated on the wire and swept away by the flow. Sodium sulfate (Na_2SO_4) was added to the water at a concentration of about 150 gm/m^3, as recommended by Thompson (1973), to increase its conductivity. The bubbles were small enough to follow the flow sufficiently close for qualitative purposes. The wire holder and suction cup-mounted mirror used to view the bubbles were found not to significantly affect the flow in the region under observation. An electronic pulse generator (see thesis of J. Simonich for details) enabled us to generate discrete time lines of bubbles of variable width and spacing.

The bubbles were illuminated by a 500 watt spotlight with a tungsten halogen bulb, suspended above the channel and shining down into the water (see Fig. 9). Best results were obtained when the angle between the line of sight and the light beam was as small as possible. Hence, end views were preferred for photographic purposes. End views also accentuated transverse motions of the flow which were difficult to perceive in plan views. High-speed black and white reversal film (Kodak 4X) forced two stops to ASA 1600 was used to photograph the hydrogen bubbles.
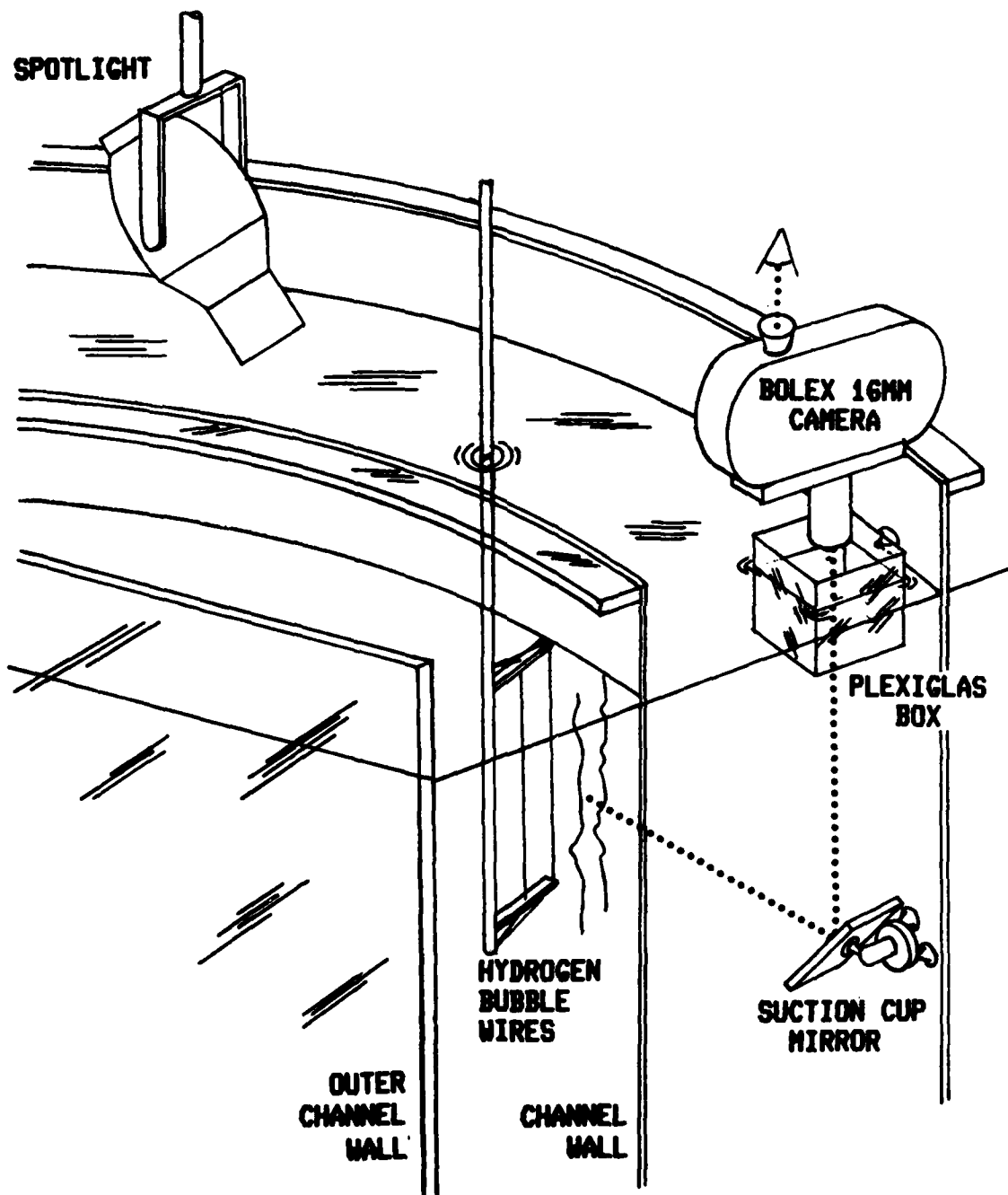
Figure 9: Lighting and viewing arrangement for hydrogen bubbles.

2.3 HOT FILM MEASUREMENT TECHNIQUE

A 0.015 cm (6 mil) diameter TSI quartz-coated cylindrical hot film probe was used to measure velocities in the flow. The length of the exposed sensor was 0.2 cm. The probe was run by a TSI 1010A anemometer unit at an overheat ratio of 1.08. The anemometer's bridge output was connected to an a/d converter in a DEC MINC-11 microcomputer, (see Fig. 10 for layout).

2.3.1 Hot Film Calibration

The channel was filled and set for minimum flowrate by closing the outlet valve. Leakage through the valve limited the minimum mean velocity to about 1.0±0.2 cm/s, determined by measuring the time-of-flight of injected dye. The velocity fluctuated between 0 and 2 cm/s with a period of about 2 s due to sloshing in the channel. The amplitude of this fluctuation was small enough compared with the range of velocities that would be measured (1 to 20 cm/s) so that the difference between the average bridge voltage and the voltage that would correspond to the average speed was negligeable. Therefore, the velocity fluctuations due to the sloshing were largely eliminated by the averaging of the bridge voltage.

The mobile instrument cart towed the probe in the upstream direction. The probe sensor was located about 20 cm below the water's surface. The photodiode speed indicator provided the cart's speed with an uncertainty of ±0.2 cm/s for speeds ranging from 0 to 20 cm/s. A computer program used this speed along with the computed average bridge voltage to create a calibration table. (See Appendix C for a program listing.)

- 30 -
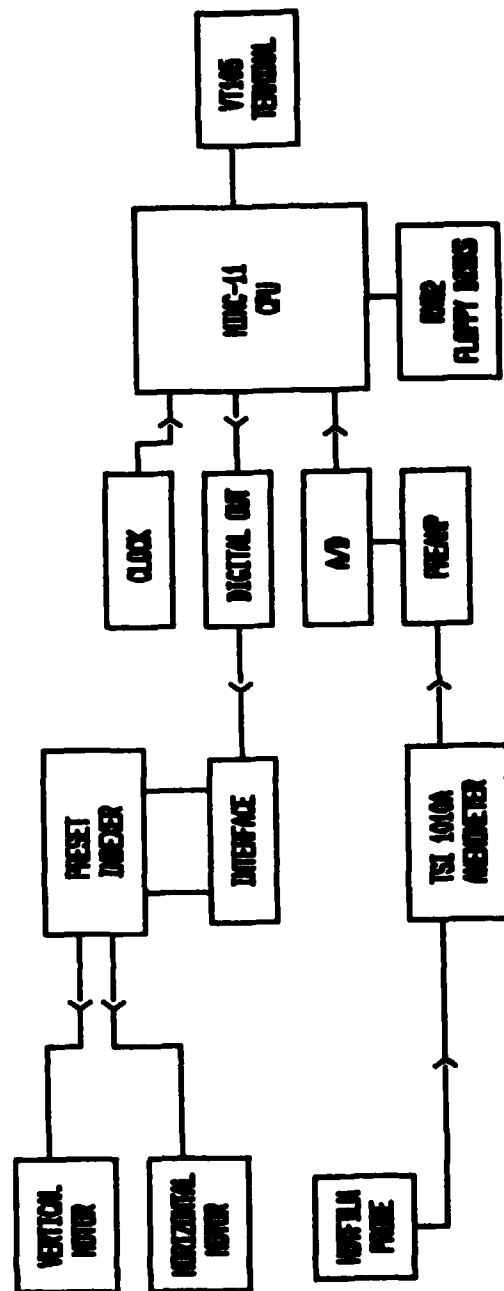
Figure 10: Block diagram of data acquisition system.

In subsequent calibration checks, the probe calibration remained
steady within 0.2 cm/s as long as the temperature remained constant. 3
or 4 spot checks were always performed before commencing a run.

2.3.2   Velocity Measurements

The difficulty of using hot films in water is well-documented by Morrow
& Kline (1971). Before computer control was instituted, we were unable
to control probe drift due to dirt contamination. In addition, the water
temperature generally rose about 0.1 degree Celsius per hour due to
heating from the pump bearings and flow system losses. Automating the
data acquisition process permitted a measurement technique which compen-
sated for some of the shortcomings of hot film probes. The main feature
of this technique was using the bridge voltage obtained in the potential
core region at a fixed reference location to normalize all measurements:

$$e_n = e_m \frac{e_r}{e_r'} \qquad (2.1)$$

where

e_n = normalized voltage at measurement point

e_m = actual voltage at measurement point

e_r = voltage at reference point during original calibration

e_r' = voltage at reference point at time of measurement

This procedure had the effect of minimizing changes in the measured
velocity due to changes in the water temperature, total channel flow
rate, drift of the anemometer electronics, and drift of the probe out-
put due to dirt contamination. Justification for this normalization
procedure is given in Appendix D. Using this procedure, we were able to

- 32 -

obtain results with good repeatability.   One beneficial side effect of
this measurement technique was the almost total elimination of probe
contamination due to dirt.   Evidentally the frequent movement of the
probe helped dislodge dirt which might otherwise accumulate at stagna-
tion points.   As a result, probe drift due to dirt was unnoticeable;
bridge output at the reference point remained constant except for
changes due to drift in the electronics and water temperature, which
were compensated for by the normalization procedure.

The normalization procedure described above requires the establish-
ment of a reference point at a fixed location in the flow.   Since the
cart could not be moved by the computer, secondary reference points were
established at each streamwise location where velocity profiles were
desired.   The velocities at the secondary reference points were measured
with respect to the primary reference point,   which was chosen to be at
x=400 cm, y=12 cm, and z=2 cm. Velocity profiles at different streamwise
locations were then taken by using the secondary reference points for
the normalization procedure.

The typical sequence of steps taken to acquire a velocity profile are
outlined below.

1. The time-of-flight of a dye blob over a 244 cm (8 ft) stretch of
    the inlet was used to determine the nominal velocity at the pri-
    mary reference point. Flow controls for the channel were sensi-
    tive enough to enable us to repeat core velocities to within less
    than 1% of the nominal 14.8 cm/s on any given day.

2. The velocity at the secondary reference point to be used was determined by measuring the mean bridge voltage at the secondary reference point, normalizing it by the voltage at the primary reference point, and interpolating between entries in the calibration table.

3. The wall location was determined by moving the probe against the wall then gradually moving it away while observing the bridge output. The low velocities and high fluctuations near the wall made it difficult to determine the wall location to better than 0.05 cm.

4. The computer was instructed to commence taking velocity measurements. (See program listing in Appendix C.) The probe was positioned by the computer according to a predetermined set of coordinates.

5. Prior to each measurement, the computer moved the probe out to the secondary reference point and sampled the anemometer at 20 hz for 20 s. The mean bridge voltage obtained there and the voltage corresponding to the velocity at the secondary reference point were used to normalize all readings taken at the measurement point according to Eq. 2.1.

6. In turbulent flows, the probe remained at the measurement location for 5 min and was sampled at 6 hz for a total of 1800 samples. In laminar flows, a 20 s average was sufficient. The program kept running tallies of the sum of the velocities and sum of

the velocities squared. At the end of the sampling period, the
mean velocity and turbulence intensity were calculated and writ-
ten into an output file.

Chapter III

RESULTS

3.1 VELOCITY MEASUREMENTS

Profiles of mean velocity and turbulence intensity (u'^2) were measured

in four cross-planes.   For purposes of qualifying the measurement tech-

nique and the apparatus, we also obtained some laminar profiles.

   Fig. 11 shows the coordinate system employed in describing positions

within the flow.   The origin for x was arbitrarily chosen to coincide

with the beginning of the flat test wall, at the exit of the nozzle.

Curvature begins at x=488 cm and ends at x=701 cm.   One cross-plane is

located in the inlet at x=400 cm, two are located in the curve at 30^0

and 75^0 of turning (x=559 cm and x=666 cm, respectively), and the fourth

in the recovery region at x=760 cm.   The coordinate y is measured from

the wall.   z is positive in the upward direction and its origin is

located near midspan, 58 cm from the bottom of the channel.

3.1.1 Laminar Profiles

Fig. 12 shows the mean velocity and turbulence intensity as measured

across the channel at x=400 cm at low channel velocities (6 cm/s) with

the boundary i..yer trips removed.   Cross-channel profiles were taken by

traversing out from each wall with some overlap of the profiles in the

center; the degree to which the readings from separate profiles at the
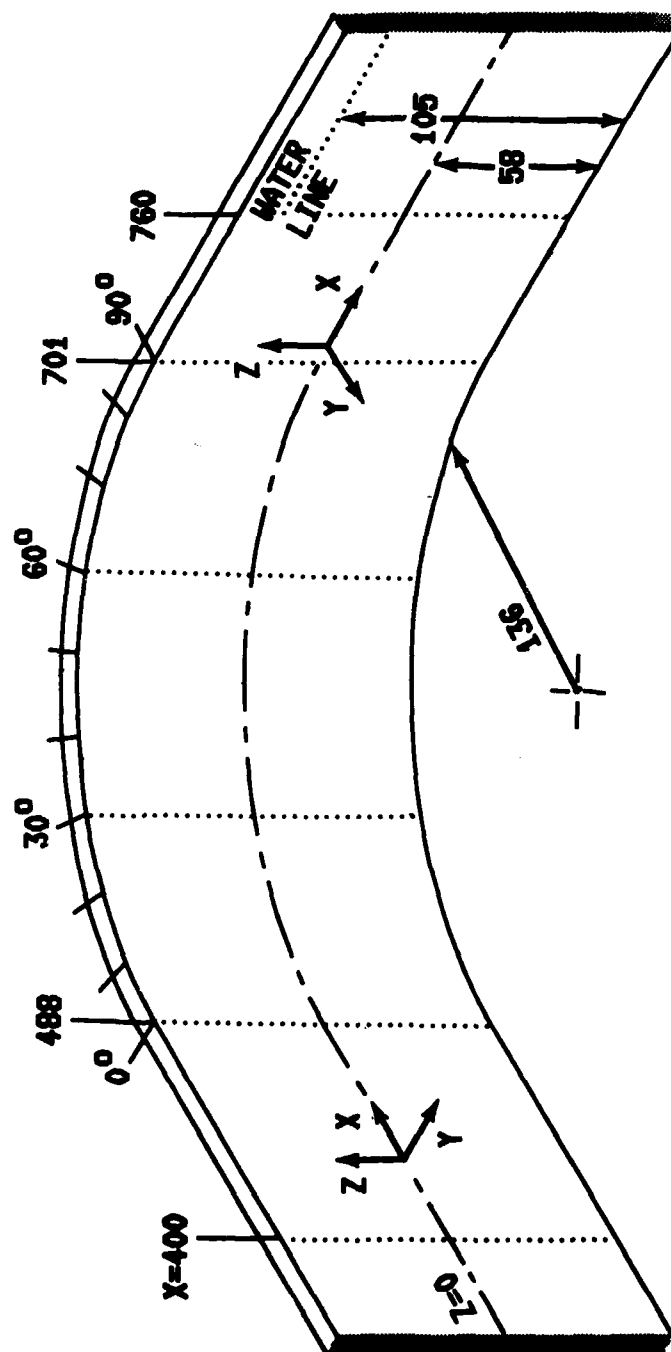
Figure 11: Concave test wall, dimensions in centimeters.

CROSS-CHANNEL VELOCITY PROFILE

LAMINAR FLOW
X=400 cm   Z=0 cm
W$_{CHNL}$=26.0 cm

⟨U⟩ (cm/s)

Y/W$_{CHNL}$

CROSS-CHANNEL TURB. PROFILE

⟨u'^{2}⟩$^{.5}$/U$_{PM}$

LAMINAR FLOW
X=400 cm   Z=0 cm
W$_{CHNL}$=26.0 cm
U$_{PM}$=5.8 cm/s

Y/W$_{CHNL}$
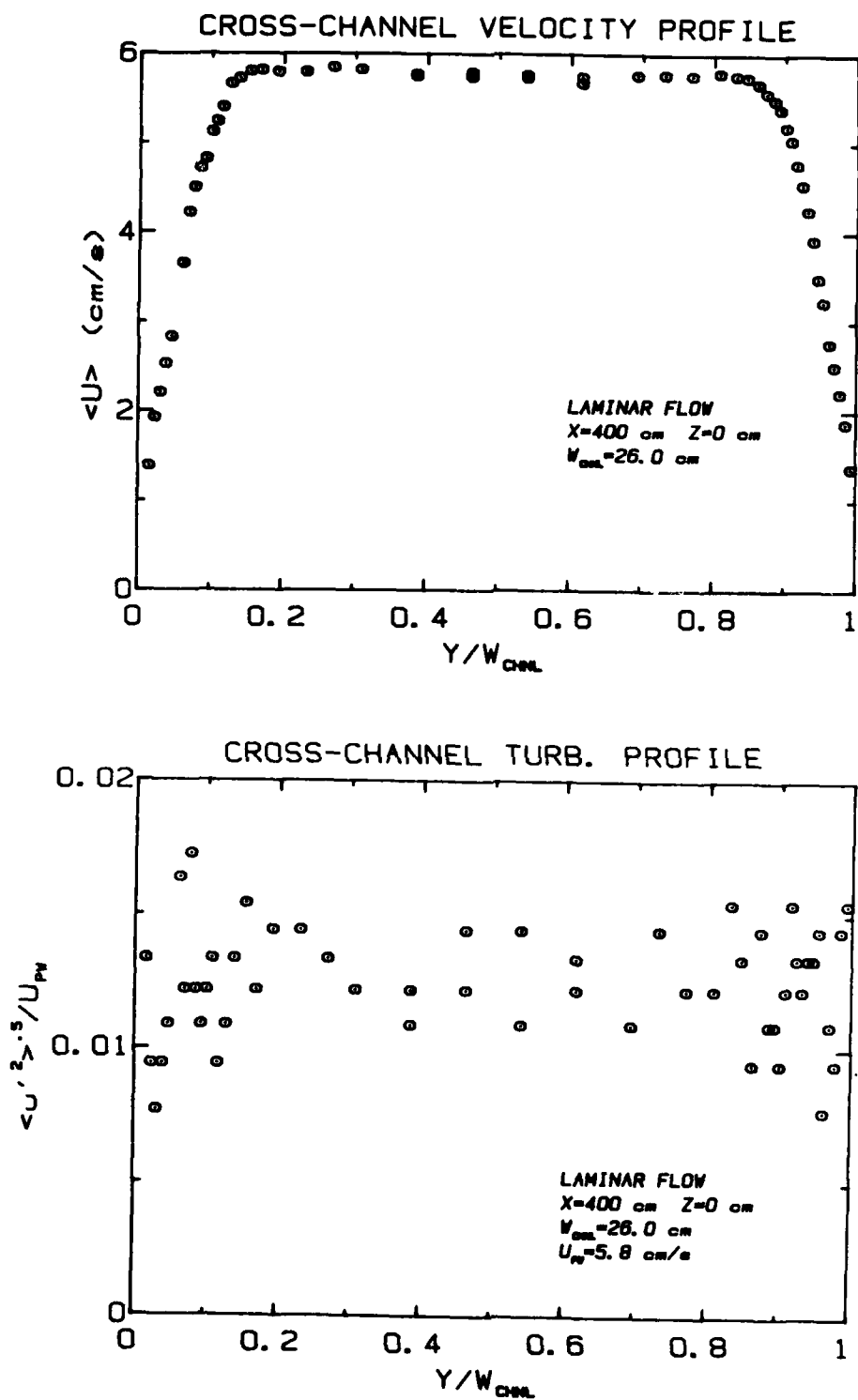
Figure 12: Laminar profiles.

- 38 -

same location agree with each other is a good measure of the repeatability [or first order uncertainty, see Moffat (1978)] of the measurements.

Several sources could have contributed to the relatively high, apparent freestream turbulence intensity (u'_{rms}/U_0=1.3%).

1. The reference voltage[6] in the anemometer was observed to contain two variable components. There was a very slowly varying part which seemed to be due to changes in the room temperature. There was also a more rapidly varying component, with a frequency on the order of a few hertz, which was probably due to noise in the power supply. The slowly varying component was removed by the normalization procedure. The more rapidly varying component is estimated to have added about 0.4% to the turbulence intensity.

2. The finite resolution of the A/D converter could have introduced some spurious fluctuations in the signal. The resolution of the A/D was 2.5 mV (12 bits for a range of 10.24 V). Since the preamplifier feeding the A/D had a gain of 0.5, the effect of having the least significant bit toggle between 0 and 1 would be to cause a spurious turbulence intensity of about 0.5% to appear.

3. The sloshing motion mentioned earlier could have been present to some degree. However, no changes in the water level were visible.

-----

[6] This voltage is the voltage imposed across the resistance bridge in the anemomter circuit and should not be confused with the voltages measured at the reference points in the flow.

Because the emphasis of this study was more on the qualitative features of the flow, further refinements of the measuring technique or the apparatus were not attempted.

LAMINAR VELOCITY PROFILES

X=400 cm   Z=0 cm
U₀=5.85 cm/s
Nu=.009 cm²/s

• TEST WALL (LAM9)
+ CTRL WALL (LAM10)
⊙ TEST WALL (LAM11)
‾ ‾BLASIUS‾ ‾

Figure 13: Comparison of data with Blasius profile.
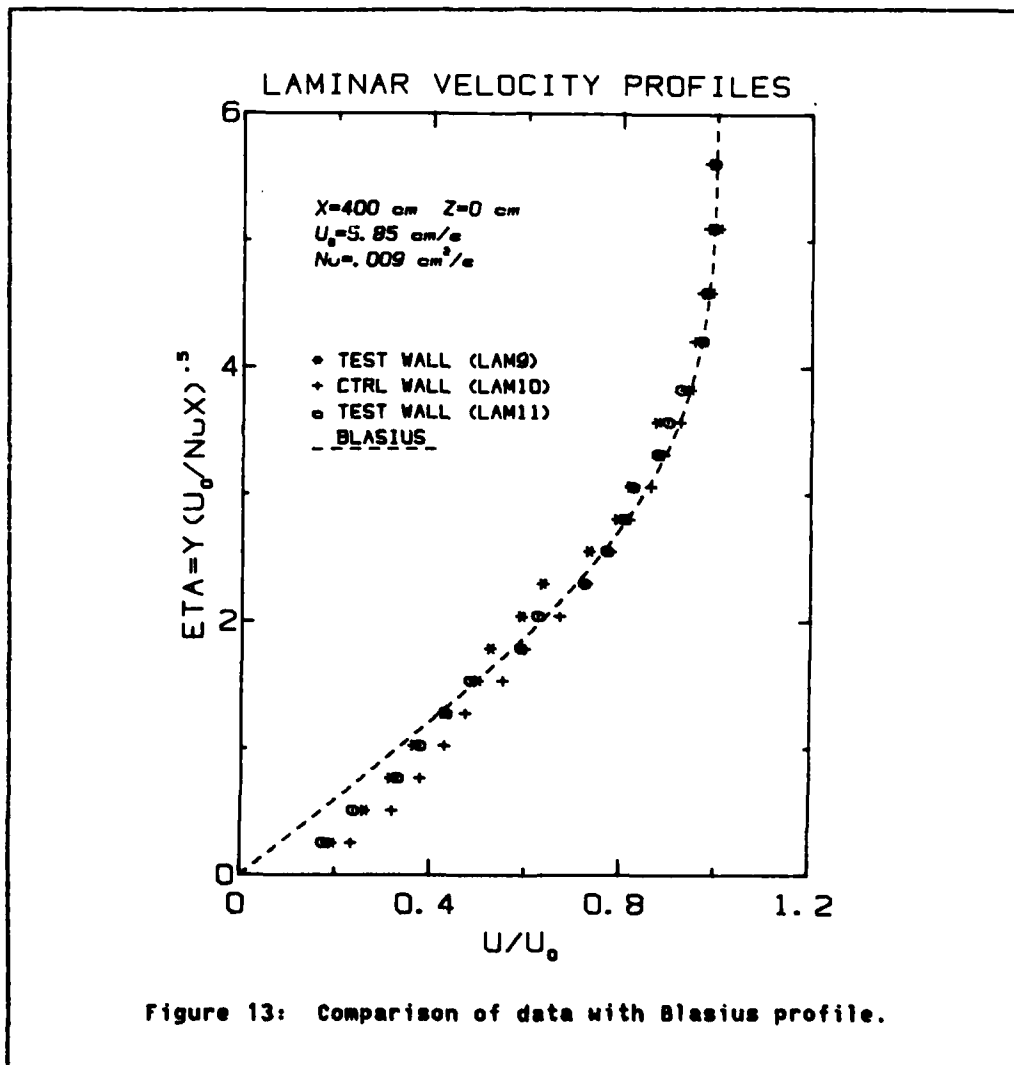
Fig. 13 shows laminar results normalized and compared with a standard
Blasius profile. Agreement is fairly good except near the wall, where,
because of the low flow speed, calibration errors were greater. Probe
blockage effects might also have been present and affected the near-wall
regions of the profiles.

3.1.2 Flat Plate Turbulent Boundary Layer, Upstream of Curved Region

Fig. 14 depicts boundary layer profiles at the inlet to the curve,
x=400, cm at various transverse (spanwise) locations. In each case the
origin of the y coordinate was adjusted to give a best guess for the
actual origin based on close-up examination of the velocity profile near
the wall. In any case the required shift, y_0, was less than the uncer-
tainty in the wall position. At each location the mean velocity profile
is plotted in raw form and in inner, wall coordinates. The value of the
friction velocity used to normalize the data was obtained using a method
suggested by Coles (1968) in which a least-squares fit is performed to
fit the data to Coles' standard velocity profile by varying u^* and δ for
$y^+>50$ and $y/\delta<.75$:

$$u^+ = \frac{1}{\kappa}\ln(y^+) + C + \frac{\Pi}{\kappa} 2\sin^2\left(\frac{\pi y}{2\delta}\right) \tag{3.1}$$

where $\kappa=0.41$ and $C=5.0$. Π is eliminated by evaluating Eq. 3.1 at $y=\delta$:

$$\frac{U_0}{u^*} = \frac{1}{\kappa}\ln\left(\frac{\delta U_0}{\nu}\right) + C + \frac{2\Pi}{\kappa}. \tag{3.2}$$

Eq. 3.2 is used with Eq. 3.1 to eliminate Π while the least-squares fit
is performed to determine u^* and δ. The program used was written by
Rangarajan Jayaraman at Stanford. The program also calculates the

- 41 -

FLATPLATE VELOCITY PROFILES

X=400 cm May 1981		
Data Set	Z (cm)	Y_o (cm)
QUAL3	20	-.03
QUAL1	10	.05
FLAT1	0	-.02
FLAT2	0	-.02
FLAT5	0	.0
QUAL2	-10	.0
QUAL7	-20	-.02

$U^+ = 2.44 LOG Y^+ + 5.0$

$U^+ = Y^+$

X=400 cm May 1981			
	Data Set	Z (cm)	YO (cm)
▽	QUAL3	20	-.03
◇	QUAL1	10	.05
○	FLAT1	0	-.02
◑	FLAT2	0	-.02
◕	FLAT5	0	.0
▢	QUAL2	-10	.0
△	QUAL7	-20	-.02
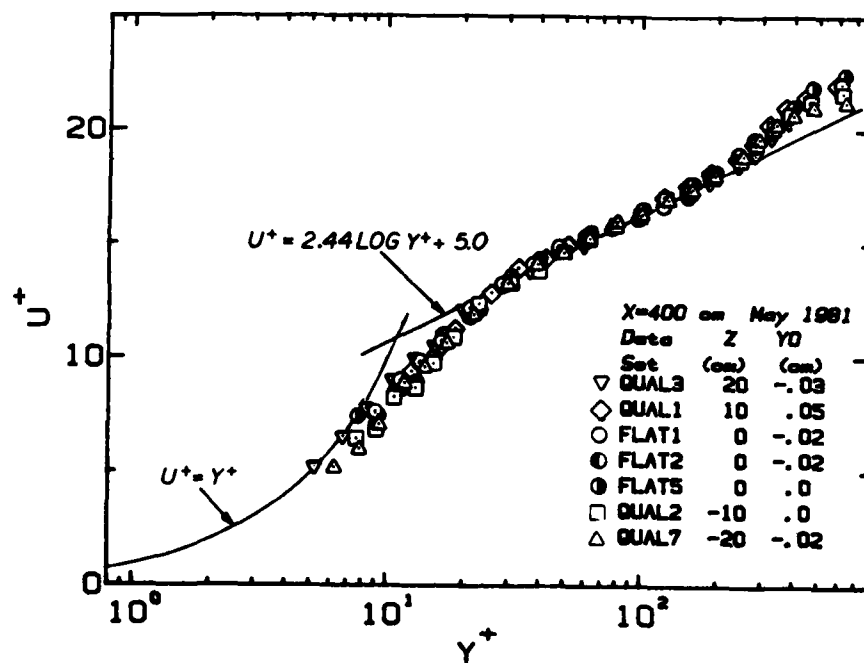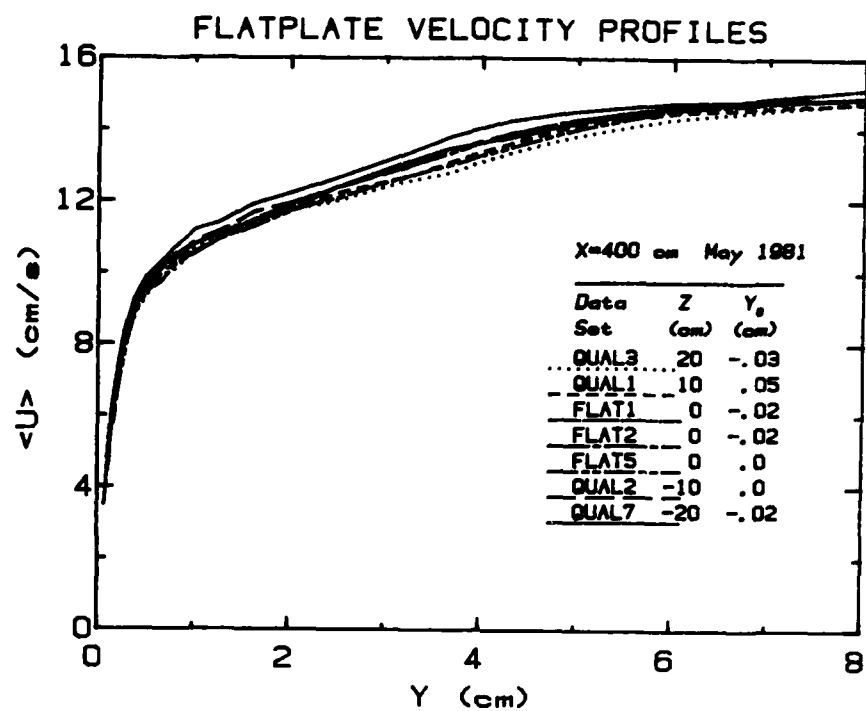
Figure 14: Profiles on inlet flatplate.

- 42 -

standard integral parameters by integrating a standard sublayer profile from the wall to y^+=50 then integrating parabolic segments fitted to the data for the remainder of the boundary layer. The values used for the sublayer integrals are given by Coles as:

$$\int_0^{50} u^+ dy^+ = 540.6, \quad \int_0^{50} u^{+2} dy^+ = 6546. \tag{3.3}$$

TABLE 2

Spanwise variation of boundary layer parameters at inlet, x=400 cm.

Z cm	δ cm	δ* cm	θ cm	H	u* cm/s	Re$_\theta$	c$_f$ .001	Π
20	8.39	1.176	0.826	1.423	0.675	1349	4.164	0.259
10	7.32	1.122	0.782	1.434	0.676	1282	4.146	0.380
0	7.56	1.160	0.814	1.426	0.686	1360	4.101	0.390
0	6.93	1.057	0.734	1.440	0.684	1206	4.222	0.361
0	7.75	1.170	0.815	1.437	0.666	1428	3.979	0.387
-10	6.94	1.046	0.729	1.433	0.688	1200	4.259	0.338
-20	6.14	0.931	0.648	1.436	0.702	1066	4.434	0.321
design	8.64	1.198	0.811	1.477	0.655	1240	3.706	0.322

Some of the more commonly used parameters appear in Table 2 along with their design values. First-order uncertainty in the measurements is reflected by the scatter of the results at z=0 (data sets FLAT1, 2, and 5). In general the boundary layer was slightly thinner towards the bottom of the channel; this is further supported by the spanwise measurements discussed below. Because of the emphasis of this study on qualitative results, we considered the variations in boundary layer parameters

acceptable. For example, over the central 20 cm of the span from z=-10
to z=+10, θ and δ had standard deviations of 5% about their repective
means of 0.775 cm and 7.30 cm and u* had a standard deviation of 1.3%
about its mean of 0.68 cm/s. In any case, at all 5 locations the bound-
ary layer appeared to be typical of a flat plate turbulent layer grown
in a zero pressure gradient to a modest momentum thickness Reynolds num-
ber of approximately 1300.

Turbulence intensity profiles at the inlet also appear normal. Fig.
15 compares turbulence intensity profiles taken at x=400 cm and z=0 with
those obtained by Klebanoff (1954). Note that Klebanoff's data were
taken at a much higher Reynolds number. Considering the uncertainty in
our data, reflected by the scatter, agreement is adequate.

3.1.3   Surveys of the Flow Field

A series of cross-channel mean velocity and turbulence intensity pro-
files were taken at the four locations described earlier: x=400 cm, 30°,
75°, and x=760 cm.   The integral parameters for the test wall boundary
layers at these locations appear in Table 3. These parameters were cal-
culated by fitting parabolic segments to the data and integrating.   The
standard Coles profile (Eq. 3.1) doesn't appear suitable in the curved
and recovery regions, so c_f was not calculated.

To simplify graphing and interpreting the cross-channel profiles, the
normal coordinate y, measured from the concave wall, has been normalized
by the local channel width at each successive streamwise location.
Velocities measured at locations in the curve have been normalized
according to the relation

- 44 -

TURBULENCE INTENSITY PROFILES

$X=400$ cm $Z=0$ cm
$U_{\rho\prime}=14.8$ cm/s
$DELTA=7.5$ cm

○ FLAT1
● FLAT2   } $Re_\theta=1300$
+ FLAT5
▲—▲ KLEBANOFF $Re_\theta=7800$

Figure 15: Comparison of data with Klebanoff's.
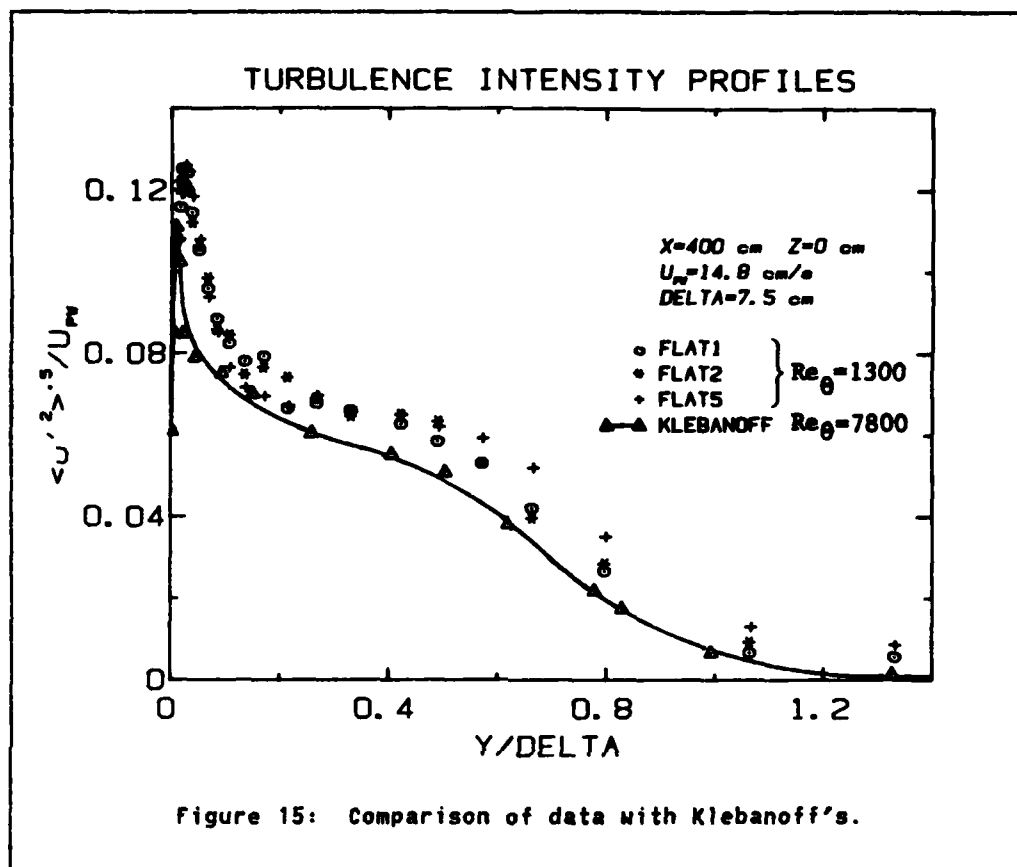
$$U_n = U\left(\frac{R_0 - y}{R_0}\right) \tag{3.4}$$

where R_0 is the radius of curvature of the concave wall. Data presented
in this way show more clearly than a plot of simple velocity the depar-
ture of the data from potential flow. For curved potential flow, the
angular momentum Ur is a constant, where r is the distance from the cen-
ter of curvature. Hence, in the present case, where $R_0-y=r$, the poten-
tial core of the flow appears as a region of constant U_n. Furthermore,
the value of this constant gives the potential velocity at the concave

TABLE 3

Streamwise development of integral parameters.

Location	δ cm	δ* cm	θ cm	H	Data Set
X=400 cm	7.56	1.160	.814	1.426	FLAT1
	6.93	1.057	.734	1.440	FLAT2
	7.75	1.170	.815	1.437	FLAT5
30°	10	1.184	.874	1.354	CRV30
75°	merged	1.141	.935	1.221	CRV75
X=760 cm	merged	.758	.567	1.338	FL760

Note: Integral parameters at locations in curve
      based on radius-normalized velocities. δ at 30°
      estimated from velocity profile.

wall (where y=0).   The potential wall velocities used to normalize the
turbulence intensity, u',   were obtained in this way by examining the
cross-channel velocity profiles. For measurements taken at 75° and x=760
cm, where no potential regions were evident, the maximum value of U_n has
been used.

Fig. 16 shows the profiles at x=400 cm, about 10 boundary layer
thicknesses upstream of the start of curvature; the flow appears fairly
symmetrical. 30° into the curve, (Fig. 17), the mean velocity and turbu-
lence intensity show some pronounced changes. A potential core is still
evident across the middle fifth of the channel. However, the region of
turbulent activity on the concave wall has enlarged and extends further
out into the flow while a drop in turbulent activity is evident near the
convex wall. This trend continues as shown by the data at 75° (Fig. 18).

CROSS-CHANNEL VELOCITY PROFILE

X=400 cm   Z=0 cm
W_CHNL=26.0 cm

CROSS-CHANNEL TURB. PROFILE

X=400 cm   Z=0 cm
W_CHNL=26.0 cm
U_PN=14.8 cm/s
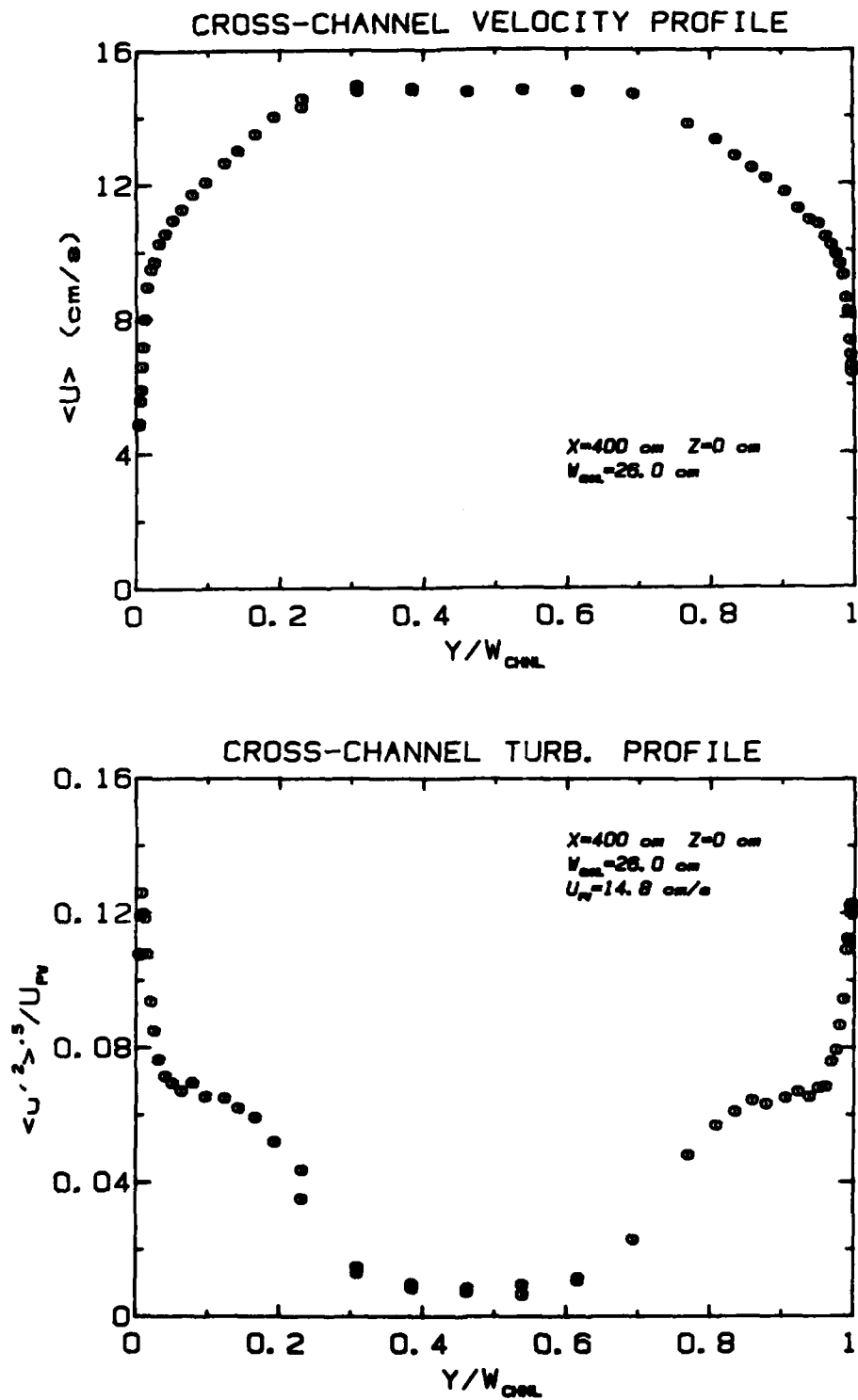
Figure 16:   Cross-channel profiles at x=400 cm, inlet section.

CROSS-CHANNEL VELOCITY PROFILE

$30°$ $Z=0$ cm
$W_{CHNL}=25.0$ cm
$R_o=138$ cm

CROSS-CHANNEL TURB. PROFILE

$30°$ $Z=0$ cm
$W_{CHNL}=25.0$ cm
$U_m=14.3$ cm/s
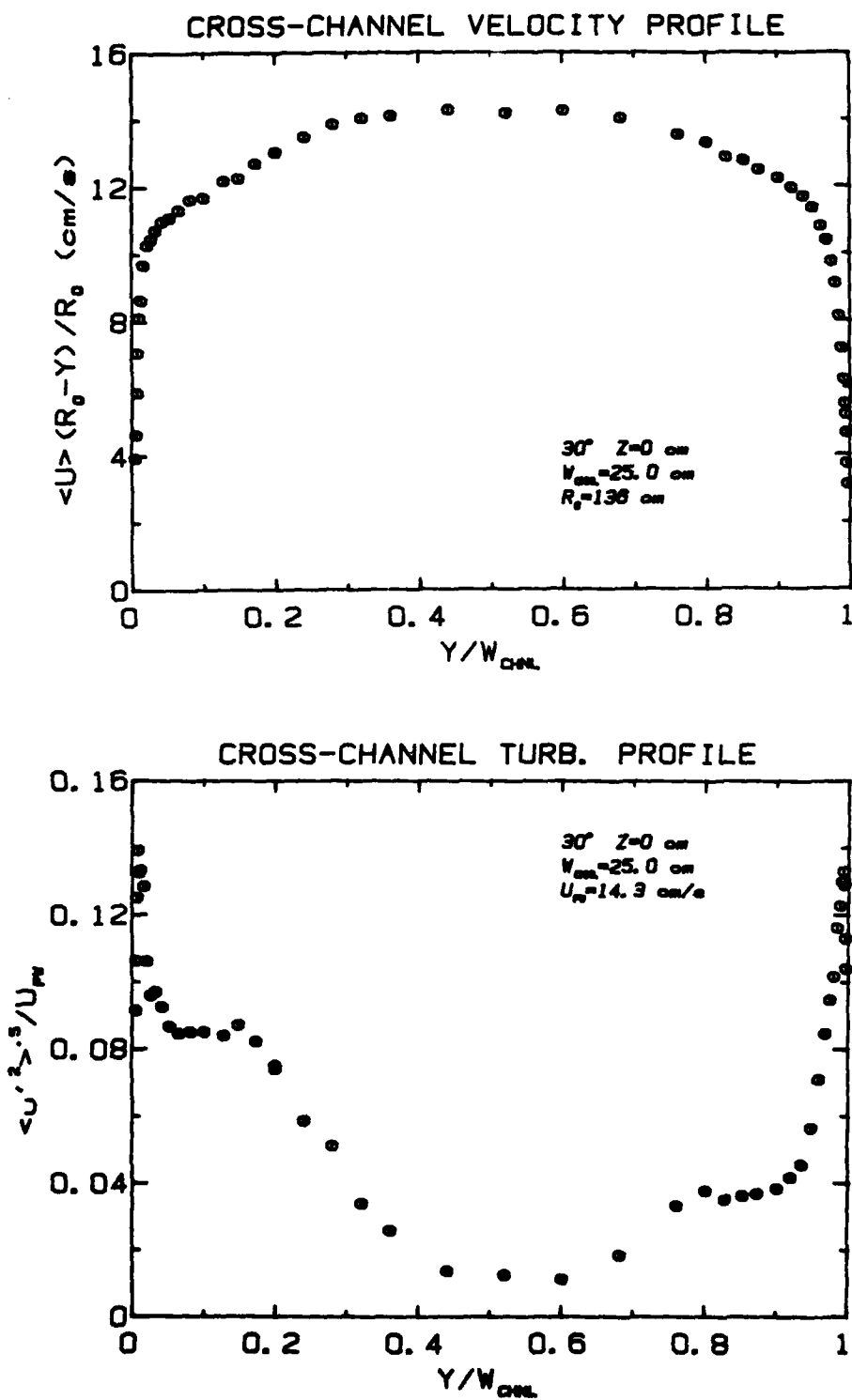
Figure 17: Cross-channel profiles 30° into the curve (x=559 cm).

CROSS-CHANNEL VELOCITY PROFILE

CROSS-CHANNEL TURB. PROFILE
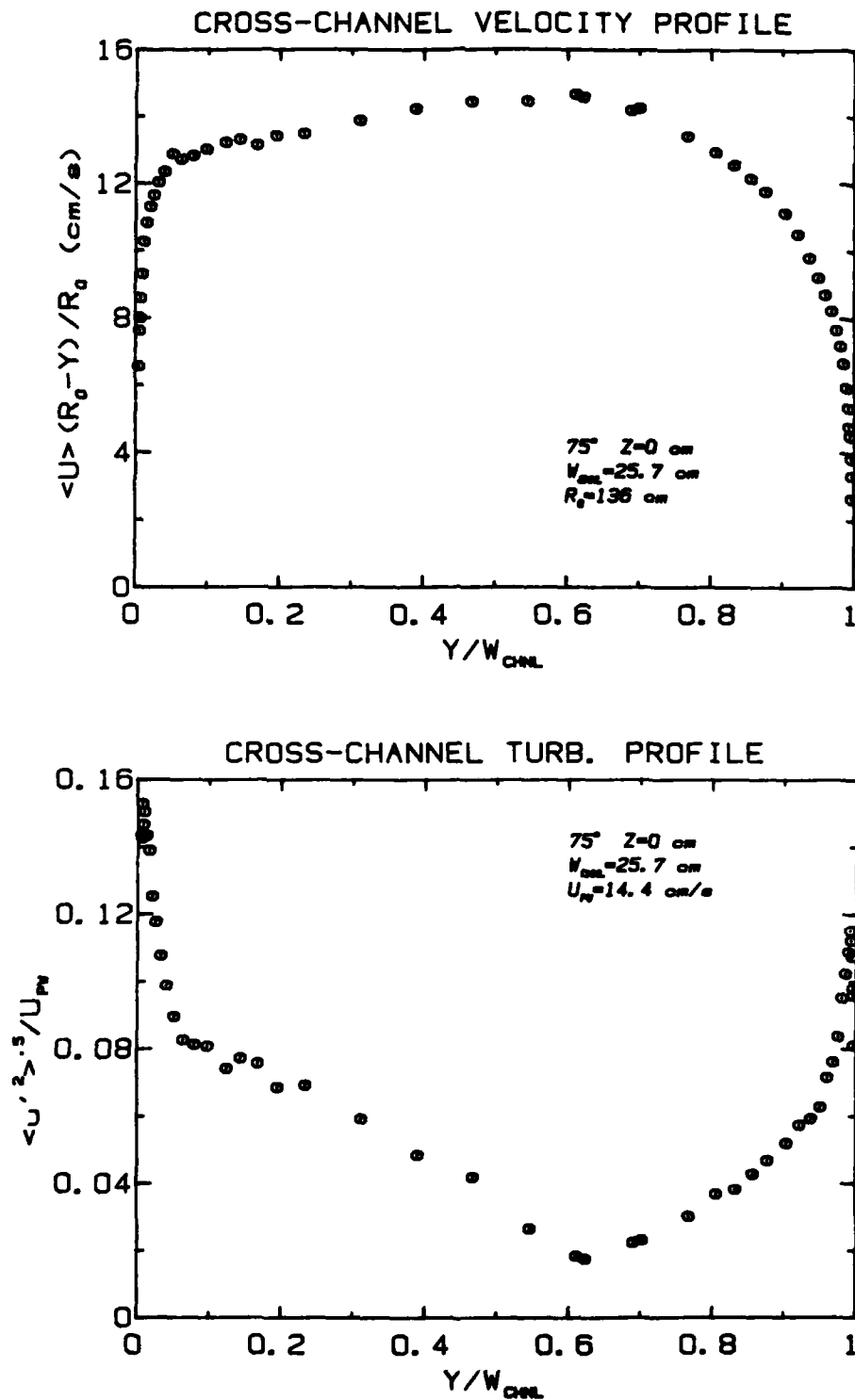
Figure 18:   Cross-channel profiles 75° into the curve (x=666 cm).

The velocity profile is considerably fuller than that for a flatplate, evidence of substantial mixing. Both the velocity and turbulence intensity profiles suggest that the boundary layers on the side walls have merged by this point.

In the flat wall region at x=760 cm, 59 cm downstream of the end of curvature, the profiles (Fig. 19) show no sign of recovery. The convex wall side of the profile shows the effects of the expansion in channel width at the 90° location. As mentioned earlier, the convex wall was shaped to minimize the streamwise pressure gradient on the test surface. This design requires an expansion of the channel at the end of curvature. This expansion produces a strong adverse pressure gradient on the convex wall, and thereby creates a small separation bubble or recirculation zone. Injected dye indicated flow separation a few centimeters upstream of 90° and reattachment about 20 cm later, 40 cm upstream of the measurement station at x=760 cm. The effects of the separation and reattachment are evident in the mean velocity and turbulence intensity profiles in the vicinity of the convex wall at x=760 cm. These profiles strongly resemble those obtained by Eaton (1980) downstream of reattachment behind a backward-facing step. The effects of the separation and reattachment on the convex wall appear not to have any effect on the concave test wall profiles.

Figs. 20-22 show the results of core surveys at x=400 cm, 30°, and 75°. Profiles were taken by traversing in the y direction at each of 21 spanwise (z) locations spaced 2 cm apart. Since the ordinate for the U profiles begins at 10 cm/s, the scatter of the data appears larger than

- 50 -

CROSS-CHANNEL VELOCITY PROFILE

X=760 cm   Z=0 cm
W_{CHNL}=27.0 cm

CROSS-CHANNEL TURB. PROFILE

X=760 cm   Z=0 cm
W_{CHNL}=27.0 cm
U_{RF}=15.8 cm/s
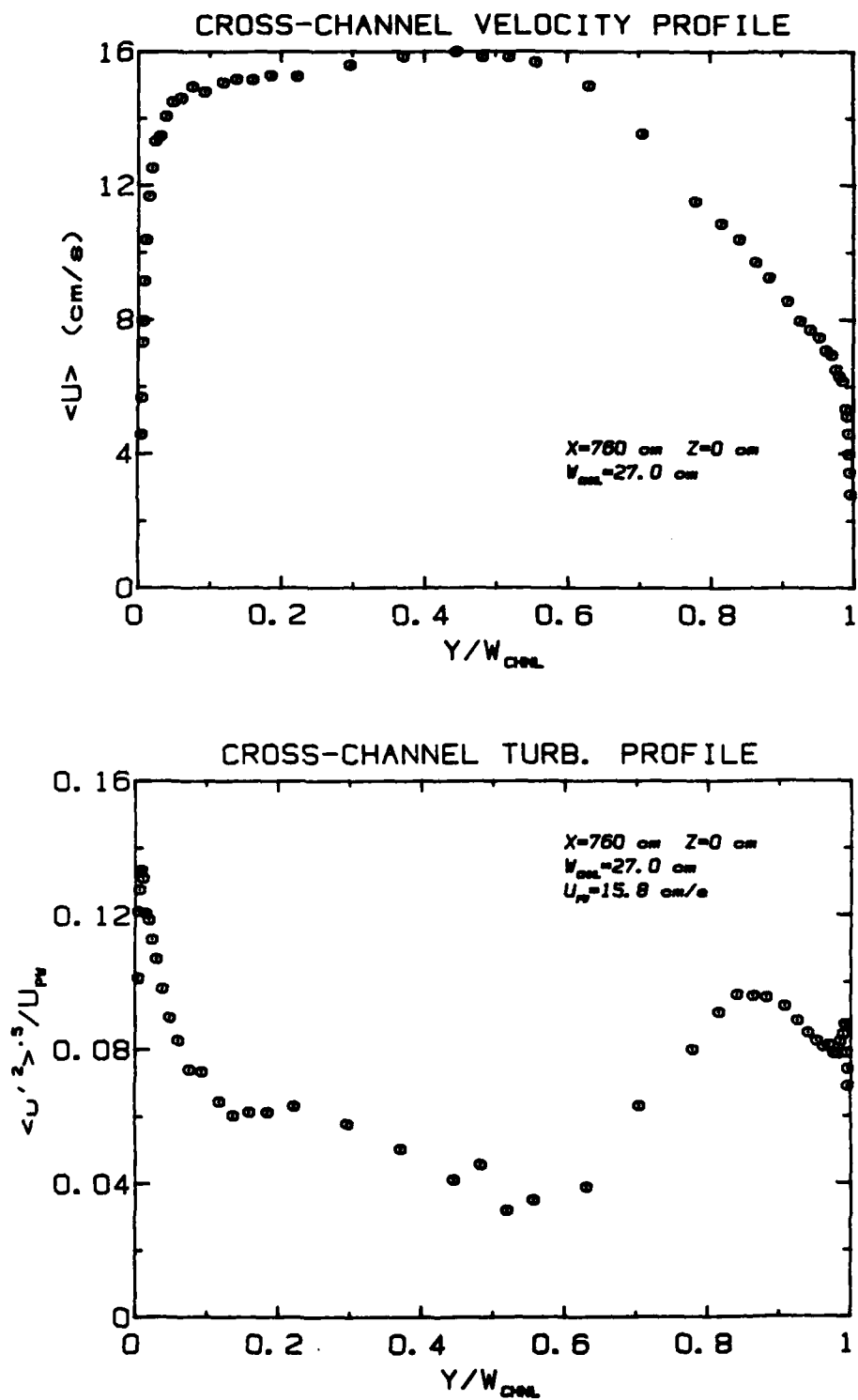
Figure 19:   Cross-channel profiles at x=760 cm, recovery section.
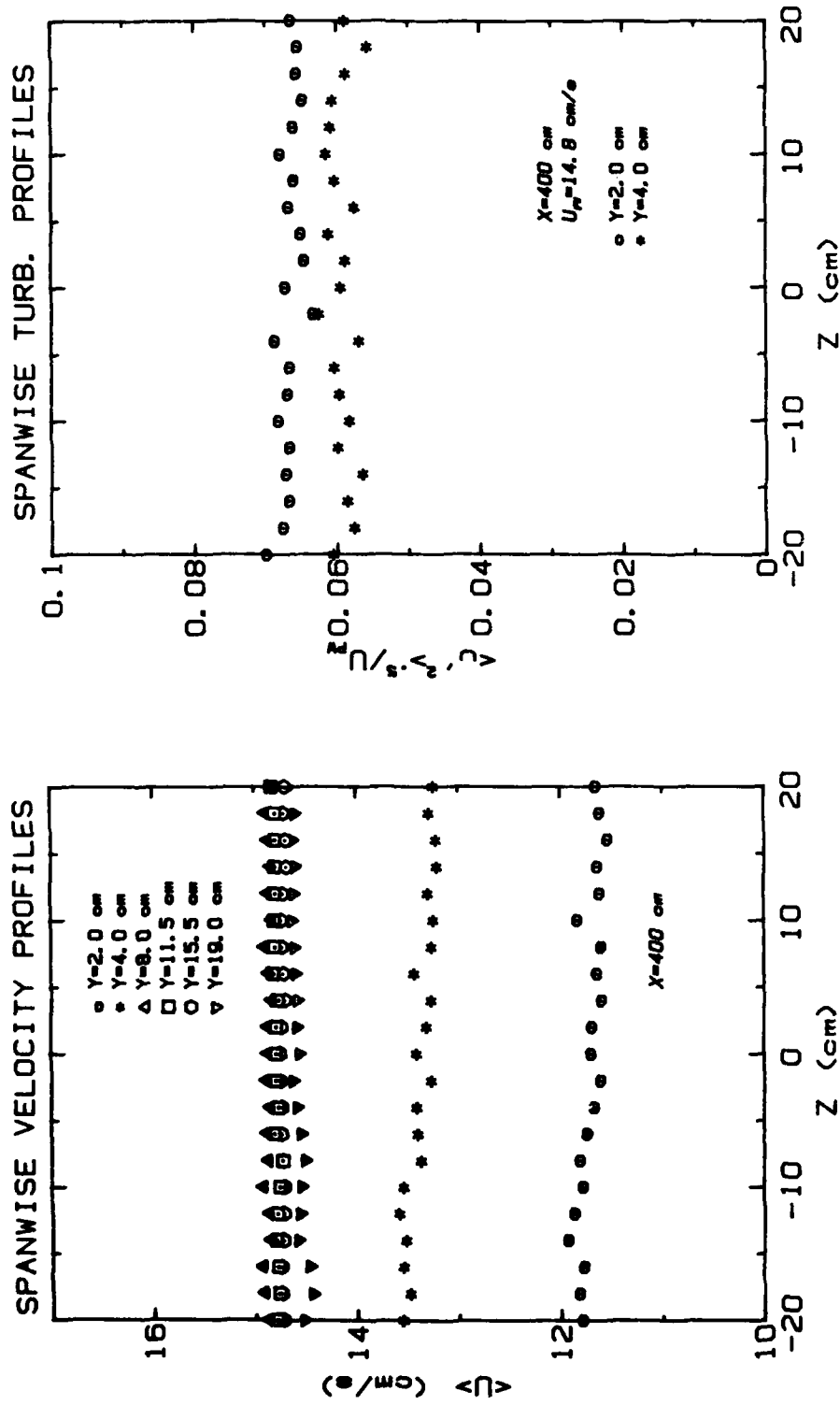
Figure 20: Spanwise profiles at x=400 cm.
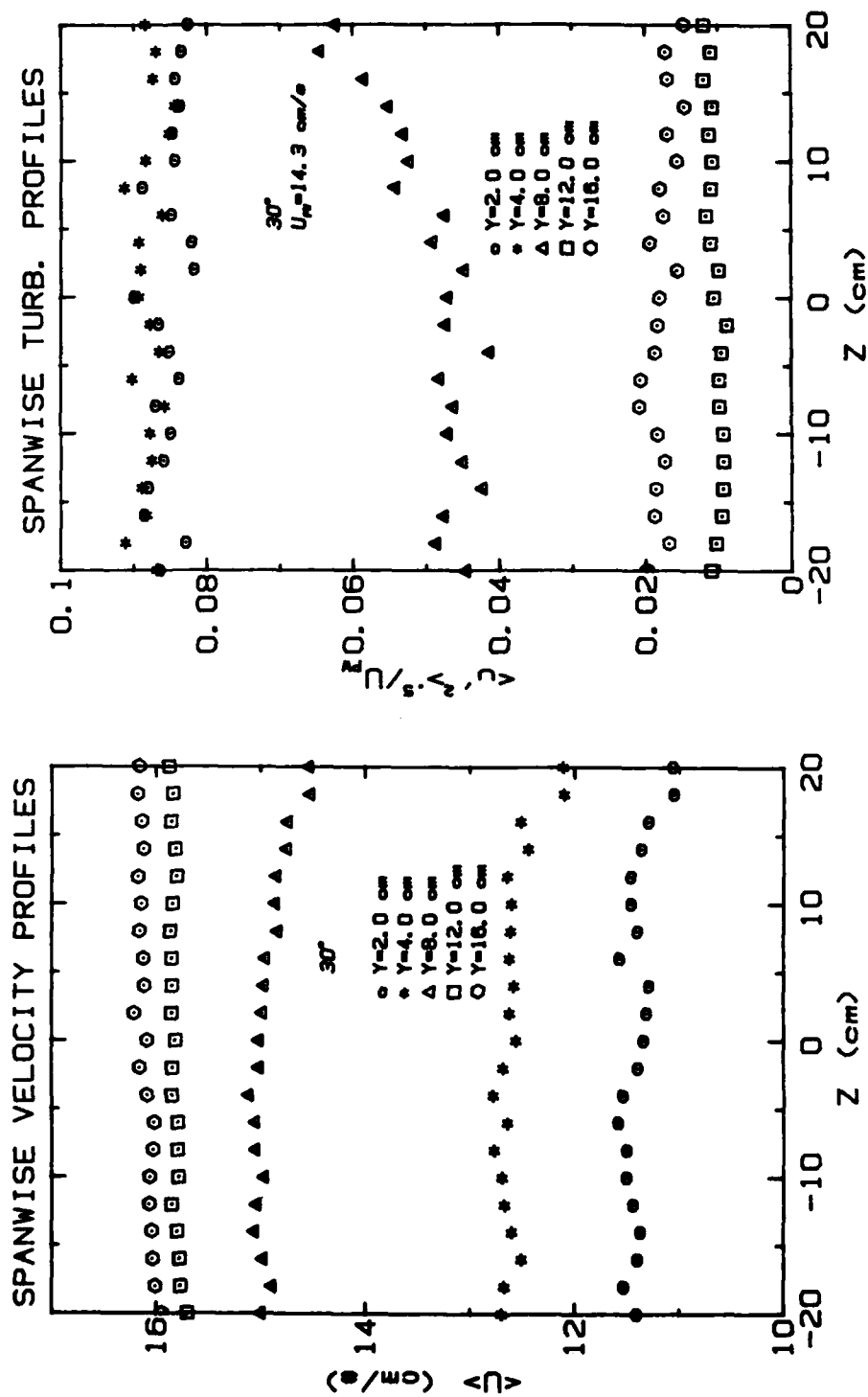
Figure 21: Spanwise profiles at 30°.
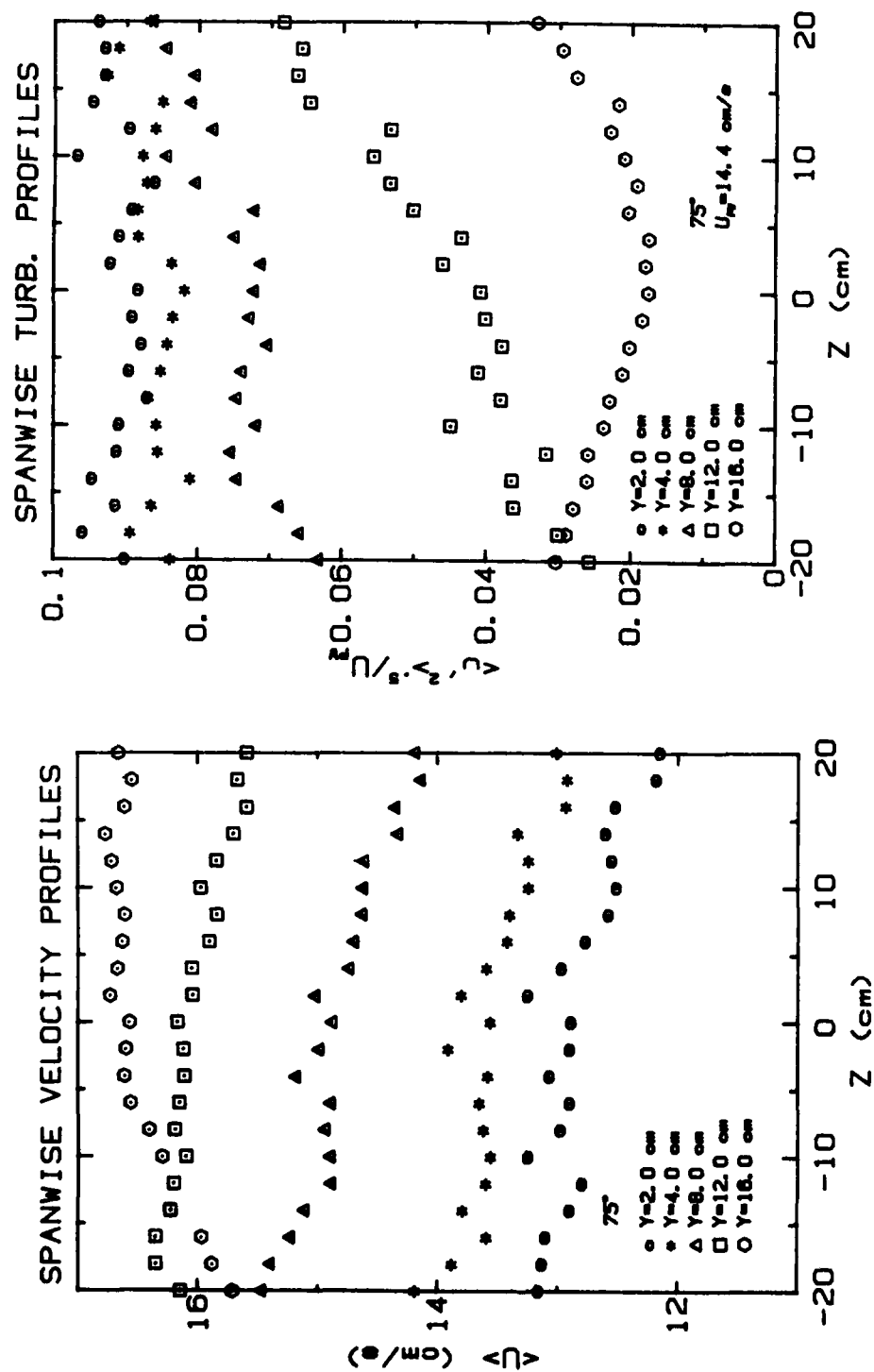
Figure 22: Spanwise profiles at 75°.

- 54 -

the scatter in previous graphs. Fig. 20 confirms the trend mentioned above, namely the boundary layer is thinner towards the bottom of the channel; the profiles at y=2 and 4 cm show slightly higher velocities for smaller values of z. The turbulent profiles, however, appear fairly uniform. Fig. 21 also shows the boundary layer to be somewhat thinner towards the bottom of the channel. The skewing of the turbulence intensity profile at y=8 cm is consistent with this trend. The turbulence intensity profiles at the other y locations are not as skewed because the cross-channel profile (Fig. 17) is relatively flat in those regions. Fig. 21 reveals that, aside from the fluctuations due to scatter in the data, no regular variation in mean velocity is apparent across the span of the channel covered by the traverse. At 75° (Fig. 22) the skewing of the turbulence intensity profiles has propagated to y=12 cm as well, although the inner profile. are still uniform. The mean velocities also show less uniformity, and scatter in the data is larger due to the higher turbulence intensities and the lack of a potential core for consistent normalization of the anemometer output.

Fig. 23 directly compares centerline profiles along the concave test surface as the flow develops. The velocity profiles are seen to become fuller, and the region of high turbulent intensity extends further away from the wall as the flow proceeds downstream.

3.1.4 Clauser Plots

In order to determine if a log region existed in the boundary layer on a concave wall, the mean velocity was plotted against the logarithm of the distance from the wall (Fig. 24). Uncertainty in the probe position
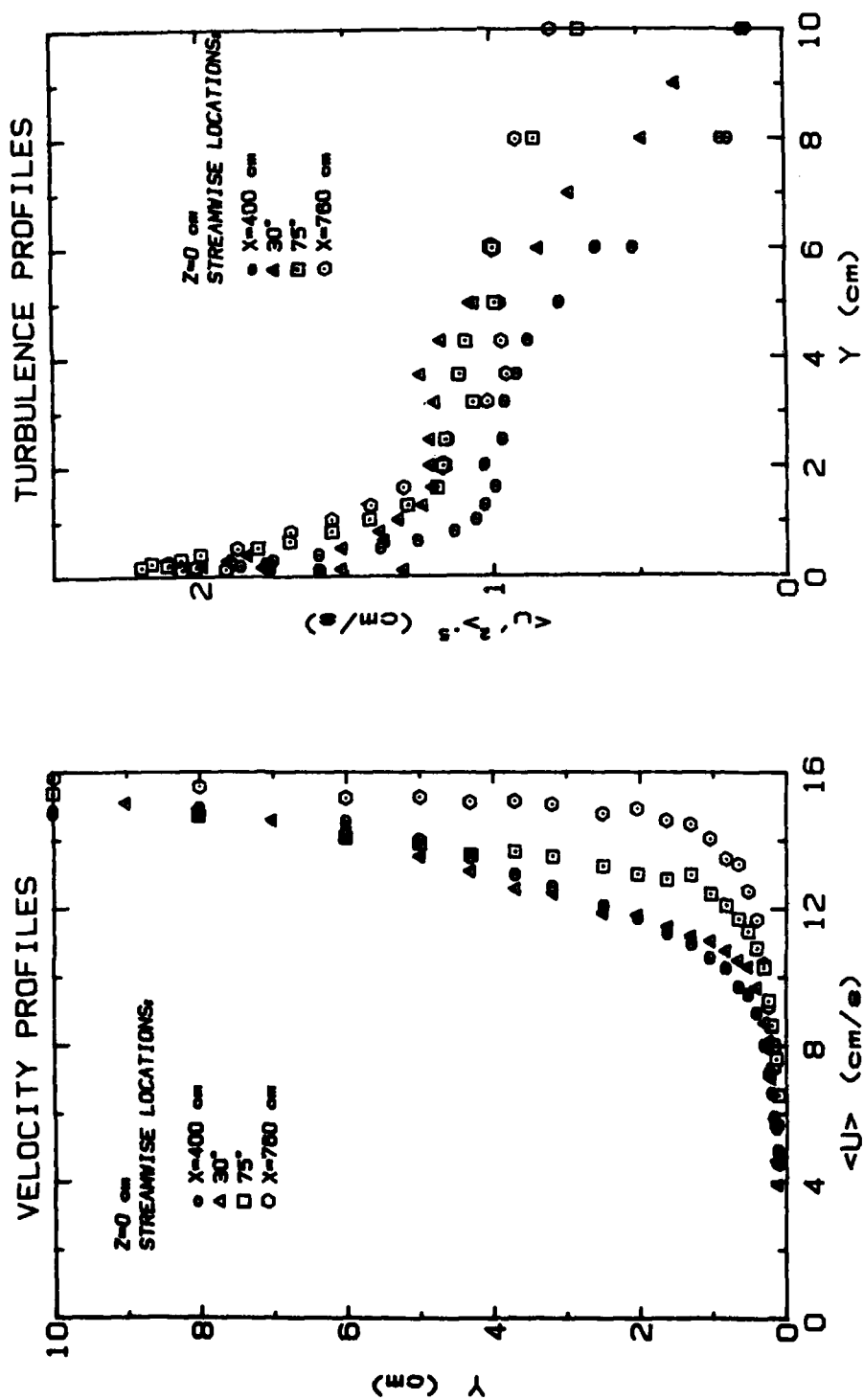
Figure 23: Streamwise development of velocity and turbulence intensity profiles.

Figure 24: Clauser plots of mean velocity profiles.
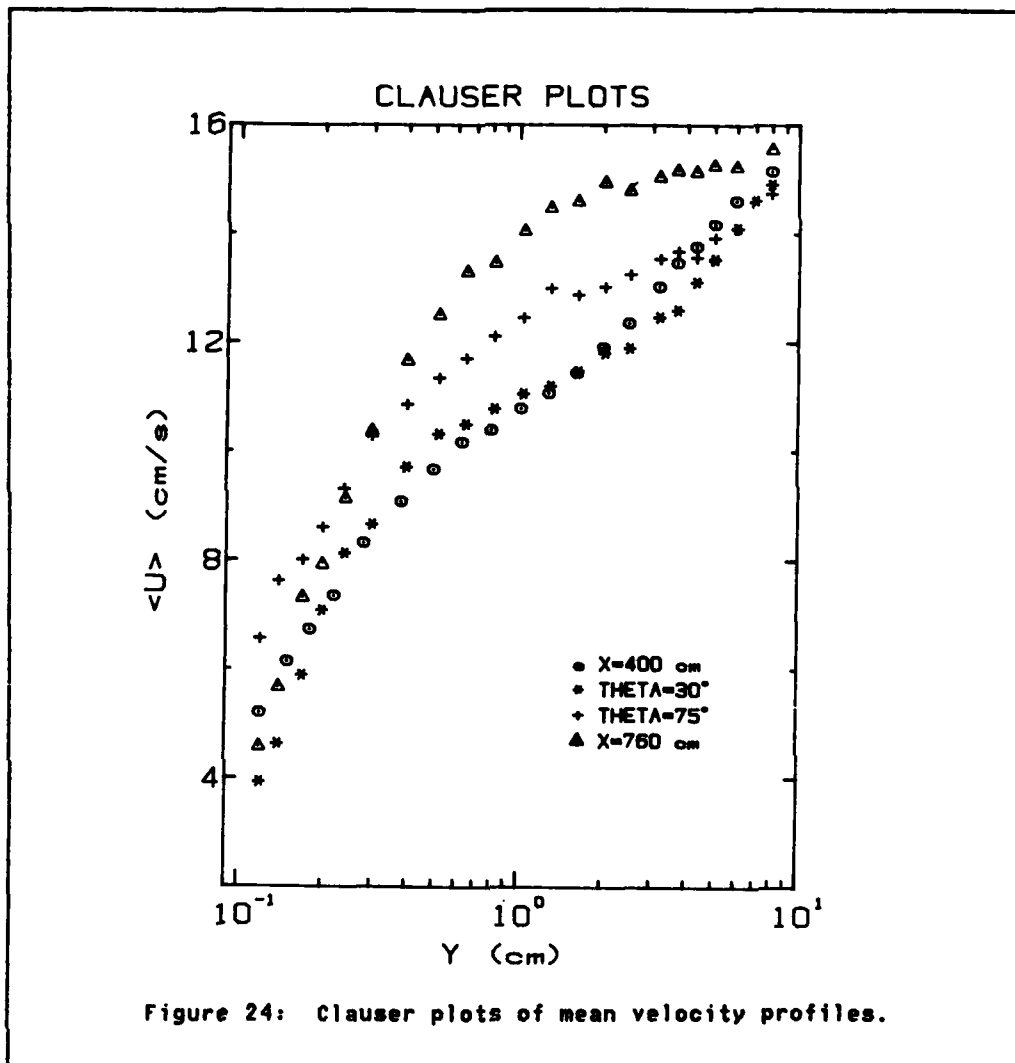
(±0.05 cm) makes comparison of points near the wall risky. Logarithmic regions are evident in the flatplate, 30°, and 75° profiles but not in the 760 cm profile. However, on the basis of the Clauser method, the slope of the log region in the profile at 30° implies a lower skin friction than that for the upstream flatplate. We believe the actual skin friction on the concave wall to be higher than that on the flatplate and

- 57 -

tentatively conclude that the usual correlation relating the log region with the skin friction may not be applicable to the log regions visible in the concave wall profiles in Fig. 24.

Figure 25: Typical velocity profiles from Smits et al (1979).
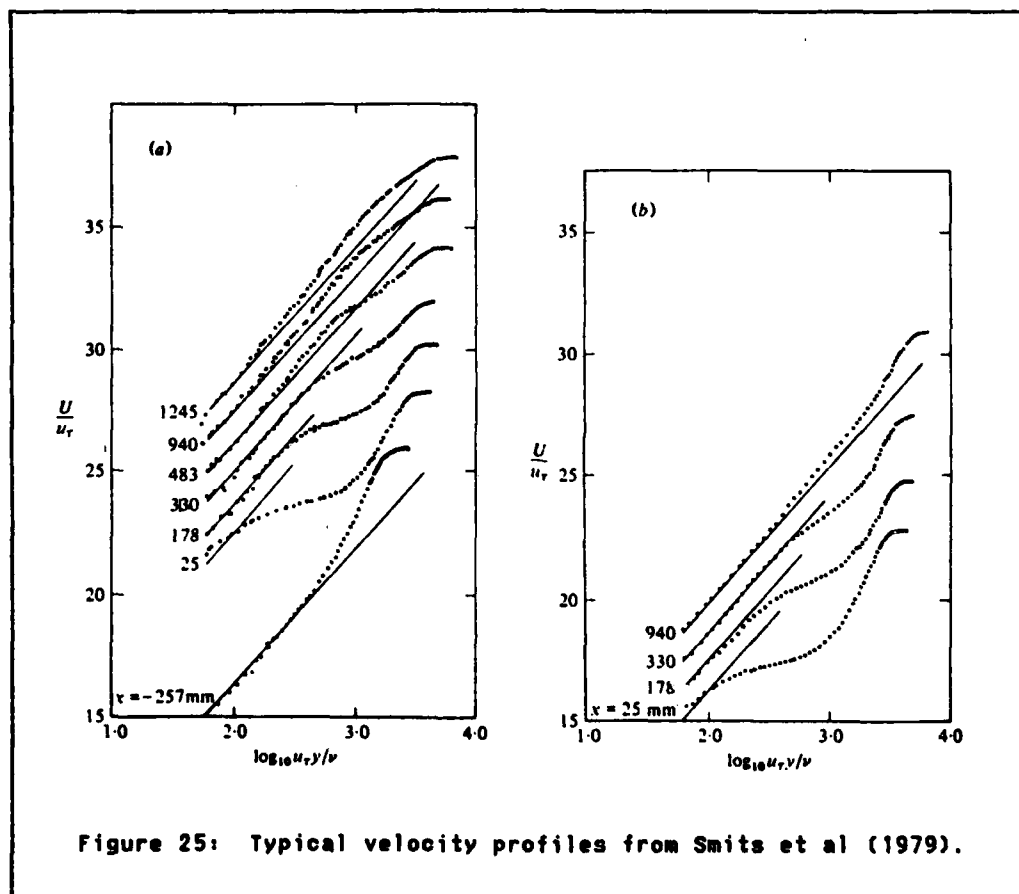
The effects of concave curvature on the Law of the Wall found in the present study bear some similarity to the results of previous investigators such as Ellis & Joubert (1974), So & Mellor (1975), Smits et al (1979), and Hoffmann & Bradshaw (1981). Although the profiles in their

studies retain the usual logarithmic region near the wall, (due in part
to the higher Reynolds numbers at which their tests were done), the wake
regions of their profiles all show a tendency to undershoot the usual
Law of the Wall. Fig. 25 shows mean velocity profiles taken from the
study of impulsive curvature of Smits et al (1979). (Their channel had
a sharp 30^0 bend in it at x=0 mm. Profiles in (a) were taken at a span-
wise location where c_f was a maximum; profiles in (b) were taken where
c_f was a minimum. The scale on the left applies only to the lowest
curves. The left-hand end of the log-law line marks $U_0/u^*=15$ for the
other curves, which are staggered.) In the 30^0 profile of the present
study, it appears as though the region from y=0.5 to 2.0 cm may actually
be part of this undershooting and should not be thought of as the usual
log region. Further discussion of this behavior is given in the next
chapter.

3.2   VISUAL RESULTS

Extensive visualization surveys of the flow were taken using dyes and
hydrogen bubbles. In addition to surveying the turbulent flow field, we
also visualized a laminar boundary layer on the concave wall to see if
we could obtain the classical Taylor-Görtler vortex flow.

3.2.1   Laminar Flow

In order to achieve the proper conditions, the velocity had to be low
enough so that transition did not occur. However, too low a velocity
resulted in the development of a strong secondary flow pattern due to
the boundary layer on the channel floor. This secondary flow dominated

the entire curved portion of the channel, resulting in flow angles approaching 45° on the test wall. By running the channel fast enough to maintain a turbulent boundary layer on the floor but slow enough to prevent transition on the test wall, we were able to produce a nominally two-dimensional laminar boundary layer on the test wall. The mean velocity under these conditions was about 5 cm/s, and the boundary layer was about 4 cm thick at the start of curvature.

The flow was visualized by injecting dye through the wall slots. Dye coming out of the first dye slot, chosen to be upstream of curvature, formed a uniform transparent sheet. As the sheet entered the curve, it coalesced into several very narrow discrete streamers, the result of Taylor-Görtler vortices. Dye injected through a second slot 30° into the curve coalesced within a few centimeters. The first time this test was performed, the streamers were evenly spaced about 10 cm apart and tended to be quite stable (see Fig. 26a). In a subsequent experiment, the spacing was not nearly as uniform. The reasons for this nonrepeatability are not clear at this time, but the transitional nature of this flow would seem to make it very sensitive to upstream flow conditions. During the second experiment, the channel had to be narrowed 3 to 4 centimeters in order to impose a favorable pressure gradient to delay transition.

An interesting feature revealed by the dye was a secondary instability which sporadically developed out of the primary Taylor-Görtler cells. Occasionally, the low-speed fluid brought away from the wall by the roll cells would interact with the outer flow, forming a horseshoe vortex street (see Fig. 26b). Similar structures were observed in the
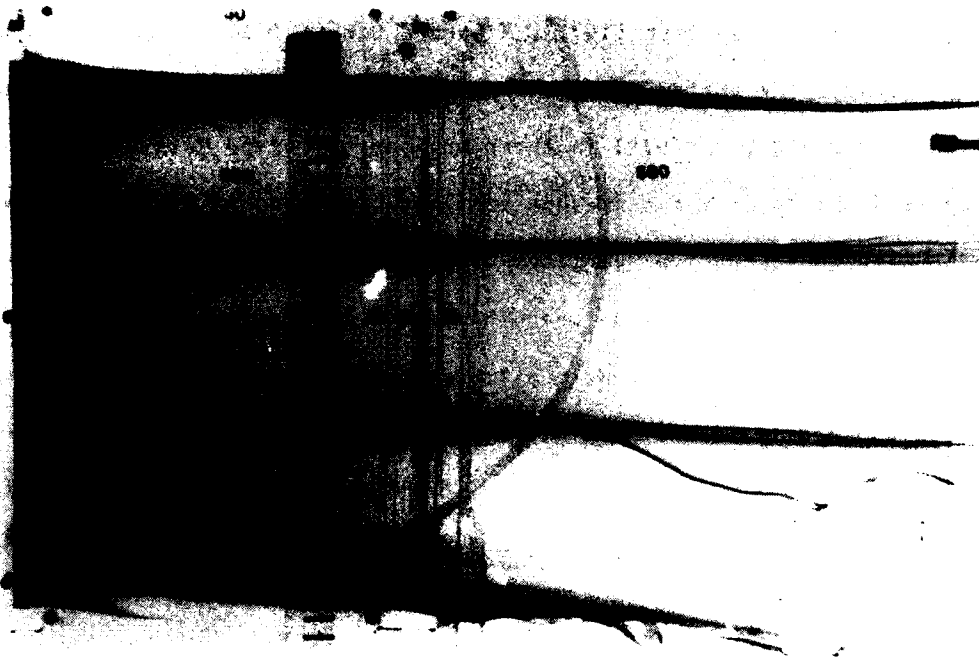
(a)
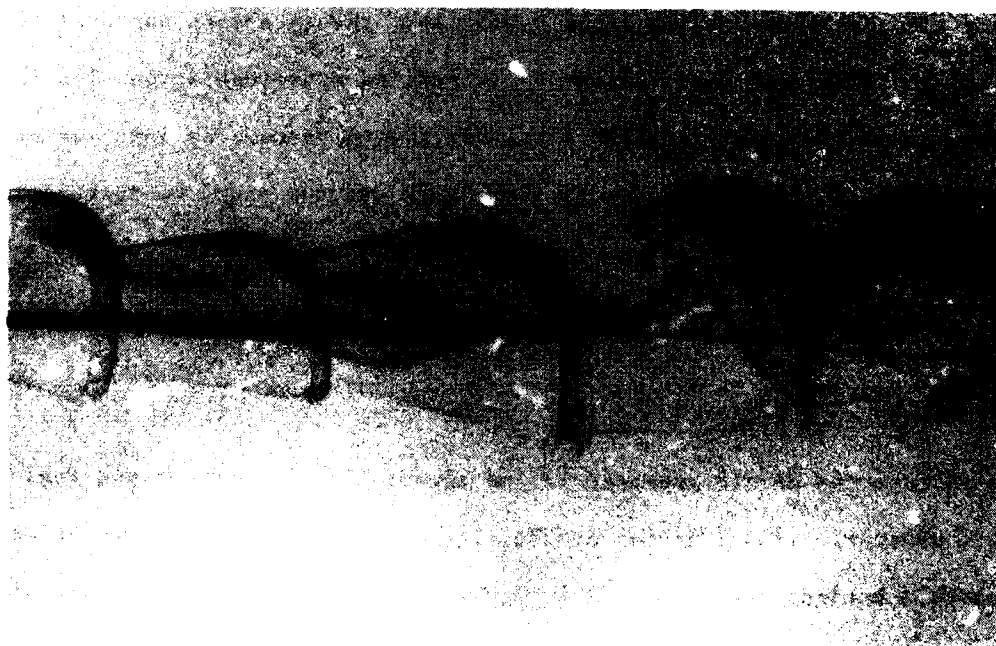
(b)

Figure 26: Dye visualization of Taylor-Görtler vortices and secondary instability.

studies of Bippes & Görtler (1972), Aihara & Sonoda (1981), and Aihara & Koyama (1981). The vortex streets also resemble the coherent structures studied by Perry & Lim (1978) in their work on coflowing jets and wakes. The spanwise width of the horseshoe vortices was roughly 5-7 cm and the spacing between successive vortices was roughly 4-5 cm. Evidentally, the tube-like shear layer between the high- and low-speed fluids was rolling up as a result of a Helmholtz-type instability. The resulting vortices would drift downstream at velocities close to that of the free-stream, occasionally pairing before breaking down into turbulence. Although these vortex streets usually formed within a few centimeters of the wall, some of them appeared almost at midchannel.

The vortex streets appeared at irregular intervals, forming for several seconds then washing away. Usually, the streamers appeared to develop a transverse oscillation of increasing magnitude which led to breakdown. Only "quiet looking" streamers seemed to develop into vortex streets. Since the primary aim of this work was the study of turbulent boundary layers, we did not pursue the investigation of laminar instability any further.

3.2.2 Turbulent Flow

Flow through the nozzle appeared to be acceptably rectilinear and laminar. However, visualization of the flow over the boundary layer trips revealed a curious phenomena. The recirculation region on the upstream side of the trip was apparently unstable in the spanwise direction. Every few centimeters, the fluid trapped in the recirculation vortex would find its way over the trip as shown in Fig. 27. The recirculation

- 62 -

Figure 27:   Schematic of flow over boundary layer trip.
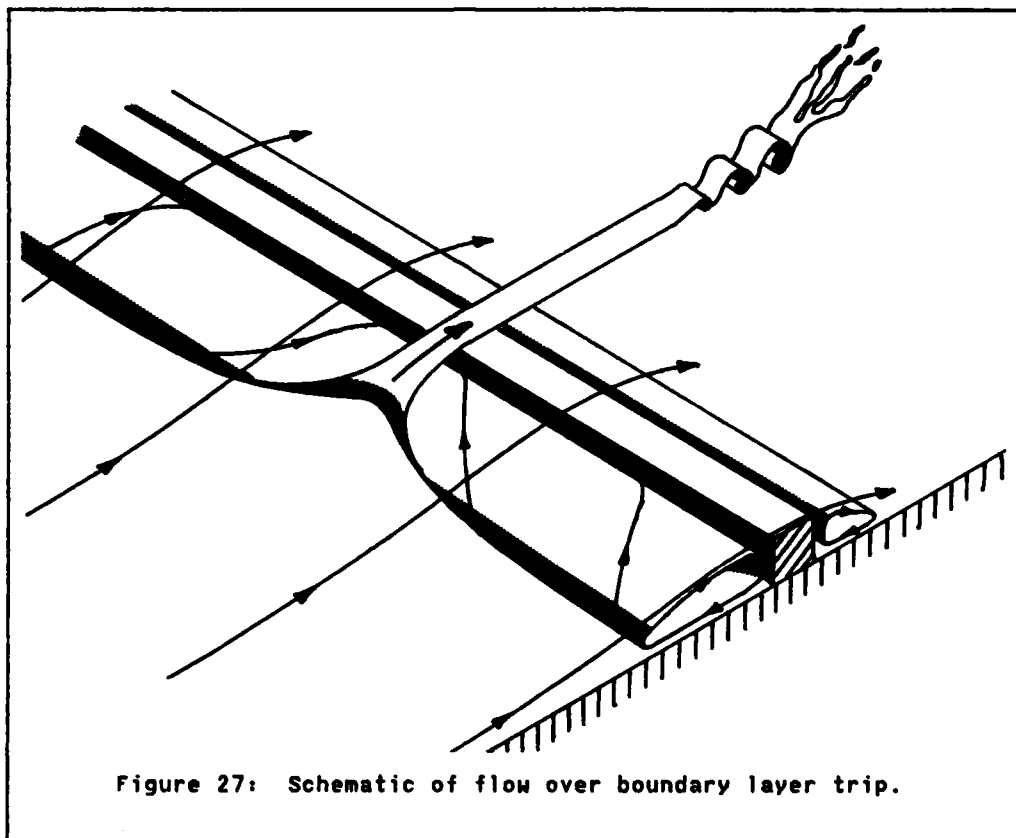
region therefore appeared segmented and three dimensional. The pattern

of "breakthroughs" was very steady, although large disturbances would

cause the pattern to change and "lock in" to a new arrangement. More

detailed flow visualization revealed that the actual volume of fluid

involved in the breakthroughs was very small and that the effects of

transition downstream of the trip obliterated all visual evidence of the

nonuniformity. No signs of the nonuniformity were apparent in the span-

wise velocity profiles taken farther downstream.

Because turbulent flow is strongly three-dimensional and time-dependent, it is almost impossible to completely document it for future analysis. The best we could do was to take motion pictures of the flow, selecting the camera angle to optimize the visual effects of the three-dimensionality. A summary of our results is contained in the film, "Turbulent Boundary Layers on Concave Walls," available on loan. The film contains footage of dye and hydrogen bubble visualization of the flow in the inlet, curved, and recovery regions. A detailed scene-by-scene narrative may be found in Appendix F. Representative still photos are shown in Figs. 28, and 30-33. The geometry of the hydrogen bubble photos is depicted in Fig. 29. The solid horizontal lines represent the locations of the hydrogen bubble wires, which are invisible in the actual photos. The dotted lines are located at the same y values as the wires, but at the mean x location of the bubble lines. Each group of hydrogen bubble pictures shows the wire(s) at different distances from the wall. The numbers to the right give the y values of the wires in centimeters. In the case of the discrete bubble lines, the photos show the bubbles about 0.57 sec after the wire was pulsed. Due to the mirror arrangement used, the flow is predominantly out of the page but slightly canted towards the lower left hand corner. What follows is a description of the flow field based on still photos, movies, and actual observations.

The flat plate boundary layer upstream of the curve at $x=460$ cm exhibits the usual pattern of streaks and bursts discovered by Runstadler & Kline (1959). With the bubble wire at $y=0.5$ cm, $(y^+=30)$ the streaks appear as narrow regions of low velocity fluid which oscillate transversely. The mean streak spacing was determined by manually

- 64 -
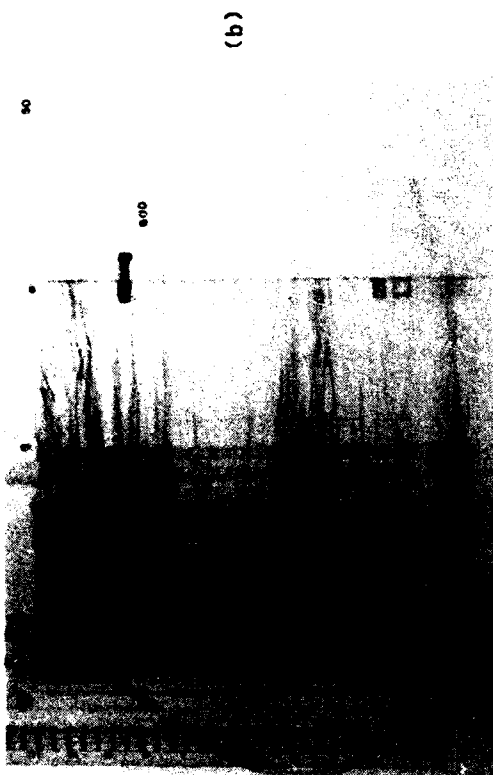
Figure 28: Dye visualization in (a) inlet, (b) curve, and (c) recovery.

Figure 29: Guide to hydrogen bubble pictures.
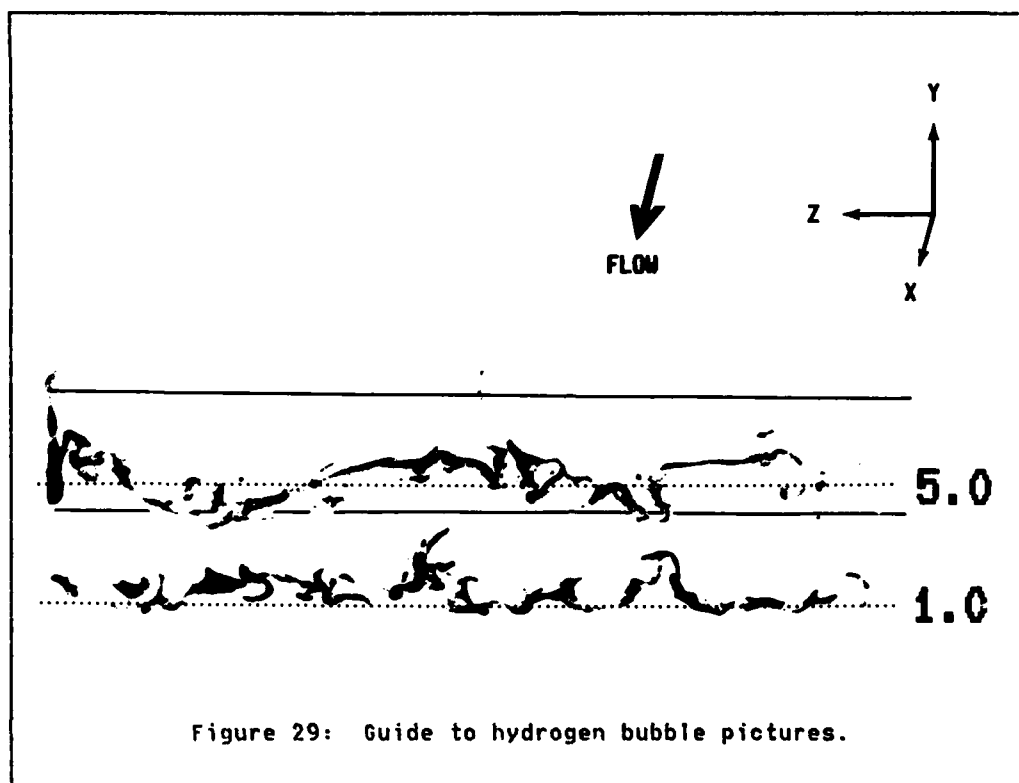
analyzing dye pictures and found to be 1.51±0.16 cm. Using the friction velocity calculated at midspan of 0.68 cm/s, this corresponds to a λ^+ of 103±11, which agrees well with the generally accepted value of 100 [Cantwell (1981)]. In addition, longitudinal vortices near the wall are occasionally seen. The typical length scale of these structures and the other eddies present in the flow is about 1 to 2 cm. The intensity of turbulent activity seems to diminish monotonically as one moves away from the wall; the bubbles at $y=2$ cm appear to be steady and almost laminar except for occasional small travelling disturbances associated with the intermittency at the edge of the boundary layer.

9.0

5.0

5.0

1.0

0.5
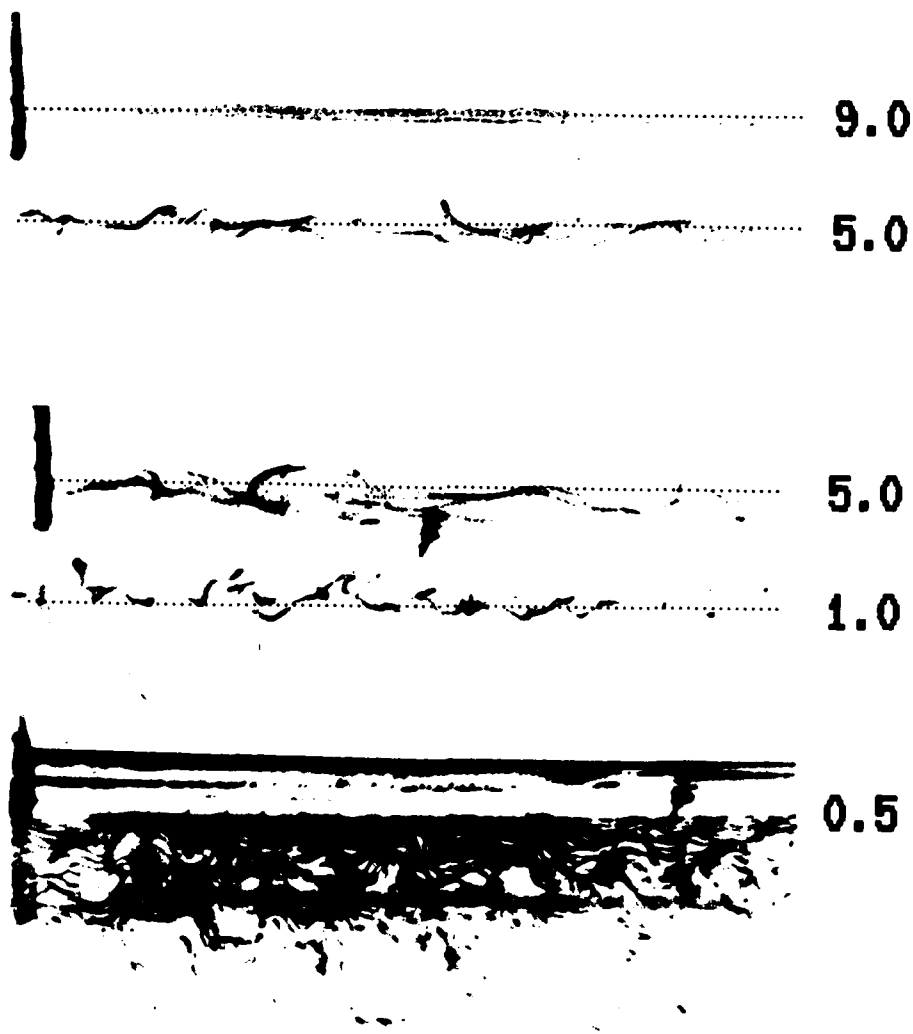
Figure 30:   Hydrogen bubbles at x=400 cm, inlet.

9.0

9.0

5.0

5.0

1.0

0.5
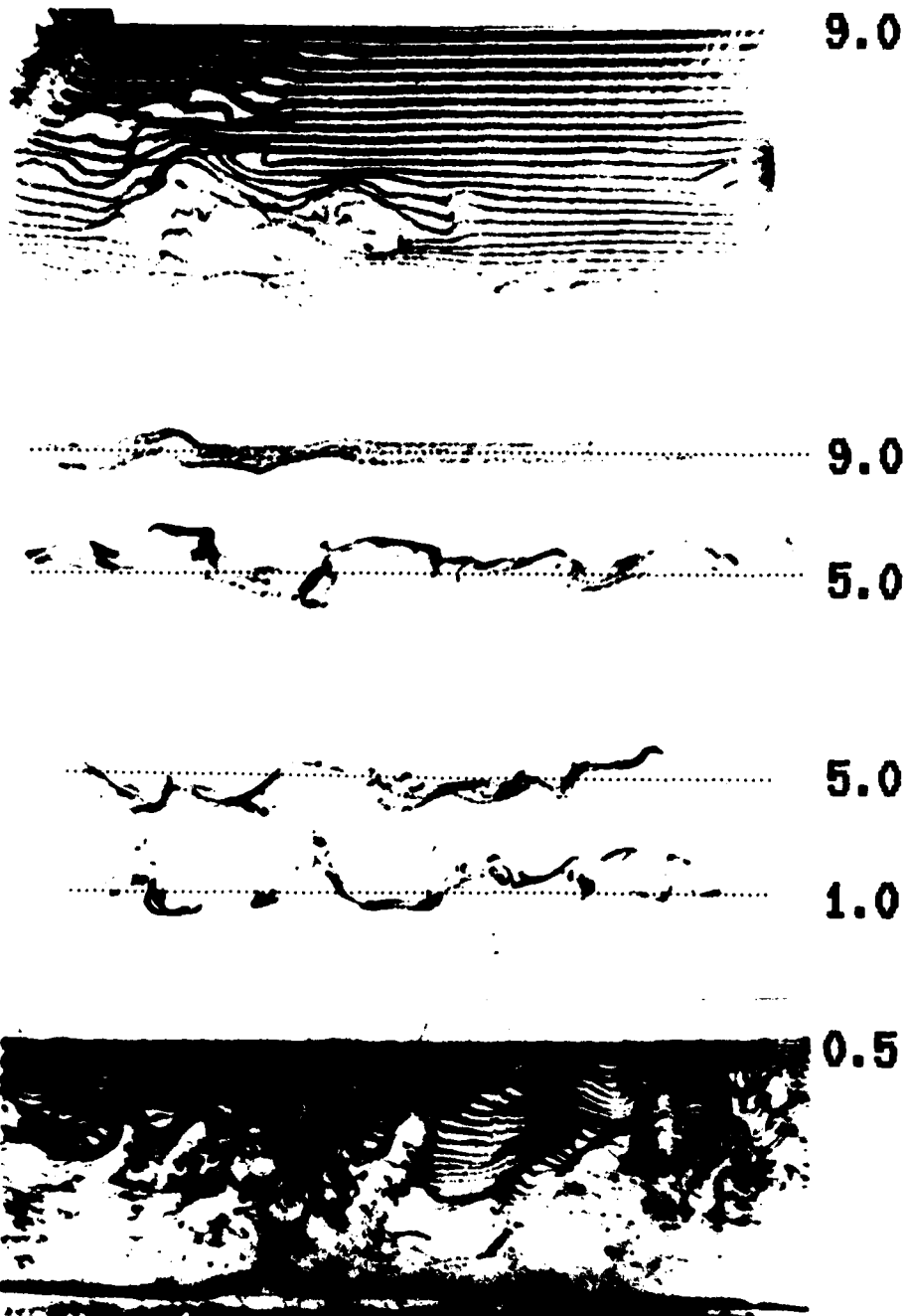
Figure 31: Hydrogen bubbles at 20⁰.

9.0

9.0

5.0

5.0

1.0

0.5
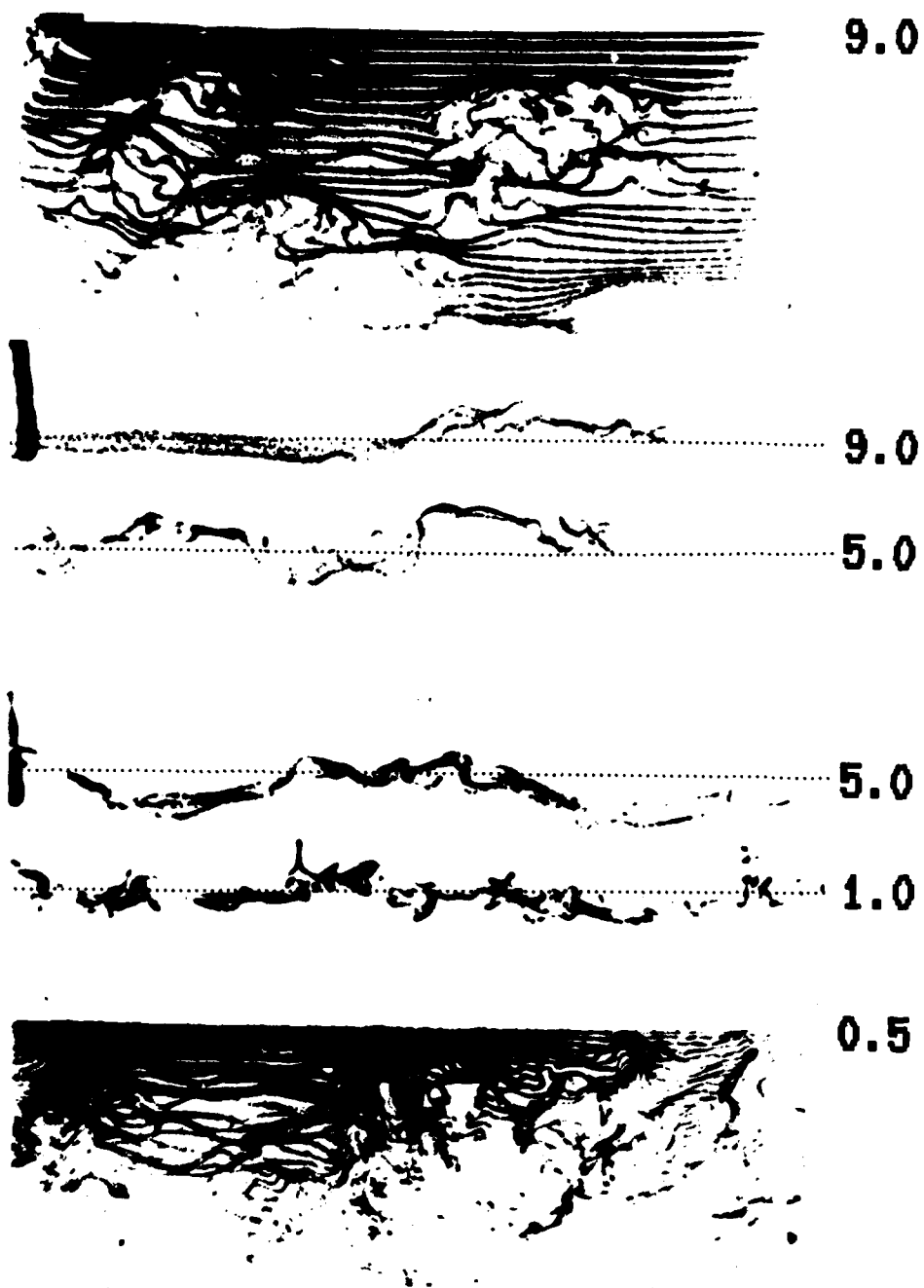
Figure 32: Hydrogen bubbles at 50°.

9.0

9.0

5.0

5.0

1.0

0.5
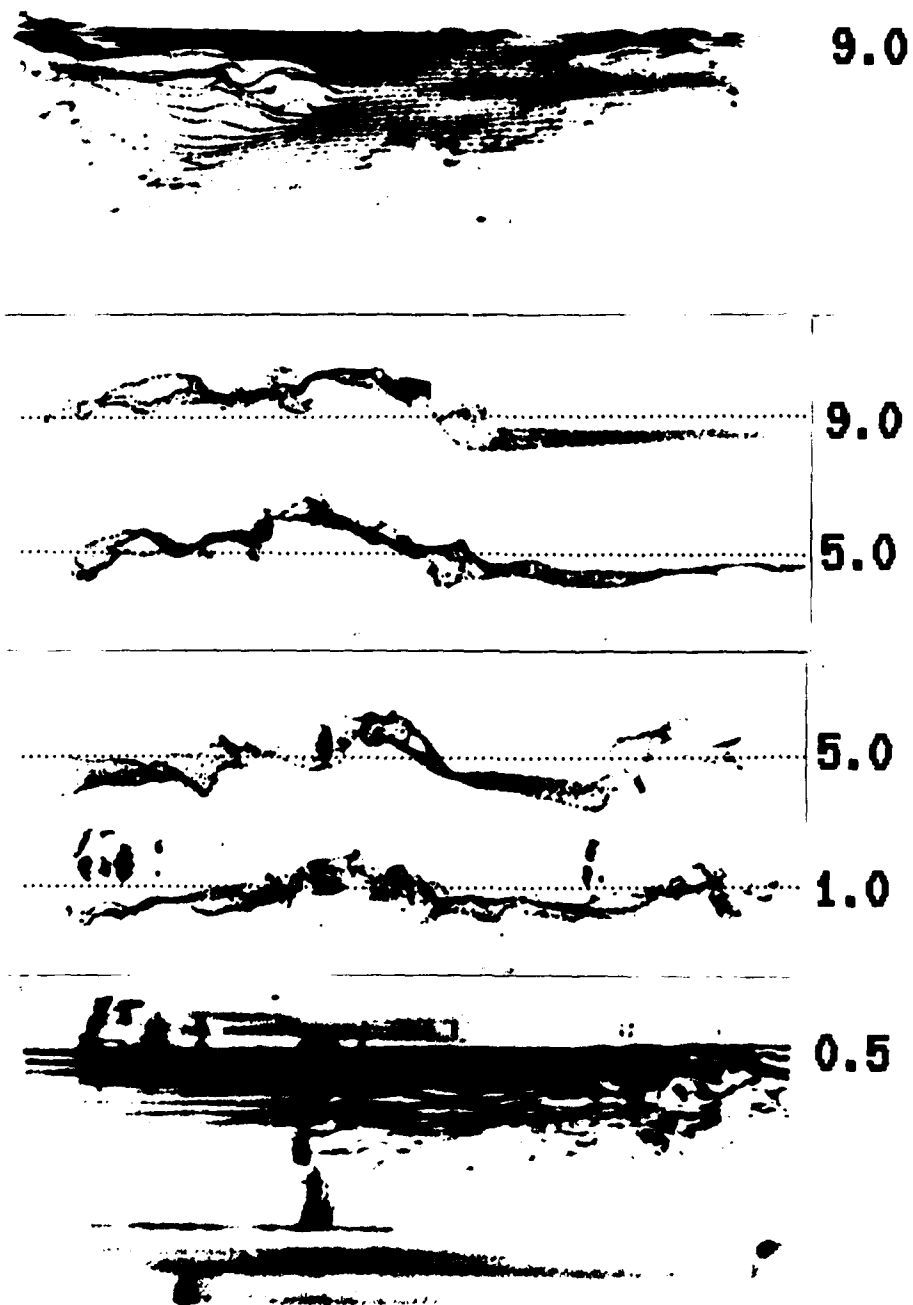
Figure 33:   Hydrogen bubbles at x=730 cm, recovery.

By about 20° into the curve, the boundary layer appears markedly dif-
ferent from that on the flat plate. The boundary layer is about 10 cm
thick at this station. Near the wall, streaks are still present, but
they are frequently swept aside or squashed by large-scale inflows or
sweeps, with spanwise dimensions on the order of 4 cm and streamwise
lengths of about 10 to 15 cm. The streaks and their surrounding fluid
are pushed into piles and the usual near-wall bursting process appears
to be mostly suppressed. Small longitudinal vortices are occasionally
seen at the interface between the high-speed inflows and the low-speed
wall fluid. Bubbles farther from the wall show that the low-speed col-
lections of fluid are squeezed or ejected away from the wall by the
sweeps and frequently make their way out to the potential core. Dual
bubble lines 4 cm apart in the y-direction show that vertical motions
are often correlated across the boundary layer. Planar visualization
with one bubble wire pulsed continuously near the wall or near the edge
of the boundary layer (y=9 cm) shows that the ejections and sweeps occur
randomly in space and time. The impression one gets from viewing the
actual flow is that the sweeps are somewhat more coherent and appear to
be responsible for the ejections, which seem to form as a result of the
sweeps. Small vortices are also present at the edges of the outflowing
bulges of the ejections as they penetrate the core. Careful observation
shows gentle streamwise circulations which extend over the entire bound-
ary layer taking place. However, these weak roll cells, reminiscent of
but weaker than the roll cells indentified in the related work by John-
ston et al (1972) in a rotating channel, appear to be more a result of
the sweeps and ejections than independent flow modules themselves.

As the flow proceeds downstream, its qualitative features as described above remain the same. However, the boundary layer gets thicker, and the crossplane movements of fluid increase in speed and extent. Intermittent values of v and w are often on the order of 4 cm/s or 25% of the mean channel velocity.

Near the downstream end of curvature and in the recovery region following the concave wall an additional flow characteric becomes evident. Large (10 cm) patches or globs of laminar-like fluid appear throughout the boundary layer, interspersed within the large-scale motions remaining from the preceeding curvature.

To assist in interpreting these visual results a computer simulation of streaklines and timelines was performed. This simulation is discussed in the following chapter. Interpretations of these observations are then given.

3.3 SUMMARY OF MAIN RESULTS

Although there was minor spanwise nonuniformity in the inlet section boundary layer, the flow was considered acceptable for the present qualitative study. The boundary layer upstream of the curved section appears to be a normal, zero-pressure-gradient flat plate boundary layer with a momentum thickness Reynolds number of about 1300. The streak spacing agrees with the generally accepted value of 100 wall units, and the boundary layer appears normal in the flow visualizations.

Once in the curved section, the appearance of the boundary layer is changed by the presence of large-scale sweeps and ejections. The sweeps

are typically about half a boundary layer thickness in span and appear
to be coherent over the height of the boundary layer.   The streamwise
extent of the sweeps is difficult to ascertain using the present methods
of visualization but is estimated to be several boundary layer thick-
nesses. The sweeps appear randomly in space and time over the concave
wall. Although no stationary pattern is observed, the sweeps are spaced
about one boundary layer thickness apart, on the average, in the span-
wise direction.   Fluid near the wall is displaced by the sweeps and
ejected away from the wall. Bursting appears to be inhibited in the
regions underlying the sweeps.

The random occurrence of the sweeps and ejections is supported by
velocity and turbulence intensity profiles obtained by traversing in the
spanwise direction; nothing in these profiles suggests that the large-
scale sweeps and ejections occur in preferred locations.   Traverses
across the height of the boundary layer reveal fuller velocity profiles
and higher values of turbulence intensity, especially in the outer
layer. These results confirm the visual observations, which indicate an
increase in mixing due to the large-scale sweeps and ejections.

The modification of the velocity profiles by concave curvature fol-
lows a trend apparent in the studies of earlier investigators. Concave
curvature seems to cause the outer layer profile to undershoot the usual
Law of the Wall, resulting in an attenuation or elimination of the usual
logarithmic region.

Chapter IV

DISCUSSION

4.1   SIMULATION AND INTERPRETATION OF FLOW VISUALIZATION

Flow visualization of an unsteady flow by fluid marking has a major

drawback, namely, the fluid markers show a time integrated picture of

the flowfield since the current position of each marker depends on its

prior history. In steady flows streaklines, streamlines and pathlines

are identical, but this cannot be said of unsteady flows. The human eye

and mind are able to integrate and interpret streak and pathline pic-

tures to a limited extent. Thus when viewing a flow, some useful inform-

ation regarding the instantaneous velocity distribution can be

extracted. However, there is still a tendency for the eye to make erro-

neous conclusions based on some of the shapes formed by the markers. In

order to help interpret the visualization data in the present study and

to try out some simple models of the flow field, a computer program was

developed which is capable of tracing fluid markers (e.g. streak and

timelines) in a prescribed three-dimensional, time-dependent velocity

field. The results, when displayed graphically and compared with actual

visualizations of the flow, give an idea of what the actual velocity

fields may be like.

Given a known Eulerian velocity field, for example $\bar{u}(\bar{x}, t)$, and a

fluid marker which is identified by it intial position at time t=0, $\bar{X}_0$,

the position of the marker, $\bar{X}(t)$, is given by solving the differential

equation:

- 74 -

$$\frac{d\overline{X}}{dt} = \overline{u}(\overline{X}, t),$$ (4.1)

subject to the initial conditions $\overline{X}(0) = \overline{X}_0$.

In the present study, a velocity field resembling a Taylor-Görtler velocity field was prescribed:

$$u = U_0 - v'y$$ (4.2)

$$v = \frac{-2V_0 hy}{h^2 + y^2} \cos(k_z z) \cos[k_x(x - ut)]$$ (4.3)

$$w = \frac{2V_0 h(h^2 - y^2)}{k_z(h^2 + y^2)^2} \sin(k_z z) \cos[k_x(x - ut)]$$ (4.4)

where

$$k_i = \frac{2\pi}{\Lambda_i}, \quad i = x, y, \text{ or } z.$$ (4.5)

This flow field satisfies continuity, but it is not irrotational. The intent here is not to propose a realistic model of an actual flow field but to see how fluid markers behave in a hypothetical flow field which has some similarities to an actual flow.

The flow described by Eqs. 4.2-4.4 consists of an array of counterrotating roll cells adjacent to a wall, each of width $\Lambda_z/2$, with solid body rotation in the center of each cell at height h. At the corners of each cell there is stagnation point flow (see Fig. 34). The maximum vertical velocity, V_0 and occurs at a height h on the vertical line separating adjacent cells. The streamwise (u) velocity consists of a constant velocity, U_0, plus a shear, v'. The shear is used in an attempt to reproduce the fact that flow moving towards the wall has a higher u

Figure 34: Cross-plane streamlines for simulated velocity field.
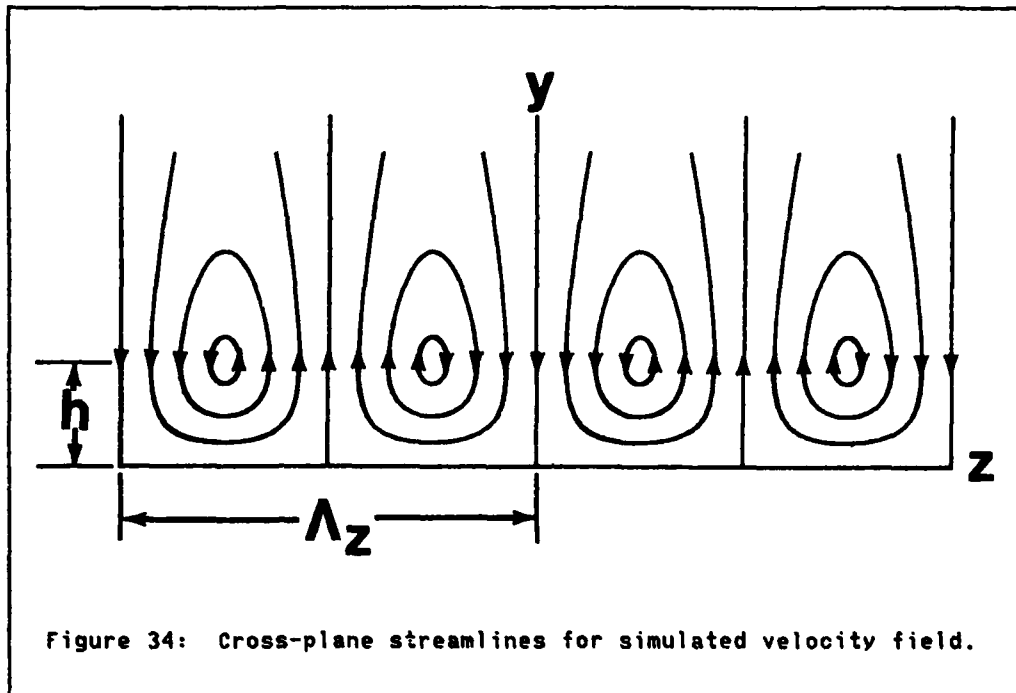
velocity than flow moving away from the wall. The cosine terms at the
ends of the expressions for v and w modulate the amplitudes of the
cross-stream velocities so that the cells are of limited streamwise
extent and travel downstream as coherent entities, like travelling
waves.

The differential equations represented by Eq. 4.1 were solved using a
fourth order Runge-Kutta ODE solver given by White (1974). Subroutines
were written to display the results in true perspective.

The resulting velocity field causes computed time-streak markers to
behave as shown in Figs. 35 and 36.   Each cell is 5 cm wide (Λ_z=10 cm)
and 10 cm long (Λ_x=20 cm)   with a core set at h=2.5 cm from the wall
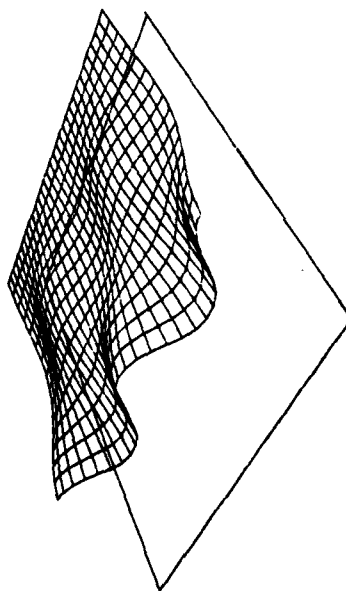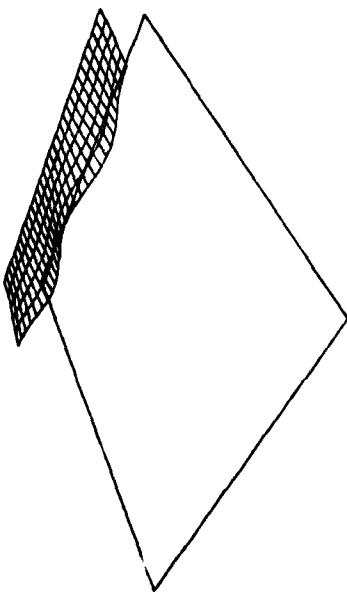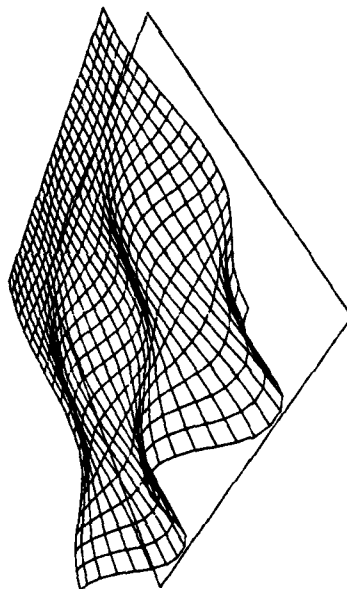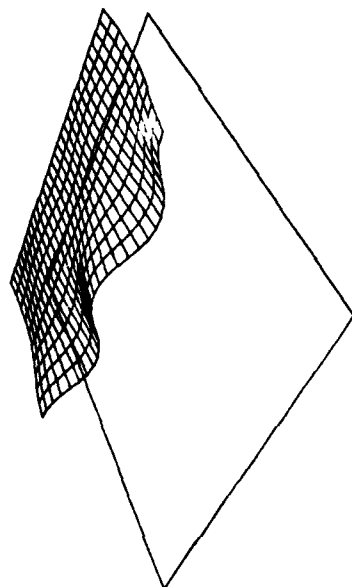
Figure 35: Evolution of simulated time/streak markers with time.
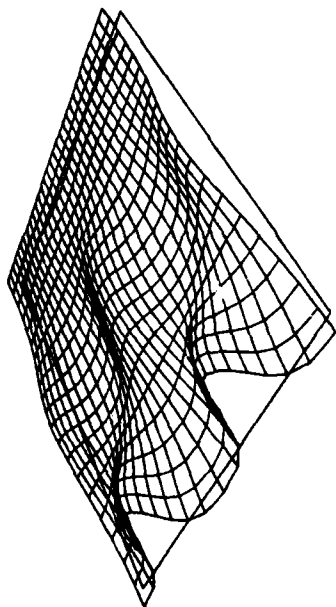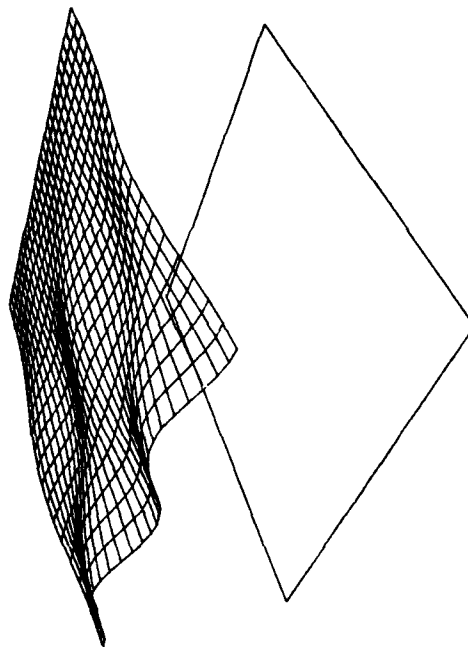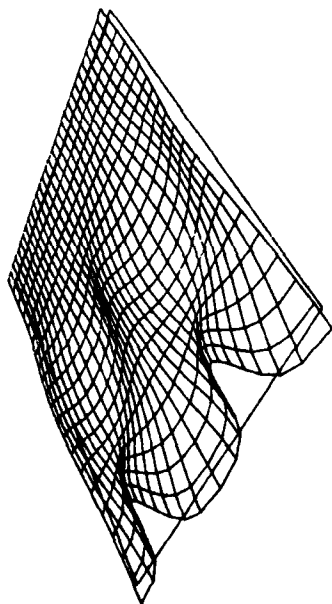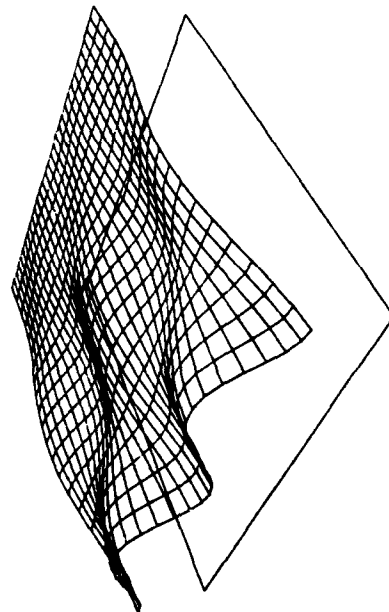
Figure 36: Appearance of simulated time/streak markers generated at (a) 0.5, (b) 1.0, (c) 5.0, and (d) 10 cm from base.

(units are arbitrary). The base plane is 20 cm square. U_0, the velocity at y=0, is 11 cm/s, and the shear v' is chosen so that the velocity at the height of the marker generator is 10 cm/s in all cases. In this way, there is less of a vertical velocity gradient for markers placed farther from the wall, as is the case in the actual flow. The maximum vertical velocity, V_0, is 4.0 cm/s. The values for these parameters roughly approximate the actual observed characteristics of the flow while at the same time simplifying the display of the results. Fig. 35 shows a sequence of views at consecutive times with the generator at y=2.5 cm. Note the development of the the "structures" as they proceed downstream. Fig. 36 has the generator at y=0.5, 1.0, 5.0 and 10 cm, all at the same time. If we imagine some random turbulence superimposed on the simulated flow field (Figs. 35 & 36), the result is qualitatively similar to the flow actually observed (Figs. 31-33).

The simulation exhibits several of the features observed in the actual flow field and helps explain how some of those features may appear. One of the more striking resemblances of the simulation to the actual flow is the narrowness of the outflows (ejections) for markers placed near the wall (Fig. 36a). The simulation demonstrates that such outflows are simply a result of the combined movements of the markers and are not necessarily indicative of narrow, jet-like ejections in the velocity field. Another feature the simulation helps clarify is the streamwise development of the large-scale structures. The markers make it appear as though the structures are larger downstream of the wire when in fact we know the prescribed velocity field is uniform aside from the periodic fluctuations. The assumption of a slow streamwise

- 79 -

2/2
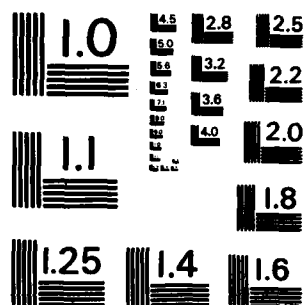
MICROCOPY RESOLUTION TEST CHART
NATIONAL BUREAU OF STANDARDS-1963-A

development of the actual flow field is supported by the observation that similar structures appear at all locations in the curve. The variations in shape of the different timelines in the real flow is due to the random distribution of the "cells" and the different positions, relative to these "cells", at which bubbles are injected. In fact, "cells" is probably not a good word to describe the regions of inflow and outflow in the actual flow since planar visualization (in the x-z plane) shows them to be multiply-connected domains of irregular shape and size.

4.2   PHYSICAL CONSIDERATIONS

Most previous investigators [e.g. Tani (1962), So & Mellor (1975), Hoffman & Bradshaw (1981)] have reported stable longitudinal flow structures in the boundary layer on a concave wall and have concluded that a stationary array of counterrotating *turbulent vortices* exist there, analogous to the Taylor-Görtler vortices observed in a laminar boundary layer. Clearly, our flow is also dominated by large-scale structures, the difference being that our structures have less coherence and are distributed randomly over the wall. To see why this might be so, let's examine current knowledge about the fluid dynamics.

Various stability criteria lead one to expect flow with streamline curvature to be unstable to disturbances in the plane of curvature if a certain velocity gradient exists. Görtler (1954) and others have done detailed analyses to determine the exact conditions for instability in a laminar boundary layer assuming that the initial disturbances would take the form of vortices. It is important to keep in mind the other assumptions made in these analyses. The initial boundary layer is steady,

laminar, and two-dimensional. The initial disturbances are assumed small so that linearization of the equations is possible. The theory says nothing about how the flow will behave as the disturbances grow. In fact, our own laminar flow experimental studies as well as those of Bippes (1972), Aihara & Sonoda (1981), and others, have demonstrated that as the vortices develop, a secondary instability occurs in the shear layer between the low-speed fluid transported away from the wall and the high-speed outer layers, leading to eventual breakdown and turbulence.

Before moving on to discuss turbulent flow, it may be useful to examine the physical basis for the instability of curved flows. Newton's First Law says that an object in motion in a straight line will continue moving in a straight line unless acted upon by a force. In the absence of forces, a particle moving initially tangent to a wall with concave curvature will approach the wall and eventually collide with it. The same will happen even if there are forces on the particle, if those forces are insufficient to turn the particle (i.e. $F < mv^2/R$). Imagine a constant density fluid flow along a concave wall which contains a fluid particle with an abnormally high velocity. With its higher momentum, the particle will move in a path with less curvature than its neighbors and approach the wall. Continuity requires that the surrounding lower-speed fluid move away from the wall. How fast need the particle move to deviate from its neighbors in an unstable manner? For inviscid, constant density flow, Rayleigh's stability analysis and the Navier-Stokes equations show that potential flow is the condition for neutral stability, i.e. $Ur =$ constant. If the local velocity gradient exceeds that for a potential flow, the flow is unstable. For viscous flows, the conditions

- 81 -

are not so simple as Görtler demonstrated, but the basic idea is the same.

In turbulent boundary layers the fluid velocity varies randomly in space and time, although the mean is stationary. If a point function describing the local stability were defined, its value would also vary randomly throughout the flow. Hence, in a turbulent flow one would expect at any instant to see randomly distributed regions (in all three dimensions) of stability and instability. The size of the regions would depend in some way on the characteristics of the fluid and the statistics of the velocity. Furthermore, the velocity statistics would be continuously altered by the mixing of high- and low-speed fluid elements. Added to this picture is the structure of the boundary layer itself, manifested in streaks and bursts as in the basic case of flow over a flat wall. Nothing in this picture suggests the development of a stationary pattern of Taylor-Görtler vortices.

Why have so many other investigators discovered stationary flow patterns, e.g. Taylor-Görtler-like cells of long streamwise extent? Rig dependency must be seriously considered when dealing with instability phenomena. Remember that it is variations in velocity throughout the flowfield which govern the stability. It is therefore important to consider (a) how experimenters deal with the streamwise pressure gradient[7] associated with the onset of curvature, (b) how they control inlet conditions and secondary flows on endwalls, and (c) the geometry,

----

[7] Aihara & Sonoda (1981) showed that the onset of Taylor-Görtler vortices in a laminar boundary layer was delayed by a favorable streamwise pressure gradient.

particularly the aspect ratio, of the channel they employ to investigate the phenomenon. It is felt that the control of flow nonuniformities, by inlet screens for example (see comments in previous section), can have a very strong influence on the final outcome. Very small stationary span-wise disturbances generated by pore size nonuniformities in the inlet screens or other elements can propagate far downstream. Depending on their relative amplitudes and distributions, these disturbances can in fact trigger standing Taylor-Görtler-like cells in a turbulent boundary layer, as demonstrated by Hoffman & Bradshaw (1981). In conclusion, it appears that some of the previous experimental work may in fact be con-taminated by influences outside the control of the experimenters. In a number of cases these influences may be creating the stationary Taylor-Görtler-like cells that are apparently being observed.

4.3 PHYSICAL FLOW MODEL

The physical arguments given above, the results of the flow simulation, and the results of actual observation of the flow give rise to the fol-lowing suggested physical model for the flow. This model is advanced as a hypothesis which needs further verification.

Pockets of relatively high-speed fluid force their way towards the concave wall as sweeps, pushing aside low-speed fluid. The sweeps origi-nate as the random fluctuations in velocity associated with the large eddies in the outer flow. The spanwise width of the sweeps is on the order of half the boundary layer thickness, or about 500 y^+ units. Although they occur randomly throughout the boundary layer, the spanwise spacing of the sweeps is on the average comparable to the boundary layer

- 83 -

thickness. Furthermore, although the sweeps may initially be localized, inertial effects and the presence of a mean velocity gradient which is less stable* near the wall would tend to carry the sweeps all the way to the wall.

Sweeps impinging on the wall set-up regions of stagnation-like flow with appreciable transverse velocities. The sweeps push aside the low-speed fluid near the wall along with the streaks embedded in it. The severe distortion and acceleration that the fluid undergoes may inhibit streak bursting. Bursting is a phenomenon associated with the presence of streamwise vorticity and a pattern of low-speed/high-speed streaks in the wall layer. The streaks may not get a chance to form fully before they are disrupted by the large-scale sweeps. However, the turbulence intensity remains high in the wall layers because of contributions from the larger scales of motion and the shearing action between the sweeps and the low-speed wall layers which get caught between adjacent high-speed sweeps and are ejected away from the wall.

The ejection of low-speed fluid into the higher velocity regions appears to increase the turbulence production there with a consequent increase in turbulence intensity far from the wall. What appears to be a Helmholtz instability occurs in the narrow shear layers formed between ejections and sweeps; this may be the mechanism that enhances turbulence production throughout the boundary layer and could possibly be a process that keeps the overall turbulence levels higher than in a flat wall boundary layer even though normal bursting appears to be suppressed as

----

* Less stable in the sense that it represents a larger deviation from neutral stability, ur=constant.

described above.

It thus appears that these large-scale sweeps and ejections augment the effective Reynolds stress throughout the boundary layer[9] even though bursting near the wall may be suppressed. If this is true, one model or picture of the structure might be one of a magnified wall-layer-like sweep/ejection mechanism. Thus the boundary layer as a whole may have a structure similar to that in the zone $0 < y^+ < 30$ in a flat plate boundary layer but on a much larger scale. This would explain the modification or absence of a logarithmic zone in boundary layers on concave walls. This conjecture needs further study.

The actual flow is of course complicated by the random variations in sweep size, intensity, and location, and the interaction between the high and low-speed fluid elements. In fact, the sweeps and ejections are actually more like multiply-connected, intertangled regions in space which are constantly deforming as they drift downstream. Because of continuity, sweeps and ejections must give rise to localized regions where the flow is rotating. However, the extent, shape, and strength of these rotating bodies of fluid make it difficult to think of them as coherent structures in themselves. For this reason, the terms longitudinal vortices and roll cells seem inappropriate for describing this flow. However, the structural elements consisting of sweeps and ejections, random though they may be, seem to repeat themselves on a quasi-periodic basis and more adequately characterize the flow.

----

[9] The turbulence measurements of So & Mellor (1972) and Hoffman & Bradshaw (1981) support this remark, but additional quantitative measurements are needed to distinguish between turbulence production by bursting and turbulence production by sweep/ejection interactions.

It should be emphasized that the flow over the concave wall in this study is a developing one. The imposition of concave curvature on the flat wall boundary layer gradually transforms that layer into a boundary layer with a new equilibrium state governed by the large-scale sweeps and ejections. The behavior of the mean velocity profiles in the Clauser plots can be explained in terms of this picture of a developing flow.

The boundary layer growing on the flat wall of the inlet accumulates a relatively large amount of momentum-deficient fluid near the wall by the time it reaches the curved section. As the flow enters the curve, this low-speed fluid is ejected away from the wall by the large-scale sweeps. The incoming sweeps begin to establish a new equilibrium condition in which the ejection of low-speed wall fluid is limited by the rate at which fluid is decelerated near the wall by viscosity. Since the sweeps replace fluid near the wall with higher speed fluid from farther out, the mean skin friction increases. Meanwhile, the initial, large body of low-speed wall fluid migrates outward, away from the wall, gradually mixing with the surrounding fluid. In mean velocity profiles this mixing region is believed to correspond to a quasi-logarithmic zone with a slope less than that corresponding to the Law of the Wall. Fig. 37 shows the streamwise development of the mean velocity profiles with the quasi-log zones marked by line segments. (In the profile at 75°, a new logarithmic region may actually be present close to the wall.) Consequently, all conclusions from the present study may be said to represent only developing concave wall flow. In practice, regions of extended curvature seldom occur. Almost all real flows are therefore developing, and the present results and this flow model are of practical significance.

CLAUSER PLOTS

Figure 37: Clauser plots showing outward migration of quasi-logarithmic zone.
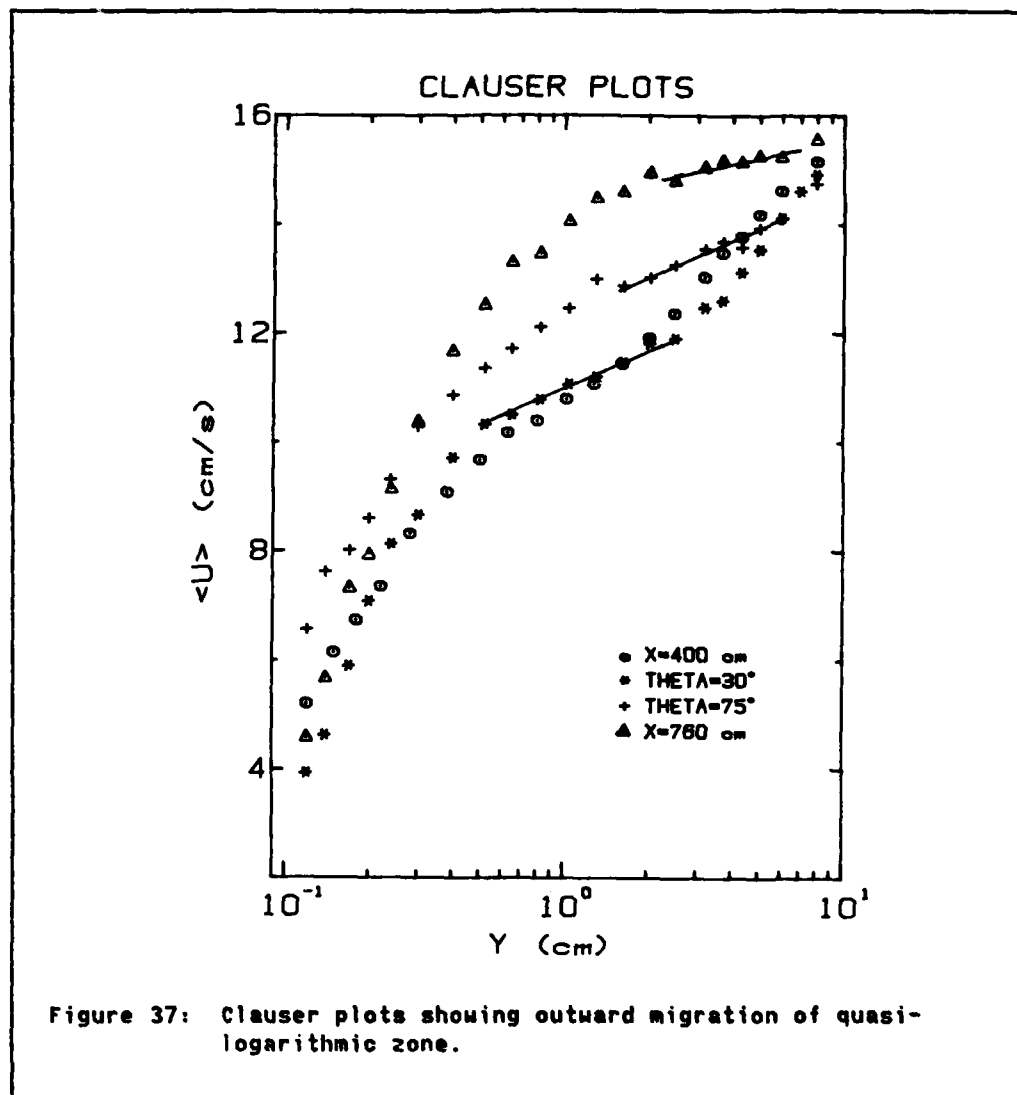
Finally, the behavior of the flow in the recovery region can be explained as follows: The vigorous mixing occurring in the curved region depletes the supply of low momentum fluid near the wall. When the flow exits from the curved section, the large-scale instability mechanism is turned off, and quite likely the flow studied here experiences a

favorable pressure gradient since separation on the opposing wall nullifies the effects of the channel expansion to some extent. The result is a new, thinner boundary layer growing on the flat, recovery region test wall. This layer has large-scale motions in the outer flow whose inertia makes them slow to decay as they are convected downstream from the curved section. The large pockets of laminar-like fluid seen near the wall may indeed be the results of local relaminarization in various parts of the boundary layer. The laminar-like pockets in the outer flow are probably chunks of the potential core which were entrained by the large-scale motions.

The flow model for the concave wall boundary layer points to large changes in the distributions of the sizes of the eddies which contribute to the turbulence as the flow goes from flat to concave wall conditions. The basic concave instability amplifies the outer layer scale of motion to create the sweeps which then interact with the wall layers and change their structure by pushing them into the outward ejections. Simple measurements of u' cannot reveal these changes. Although flow visualization gives a good qualitative picture, quantitative data of a much more detailed kind are needed. Space-time correlations of several velocity components would be particularly useful in determining the relative contributions of the large and small scales and how the distribution of these scales of motion changes as we go from a flat wall to a concave wall, and back again. None of the studies obtained to date, including our own, satisfy this requirement.

Chapter V

CONCLUSIONS

1. The results of the present experiment provide a much clearer pic-
    ture of the nature of the flow in turbulent boundary layers on
    concave walls.   This picture aids understanding of past experi-
    ments and should help guide the course of future studies.

    The following description of a turbulent boundary layer on a
    concave wall is proposed:

    a) The structure of the boundary layer appears to be dominated by
       large-scale sweeps and ejections.   These sweeps and ejections
       are coherent over the height of the boundary layer normal to
       the wall and are typically about half the boundary layer
       thickness in span.   The streamwise extent of the structures is
       of the order of a few boundary layer thicknesses. The struc-
       tures are distributed randomly over the wall and essentially
       travel with the mean flow with the sweeps moving faster than
       the ejections since they originate farther from the wall.   The
       spanwise locations of the structures are not stationary in our
       apparatus,[10] nor do the structures give rise to well-defined
       vortices or roll cells.

----

[10] Some past experiments by others did find stationary structures per-
     haps due to apparatus irregularities. The question of what determines
     fixed versus moving structures is not settled. See below.

The effect of the sweeps is to bring high-speed fluid from the outer flow closer to the wall. This action displaces the low-speed fluid near the wall which is ejected away from the wall. These large movements of fluid appear to inhibit the near-wall bursting process, the major turbulence production mechanism for flat wall flow. However, the interaction between the ejections and sweeps appears to create a Helmholtz instability of the shear layer between the high-speed sweeps and the low-speed ejections, and creates additional turbulence production throughout the rest of the boundary layer.

b) An effect of the large-scale sweeps and ejections is a fuller mean velocity profile which gradually develops through the curved region as the flow moves toward a new state of equilibrium. The usual Law of the Wall is either attenuated or eliminated by the onset of concave curvature; instead, a quasi-logarithmic zone appears which seems to correspond to the outward migration of the ejections created at the start of curvature.

c) The large-scale fluid motions induced in the curved boundary layer persist long distances after wall curvature has ended. The removal of low-speed fluid from the near-wall region in the curve causes the boundary layer in the recovery region to appear somewhat like a newly developing, laminar-like boundary layer with little near-wall bursting.

The present results lend credibility to those earlier investigations which failed to find evidence of large-scale structures in their measurements of mean quantities. This suggests the need for further work to determine under what circumstances the sweeps and ejections remain fixed in position. In particular, weak upstream disturbances, such as those introduced by screens, honeycombs, and trips may have contaminated several of the more recent studies, causing their large-scale structures to occur at fixed locations.

2. The present facility provides an acceptably uniform flow which can be adequately visualized. The flexibility inherent in the water channel's design should make the channel a useful tool for future investigations into a variety of flows. Much of this flexibility lies in the channel's ability to accept different test wall inserts. The large size of the outer channel allows the use of a wide variety of inner channel geometries. Another useful feature is the ability to produce laminar or transitional flows by varying the flow rate. More drastic modifications are also possible: the outer channel modules can be unbolted and reconnected in different configurations. Furthermore, should any of the modules become worn or damaged, they can be replaced relatively easily.

3. The computer controlled hot film probe enabled us to acquire velocity data with good repeatability in what would otherwise be an unfavorable environment for such an instrument. The largest uncertainty in the results was due to calibration uncertainty;

further refinements in the speed sensor of the instrument plat-
form could reduce this uncertainty.

Chapter VI

SUGGESTIONS FOR FUTURE RESEARCH

Future investigations of turbulent boundary layers on concave walls might profitably proceed along various paths, two of which are:

1. Obtain more detailed quantitative data on the flow. Suggestions include:

    a) Measurements of turbulent quantities, especially turbulent shear stress, obtained by conditional sampling employing simultaneous visualization to identify structural features.

    b) Measurements of space-time correlations to quantify the size of the large-scales of motion.

    c) Quantitative analysis of hydrogen bubble pictures by image processing to more accurately determine the shapes, sizes, and motions of the large-scale structures.

2. Attempt to resolve the role of upstream or other disturbances in determining the flow in the curve. A systematic study of the effects of various commonly encountered wind tunnel or water channel flow abnormalities (e.g. streamwise vortices or wakes from the inlet screens) can perhaps answer the question of why some of the flows contain stationary structures while others do not.

REFERENCES

Aihara, Y. & Koyama, H. (1981) "Secondary instability of Görtler
vortices," Trans. of the Japanese Society for Aeronautical & Space
Sciences, Vol. 24, No. 64, p. 78.

Aihara, Y. & Sonoda, T. (1981) "Effects of pressure gradient on the
secondary instability of Görtler vortices," Report No. AIAA-81-0197,
presented at the AIAA 19th Aerospace Sciences Meeting.

Bippes, H. (1972) "Experimental study of the laminar-turbulent
transition of a concave wall in a parallel flow," NASA Technical
Memorandum TM-75243. Translation of "Experimentelle Untersuchung des
laminar-turbulenten Unschlags an einer parallel angestromten konkaven
Wand," Heidelberger Akademie der Wissenschaften,
Matematischnaturwissenschafliche klasse, Sitzunsberichte, no. 3,
1972, pp. 103-180. NTIS N78-21442.

Blackwelder, Ron (1981) "Analogies between transitioning and turbulent
boundary layers," presented in the Leslie G. Kovasznay Memorial
Session, 34th Annual Meeting of the American Physical Society,
Division of Fluid Dynamics, Nov. 22-24, 1981.

Bradshaw, P. (1973) "The effects of streamline curvature on turbulent
flow," NATO Advisory Group for Aerospace Research and Development,
AGARDograph No. 169.

Cantwell, Brian J. (1981) "Organized Motion in Turbulent Flow," Annual
Review of Fluid Mechanics, Vol. 13, pp. 457-515.

Coles, D. E. (1969) "A young person's guide to the data," Computation of
Turbulent Boundary Layers - 1968 AFOSR-IFP-Stanford Conference, D. E.
Coles & E. A. Hirst, eds., Stanford University, Vol. II, pp. 1-17.

Clutter, Darwin W. & Smith, A. M. O. (1961) "Flow visualization by
electrolysis of water," Aerospace Engineering, Vol. 20, pp. 24-27,
74-76.

Eaton, J. K. & Johnston, J. P. (1980) "Turbulent flow reattachment: an
experimental study of the flow and structure behind a backward-facing
step," Report MD-39, Thermosciences Div., Dept. of Mechanical
Engineering, Stanford Univ.

Ellis, L. B. & Joubert, P. N. (1974) "Turbulent shear flow in a curved
duct," J. Fluid Mech. Vol. 62, Pt. 1, pp. 65-84.

Eskinazi, Salamon. & Yeh, Hsuan (1956) "An investigation on fully developed turbulent flows in a curved channel," J. of Aero. Sci., Vol. 23, No. 1, pp. 23-35.

Gillis, J. C., Johnston, J. P., Kays, W. M., & Moffat, R. J. (1980) "Turbulent boundary layer on a convex, curved surface," Report No. HMT-31, Thermosciences Division, Dept. of Mechanical Engineering, Stanford Univ.

Görtler, H. (1954) "On the 3-dimensional instability of laminar boundary layers on concave walls," NACA Technical Memorandum TM-1375. Translation of "Uber eine dreidimensionale Instabilitat laminarer Grenzschichten an konkaven Wanden," Ges. d. Wiss., Gottengen, Nachr. a. d. Math., Bd. 2, Nr. 1, 1940.

Hoffmann, P. H. & Bradshaw, P. (1981) "Turbulent boundary layers on concave surfaces," Imperial College of Science and Technology, private communication.

Hunt, I. A. & Joubert, P. N. (1979) "Effects of small streamline curvature on turbulent duct flow," J. Fluid Mech., Vol. 91, Pt. 4, pp. 633-659.

Johnston, D. S. (1959) "Velocity and temperature fluctuation measurements in a turbulent boundary layer downstream of a stepwise discontinuity in wall temperature," J. Appl. Mech., Vol. 26, p. 325.

Johnston, J. P., Halleen, R. M., & Lezius, D. K. (1972) "Effects of spanwise rotation on the structure of two-dimensional fully developed turbulent channel flow," J. Fluid Mech., Vol. 56, Pt. 3, pp. 533-557.

Klebanoff, P. S. (1955) "Characteristics of turbulence in a boundary layer with zero pressure gradient," NACA Report 1247.

Kline, S. J. & Falco, R. E. (1979) Summary of the AFOSR/MSU Research Specialists Workshop on Coherent Structure in Turbulent Boundary Layers. Report CSL-80-1 or AFOSR-TR-80-0290, Dept. of Mechanical Engineering, Michigan State Univ.

Meroney, R. N. & Bradshaw, P. (1975) "Turbulent boundary-layer growth over a longitudinally curved surface," AIAA Journal, Vol. 13, No. 11, pp. 1448-1453.

Moffat, Robert J. (1978) "Uncertainty Analysis," Report No. 111, Thermosciences Division, Dept. of Mechanical Engineering, Stanford Univ.

Morrow, T. B. & Kline, S. J. (1971) "The evaluation and use of hot-wire and hot-film anemometers in liquids," Report MD-25, Thermosciences Division, Dept. of Mechanical Engineering, Stanford Univ.

Patel, V.C. (1968) "Measurements of secondary flow in the boundary layers of a 180 channel," Aeronautical Research Council Report 30428.

Perry, A. E. & Lim, T. T. (1978) "Coherent structures in coflowing jets and wakes," J. Fluid Mech., Vol. 88, Pt. 3, pp. 451-463. Ramaprian, B. P. & Shivaprasad, B. G. (1977) "Mean flow measurements in turbulent boundary layers along mildly curved surfaces," AIAA Journal, Vol. 15, No. 2, pp. 189-196.

Rao, B. N. S. (1980) "An experimental study of the effects of moderate to strong longitudinal curvature on turbulent boundary layers," Ph.D. Thesis, Dept. of Aeronautical Engineering, Indian Institute of Science, Bangalore.

Rayleigh, J. W. S. (1917) "On the dynamics of revolving fluids," Proceedings of the Royal Society of London, Vol. 93, Serial A, pp. 148-154.

Runstadler, P. W., Kline, S. J., & Reynolds, W. C. (1963) "An experimental investigation of the flow structure of the turbulent boundary layer," Report MD-8, Thermosciences Division, Dept. of Mechanical Engineering, Stanford Univ.

Savill, Anthony Mark (1979) "Effects on turbulence of curved or distorting mean flow," Ph.D. Thesis, Selwyn College, Univ. of Cambridge.

Schraub, F. A., Kline, S. J., Henry, J., Runstadler, P. W., & Littell, A. (1965) "Use of hydrogen bubbles for quantitative determination of time dependent velocity fields in low-speed water flows," J. Basic Engineering, Trans. ASME, Series D, pp. 429-444.

Shizawa, T., Honami, S., Shirai, H., & Takahashi, A. (1981) "The effect of longitudinal vortices in a turbulent boundary layer over a concave wall," Private communication from S. Honami.

Simon, T. W., Moffat, R. J., & Kays, W. M. (1980) "Turbulent boundary layer heat transfer experiments: convex curvature effects, including introduction and recovery," Report HMT-32, Thermosciences Division, Dept. of Mechanical Engineering, Stanford Univ.

Smits, A. J., Young, S. T. B., & Bradshaw, P. (1979) "The effects of short regions of high surface curvature on turbulent boundary layers," J. Fluid Mech., Vol. 94, Pt. 2, pp. 209-242.

So, Ronald M. C. & Mellor, George L. (1975) "Experiment on turbulent boundary layers on a concave wall," Aero. Quarterly, Vol. 26, pp. 35-40.

Tan-atichat, J., Nagib, H. M., & Loehrke, R. I. (1982) "Interaction of free stream turbulence with screens and perforated plates: A balance between turbulence scales," J. Fluid Mech., Vol. 114, part 3, pp. 541-568.

Tani, Itiro (1962) "Production of longitudinal vortices in the boundary layer along a concave wall," J. Geophysical Research, Vol. 67, No. 8, pp. 3075-3080.

Thompson, D. H. (1973) "Flow visualization using the hydrogen bubble technique," Dept. of Supply, Australian Defense Scientific Service, Aeronautical research Labs, Melbourne, Aerodynamics Note 338, NTIS N73-30229.

Wattendorf, Frank L. (1935) "A study of the effect of curvature on fully developed turbulent flow," Proc. Royal Soc., Vol. 148, pp. 565-598.

White, Frank M. (1974) Viscous Fluid Flow. McGraw-Hill Book Co. Appendix C, pp. 674-678.

Wilcken, H. (1930) "Effect of curved surfaces on turbulent boundary layers." NASA TT-F-11, 421. Translation of "Turbulente Grenzschichten an gewoelbten Flaechen," Kaiser Wilhelm Inst. for Flow Research, Vol. 1, No. 4, pp. 357-376.

Appendix A

WATER CHANNEL DESIGN

A.1   OUTER CHANNEL DESIGN

The basic design criteria for the outer channel structure were:

1. that it safely hold the large volumes of water required,

2. that it be as large as practically and economically possible,

3. that it permit visual access to as much of the test wall as possible, and

4. that it be flexible enough in design to allow for future modifications or repairs.

The last criterion and the desire to facilitate the construction led to a modular approach where the channel could be assembled from parts of an easily manageable size. Consequently, the fabrication of the parts could be done elsewhere and the channel assembled on site with little or no additional modification to the parts.

Visualization requirements dictated that most of the channel be transparent. To support the weight and pressure of the large volumes of water, a steel reinforcing frame was necessary. In order to facilitate fabrication, the channels and frames were designed as separate units.

- 98 -
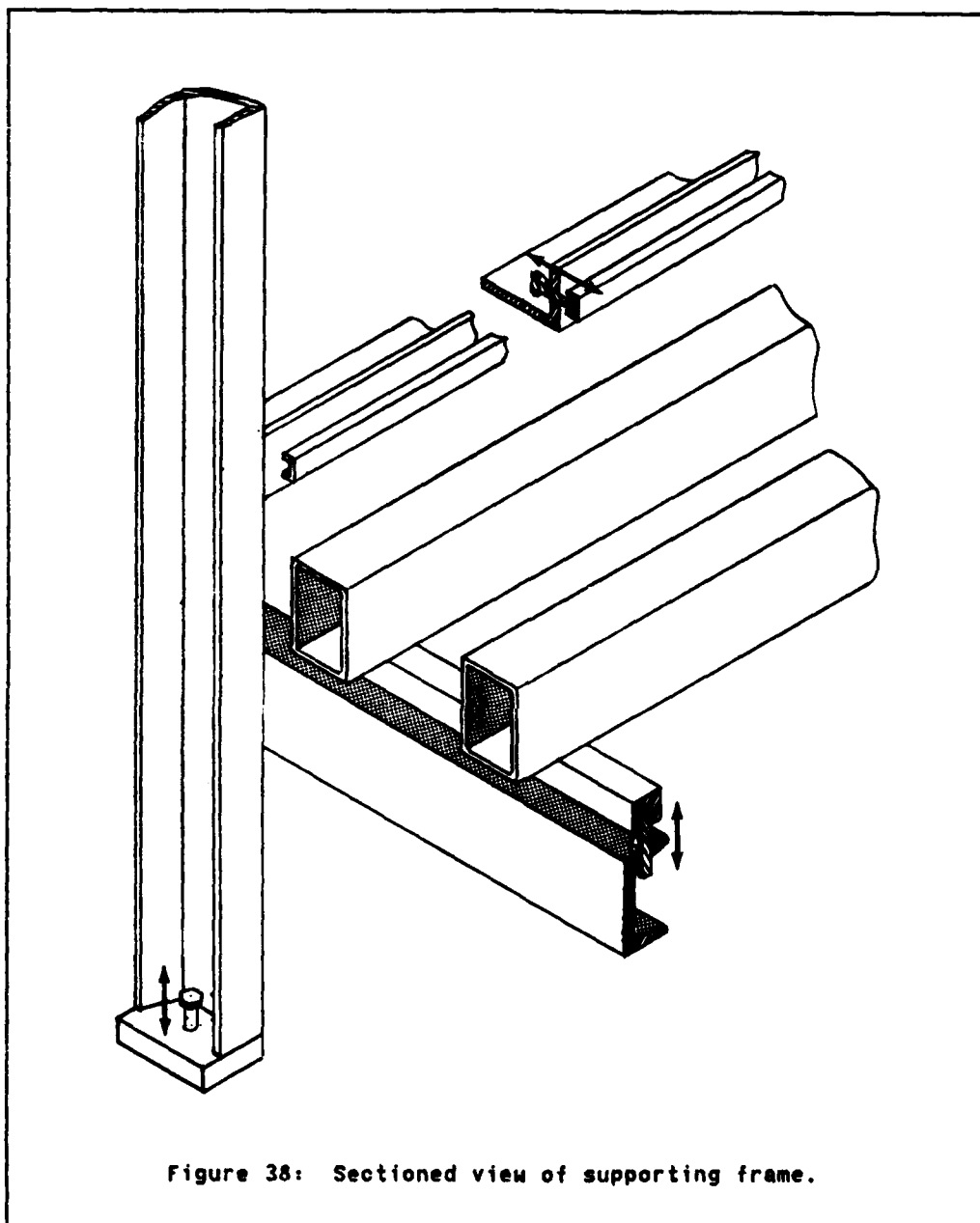
Figure 38:   Sectioned view of supporting frame.

Adjustable braces (see arrows) were used to fit each frame to its chan-

nel, as shown in Fig. 38. In addition, this design feature increased the

modularity of the apparatus. We chose plexiglas over glass for the channels because of the relative ease with which it can be machined and joined. This was considered more important than the scratch resistance of the material. The standard 4'x8' sheets plexiglas comes in, led to a channel module size of 4' long, 4' high, and 2' wide. The size and weight of these modules permitted easy handling by two people without using power equipment.

Each channel module had flanges at either end which were used to bolt adjacent channels to each other. A soft neoprene rod, sandwiched between flange faces and held in place by a groove in one face, sealed each joint. Design data for the groove was obtained from O-ring manuals, but the best bolt spacing was ultimately determined by constructing a small, prototype flange.

The inlet and outlet plenums were fabricated out of sheet steel reinforced with channel bar (small section channel) because we did not expect to have to visualize the flow in these parts. A special neoprene-asphalt paint was painted on the inside surfaces to prevent rusting. This paint has the advantages of being very flexible and easy to apply. In addition it possesses outstanding corrosion resistance properties. The plenum exteriors and the frames were painted with an industrial grade waterproof epoxy paint.

The joints between the channels and the plenums were fabricated on site since it was difficult within cost constraints to construct flanges of sufficient flatness on the plenums. At first, closed cell neoprene foam rubber was used to bridge the gap between the plexiglas and the

steel, but this material was found to shrink considerably when exposed
to our water supply, due perhaps to the high chlorine levels. Finally,
solid neoprene sheet was employed with better success. Contact cement
was used to bond the neoprene to the plexiglas and steel, followed by
silicone rubber caulk to make the joints water tight.

The stress/strain calculations needed to specify the sizes of the
various members of the frames and channels were done by breaking the
structures into their individual components and applying two-dimensional
strength of materials formulae for beam deflections, assuming that each
member was independent of the rest. In most cases the results were con-
servative estimates of the deflection to be expected. Most of the beams
were sized to keep deflections under 0.050". In the actual structures,
three-dimensionality would make the structures stronger and the deflec-
tions less. Beam sections (i.e. angle, channel, or I-beam) were selected
to minimize weight and cost and to simplify the design and fabrication
of the beam joints.

The size and/or quantity of the parts made fabrication of most of
them in our own shop unfeasible so vendors were contracted to do the
initial construction. The steel frames were assembled by Bill Arbogast
of Precision Welding, Mountain View, who also painted the parts. The
outer channel walls were fabricated by Star Products in Sunnyvale, while
the inner channel walls (described in more detail below) were con-
structed by the Hughes Plastic Co. in Redwood City. We received good,
friendly service from these vendors and recommend them to future rig
builders.

The costs of the various parts were roughly $13,000 for the steel frames and plenums, $12,000 for the outer channel walls, and $5,000 for the inner channel walls.

A.2 DESIGN AND SPECIFICATIONS OF FLOW CONTROL ELEMENTS

The various flow control elements in the water channel were sized assuming a nominal flow speed of 0.5 ft/sec through the test section, whose cross-sectional area was assumed to be 3 to 4 ft². However, the pump obtained is capable of delivering 1200 gal/min. We were unable to find much literature with design information (mainly pressure drop coefficients) for low-speed flows such as ours. However Miller's Internal Flow Systems[11] served as an excellent guide to design considerations for higher speed flows, and we were able to extrapolate from those figures and obtain reasonable guesses for our system. The reader should refer back to Fig. 5 for a diagram of the channel and its flow control elements.

A.2.1 Safety Overflow

The overflow in the inlet plenum was designed to help regulate the water level in the channel as well as serve as a safety feature to prevent the water from overflowing the channel walls should something obstruct the flow downstream. We required that the overflow pipe pass at least a quarter of the maximum flow of 1200 gal/min. A 4″ diameter pipe with a 4′ vertical drop, capable of passing about 600 gal/min, was considered adequate.

----

[11] Miller, Donald S. (1968) Internal Flow Systems, Vol. 5 in the British Hydromechanics Research Assoc. Fluid Engineering Series.

A.2.2 Perforated Pipe

In order to reduce the effects of pump surging and to break up the large eddies generated by the valves and elbows in the delivery piping, we forced the flow to pass through a perforated pipe with a large pressure drop across its surface. The pipe was simply a vertical, detachable extension of the delivery pipe coming through the bottom of the inlet plenum. Although some simple calculations using Bernoulli's equation provided a rough estimate of the porosity of the pipe required for, say, a head loss of one foot of water, the final design was determined by trial. The final design incorporates 9 columns of 0.5" diameter holes placed on the side of the pipe facing upstream. Future workers may wish to increase the number of holes to increase the channel's flowrate, since this pressure drop is a major resistance in the flow system.

A.2.3 Perforated Plate

The requirement for the perforated plate was that it cause a loss of about 100 velocity heads and have a porosity less than 20% to prevent jet coalescing. For plate porosities on the order of 10%, such pressure drops occur for a wide range of pitch Reynolds numbers (Reynolds numbers based on the mean velocity upstream of the plate and the distance between holes). The final design, influenced to some extent by the availability of stainless steel perforated plates, uses 3/16" diameter holes spaced 0.5" apart in a hexagonal pattern, with an open area of 13%. The plate was punched for us by the Duus Perforating Co. in San Jose.

A.2.4 Honeycomb

Pressure losses across honeycomb flow straighteners are usually neglige-
able. We selected a honeycomb panel (Hexcel HRP glass-reinforced phe-
nolic) 3″ thick with 1/4″ cells. The cell diameter Reynolds number is
then about 300.

A.2.5 Screens

The screens were selected to have the lowest possible wire diameter Rey-
nolds number and an open area of at least 60%. Stainless steel wire
cloths available from Tyler Industrial Products, Hayward, a large sup-
plier of industrial wire cloths and screens, use wires with diameters as
small as 0.004″. Using wire of this size in a screen with 60% open area
(56 mesh) at the nominal flowrate, the wire diameter Reynolds number is
less than 10. We estimated the pressure loss across each screen to be
about 3 velocity heads or about 0.015″. The screens were mounted in
plexiglas frames in a manner much like conventional window screens. A
flexible rubber rod was squeezed into a groove along with the screen,
holding it in place. We were able to pre-tension the frames so that the
screens remained fairly flat and taut when placed in the flow.

A.2.6 Nozzle

Following the advice of Bradshaw & Pankhurst[12] we shaped our nozzle
using cubic splines. The geometrical requirements for the nozzle are
shown in Fig. 39, where the solid lines represent the walls of the

----

[12] Bradshaw, P. & Pankhurst, R. C. (1964) "The design of low-speed wind
tunnels," Progress in Aeronautical Sciences, Vol. 5, Pergamon Press,
pp. 1-69.

Figure 39: Nozzle placement.
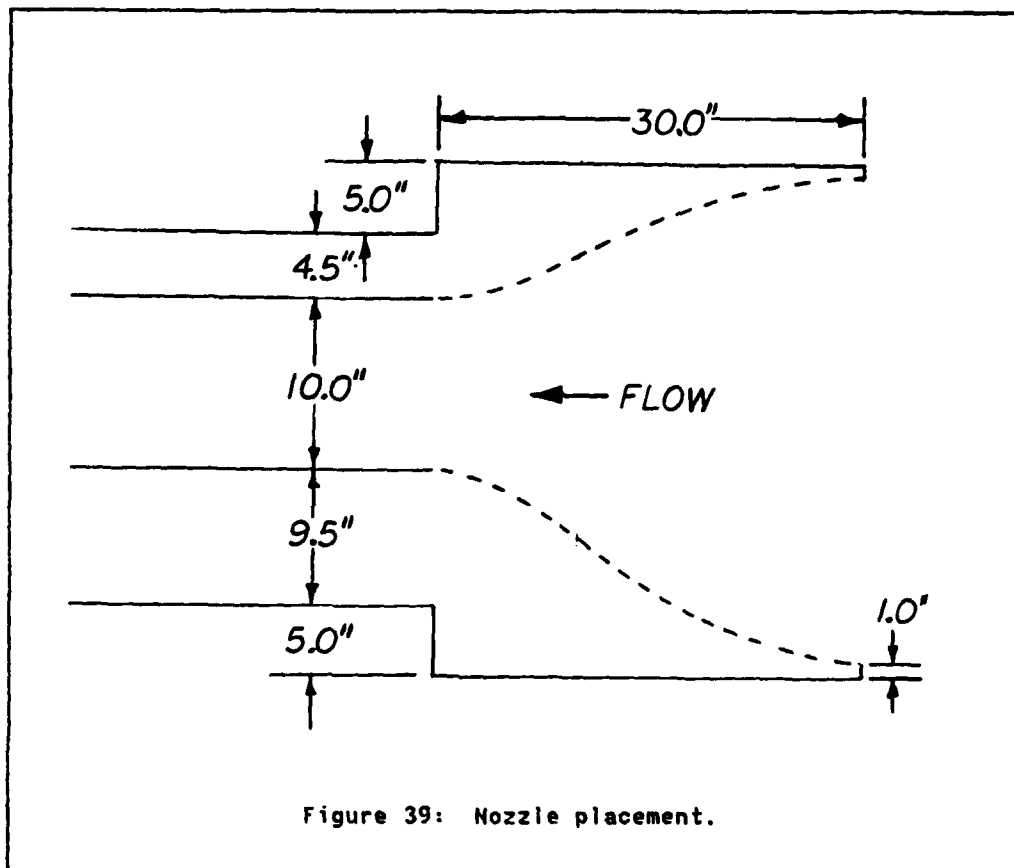
plenum, outer channel, and test walls, and the dotted lines represent the approximate shape of the nozzle to be designed. Because of the desire to allow more space between the test wall and the outer channel, the nozzle had to be asymetrical.

The matching point for each pair of cubic arcs was chosen to lie on the line joining the two endpoints, about 2/3 of the distance downstream of the inlet (refer to Fig. 40). Instead of performing two calculations, one for a width of 8.5″ and another for a width of 13.5″, one calculation was done for a width of 11.0″ and the results scaled accordingly. The 8 constants in the two cubic arcs:

Figure 40: Geometry of partial problem.
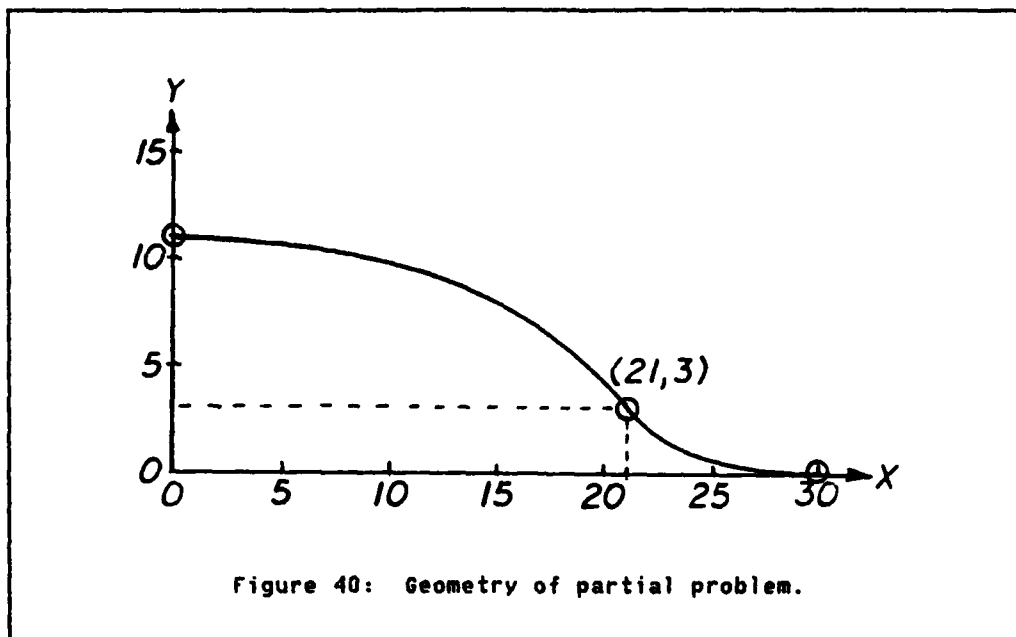
$$y_i = a_i + b_i x + c_i x^2 + d_i x^3, \quad i=1,2 \qquad\qquad (A.1)$$

were deterimined by imposing the following boundary conditions:

1. The ends of the arcs must be fixed at their proper locations:

$$y_1(0)=11, \ y_1(21)=y_2(21)=3, \ y_2(30)=0 \qquad\qquad (A.2)$$

2. The first derivatives must vanish at the inlet and outlet points:

$$\frac{dy_1}{dx}(0)=\frac{dy_2}{dx}(30)=0 \qquad\qquad (A.3)$$

3. The slopes must match at the matching point:

$$\frac{dy_1}{dx}(21)=\frac{dy_2}{dx}(21)=m \qquad\qquad (A.4)$$

4. The second derivative at the outlet must vanish:

- 106 -

$$\frac{dy_2{}^2}{dx^2}(30)=0 \qquad\qquad\qquad\qquad (A.5)$$

The solution to the above equations and boundary conditions is:

$$y=\begin{cases} 11.00 - 6.800\times10^{-3}x^2 - 5.396\times10^{-4}x^3 & (0\leq x\leq 21) \\ 111.1 + 11.11x + 0.3703x^2 - 4.118\times10^{-3}x^3 & (21\leq x\leq 30) \end{cases} \qquad (A.6)$$

The y-values from these equations were multiplied by 8.5/11 and 13.5/11 to obtain the final nozzle configuration.

A.2.7   Drain Valve

The initial design of the channel incorporated an adjustable weir at the end of the channel to regulate the level of the water and its flowrate. However, the resulting waterfall entrained unacceptably large amounts of air and this design was scrapped when we wanted to start using hot film probes and hydrogen bubbles. The problem was to regulate the flow going back into the sump without entraining any air.   There was no room to place conventional valves in the piping that was above floor level, and valves placed in the sump would be difficult to get to. We tried using homemade disc valves which were controlled by cables running back out of the plenum, but the hydrodynamic forces were too large to make fine adjustments possible. Finally a special valve, shown in Fig. 41, was designed and fabricated . Once the channel was filled, the depth of the water in the plenum prevented strong vortices from forming and any air remaining in the pipe below the valve was quickly entrained and removed by the flow.   Although the valve had a tendency to vibrate some, it was rugged enough to withstand the large hydrodynamic forces and performed satisfactorily.

Threaded

Figure 41: Drain valve in outlet plenum.
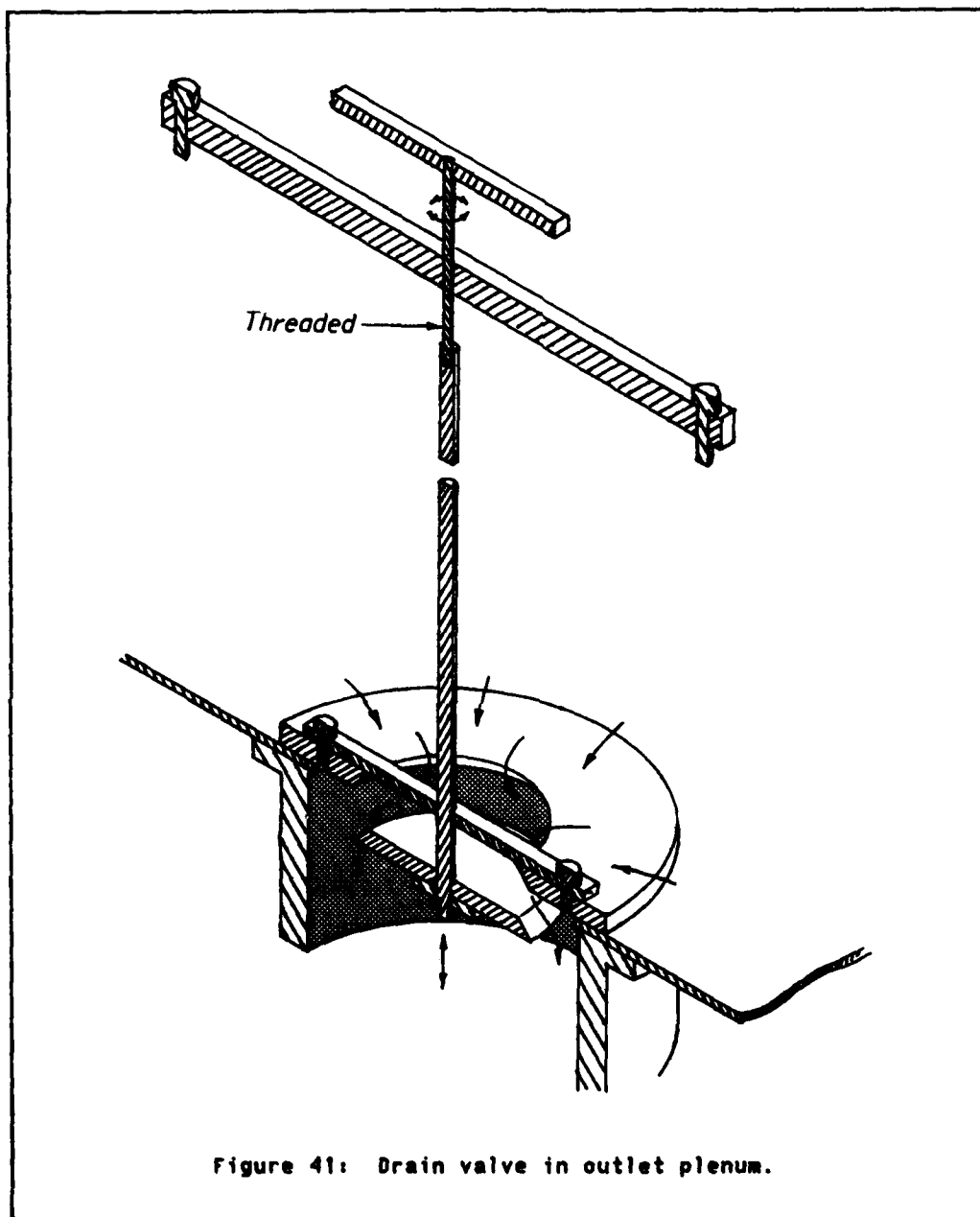
A.3   INNER CHANNEL DESIGN

In order to minimize the effects of the streamwise pressure gradient on the turbulent structure at the test wall, a design calculation was performed to determine the geometry of the opposite wall. First the potential flow velocities at the two walls (test wall with concave surface and opposite, flow control wall) were computed for a variety of opposite wall geometries.   The potential wall velocities were then used in a flat-wall boundary layer calculation to compute the streamwise development of the displacement thicknesses on both walls. The sum of the displacement thicknesses at each streamwise location was then added to the local channel width to determine the shape of the opposite wall. A more detailed description follows.

The geometry of the inner walls was to a large extent determined by the size constraints imposed by the outer structure, which in turn was made as large as economically and practically feasible.   The radius of the test wall was made to fit the corner module with a minimum clearance between the inner and outer wall of about 9" for access to the dye slots or other devices.   The opposite wall was then initially placed so that there was a clearance of about 4" between it and the outer wall. This then determined the inlet geometry and a nozzle was designed to carry the flow from the settling chamber to the channel.

In order to calculate the potential flow through the channel, a fast Laplace solver developed by Wooley, White, Bardina, & Kline[13] was used

----

[13] A description of the program may be found in "A Boundary Method for Potential Flows" by Juan G. Bardina, Report IL-17, Thermosciences Div., Dept. of Mechanical Engineering, Stanford Univ., 1977.

which determines the tangential velocities at specified points along the boundaries given the normal velocities. The program, PHIVN, calls on several large library subroutines and is not listed here. In this case the coordinates of points describing the channel geometry were entered in a counterclockwise fashion along with the normal velocity at the middle of the next segment. This normal velocity was zero for all points except two at the inlet and outlet. The initial geometry was a 90° annular sector, outer radius 136 cm (53.6"), width 24.1 cm (9.5"), with straight lead-in and trailing sections. Because of the symmetry of the channel, only half of the coordinates had to be entered; the rest were generated by the computer. The coordinates were stored in separate files for the inner and outer walls. Small auxiliary programs combined the files to create an input for PHIVN. By running PHIVN and gradually adjusting the shape of the flow control wall, the velocity along the entire test wall was made uniform to within 3% of the mean. Finer adjustments were not undertaken because it was known that the walls could not be manufactured to closer tolerances. The final potential flow geometry is described by the coordinates in Table 4. Note that X and Y refer to standard, cartesian coordinates. Fig. 42 shows these points plotted along with a circular arc, which is shown by the dashed line. Fig. 43 graphs the computed wall velocities corresponding to this channel geometry.

The output of PHIVN was then modified by another small program to serve as the input to a flatplate boundary layer code. The data for each wall was isolated, converted into the form of streamwise displacement versus velocity, and appended to additional points needed to make up the

TABLE 4

Channel configuration, cartesian coordinates.

Concave (test) wall

X, cm	Y, cm	X, cm	Y, cm
-0.1219E+03	-0.1361E+03	0.1128E+03	-0.7620E+02
-0.1524E+02	-0.1361E+03	0.1217E+03	-0.6096E+02
-0.1016E+02	-0.1361E+03	0.1282E+03	-0.4572E+02
-0.5080E+01	-0.1361E+03	0.1321E+03	-0.3302E+02
0.0000E+00	-0.1361E+03	0.1338E+03	-0.2540E+02
0.5080E+01	-0.1360E+03	0.1346E+03	-0.2032E+02
0.1016E+02	-0.1358E+03	0.1353E+03	-0.1524E+02
0.1524E+02	-0.1353E+03	0.1358E+03	-0.1016E+02
0.2032E+02	-0.1346E+03	0.1360E+03	-0.5080E+01
0.2540E+02	-0.1338E+03	0.1361E+03	0.0000E+00
0.3302E+02	-0.1321E+03	0.1361E+03	0.5080E+01
0.4572E+02	-0.1282E+03	0.1361E+03	0.1016E+02
0.6096E+02	-0.1217E+03	0.1361E+03	0.1524E+02
0.7620E+02	-0.1128E+03	0.1361E+03	0.1219E+03
0.9627E+02	-0.9627E+02		

Convex (control) wall

X, cm	Y, cm	X, cm	Y, cm
0.1120E+03	0.1219E+03	0.7112E+02	-0.8915E+02
0.1120E+03	0.1524E+02	0.6096E+02	-0.9639E+02
0.1121E+03	0.1270E+02	0.4826E+02	-0.1033E+03
0.1121E+03	0.1016E+02	0.3810E+02	-0.1075E+03
0.1122E+03	0.7620E+01	0.3175E+02	-0.1092E+03
0.1124E+03	0.5080E+01	0.2540E+02	-0.1112E+03
0.1125E+03	0.2540E+01	0.2032E+02	-0.1122E+03
0.1127E+03	0.0000E+00	0.1778E+02	-0.1126E+03
0.1130E+03	-0.2540E+01	0.1524E+02	-0.1130E+03
0.1132E+03	-0.5080E+01	0.1270E+02	-0.1133E+03
0.1133E+03	-0.7620E+01	0.1016E+02	-0.1133E+03
0.1133E+03	-0.1016E+02	0.7620E+01	-0.1133E+03
0.1133E+03	-0.1270E+02	0.5080E+01	-0.1132E+03
0.1130E+03	-0.1524E+02	0.2540E+01	-0.1130E+03
0.1126E+03	-0.1778E+02	0.0000E+00	-0.1127E+03
0.1122E+03	-0.2032E+02	-0.2540E+01	-0.1125E+03
0.1112E+03	-0.2540E+02	-0.5080E+01	-0.1124E+03
0.1092E+03	-0.3175E+02	-0.7620E+01	-0.1122E+03
0.1075E+03	-0.3810E+02	-0.1016E+02	-0.1121E+03
0.1033E+03	-0.4826E+02	-0.1270E+02	-0.1121E+03
0.9639E+02	-0.6096E+02	-0.1524E+02	-0.1120E+03
0.8915E+02	-0.7112E+02	-0.1219E+03	-0.1120E+03
0.8064E+02	-0.8064E+02		

Figure 42:   Curved channel geometry.
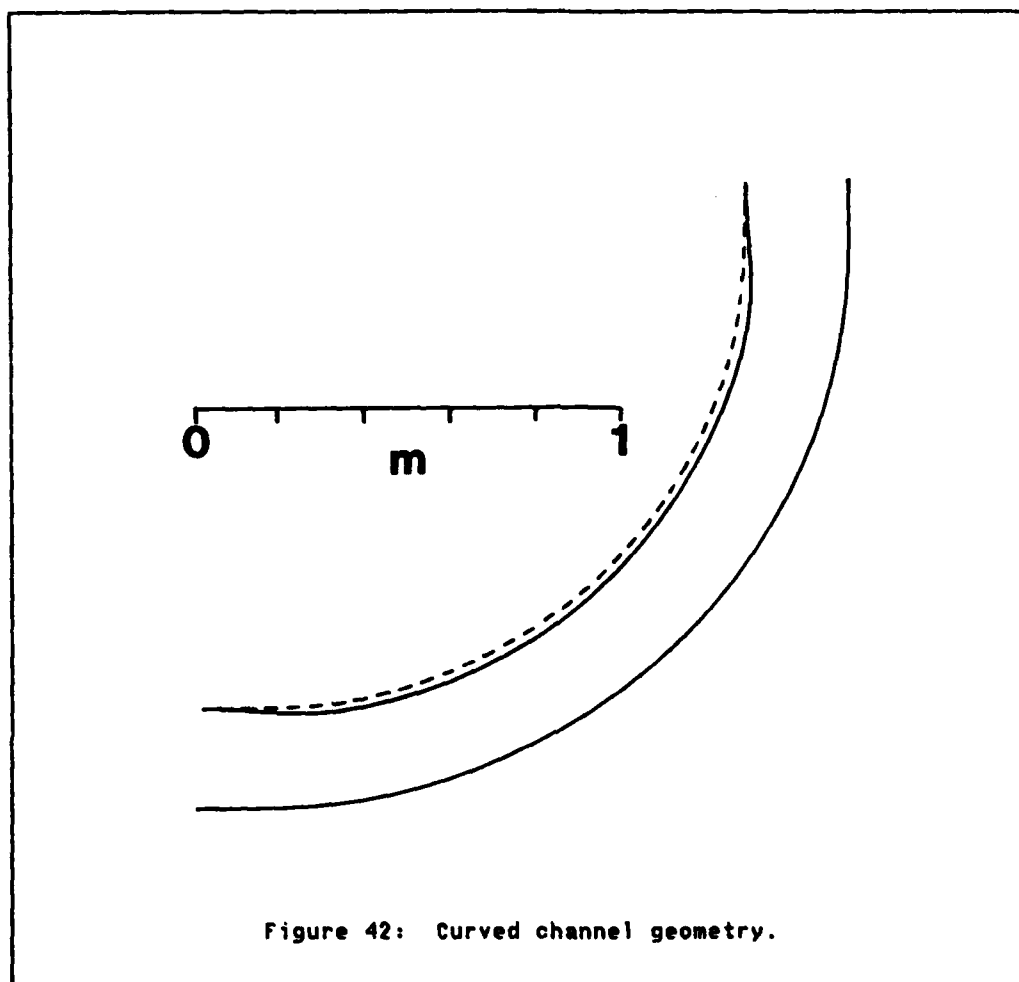
entire wall.   A code written by Cebeci & Bradshaw[14] used the velocity

data to compute boundary layer parameters. The resulting displacement

thicknesses are shown in Fig. 44. For the case of the variable width

channel, separation occurs when the flow is expanded downstream of the

bend. The sum of the displacement thicknesses for the two walls at a

----

[14] Cebeci, Tuncer & Bradshaw, Peter (1977) Momentum Transfer in Boundary
   Layers. Hemisphere Publishing Corp. & McGraw-Hill Book Co. pp.
   258-269.

POTENTIAL WALL VELOCITIES

CONCAVE WALL

* CONSTANT WIDTH
○ VARIABLE WIDTH

POTENTIAL WALL VELOCITIES

CONVEX WALL

* CONSTANT WIDTH
○ VARIABLE WIDTH
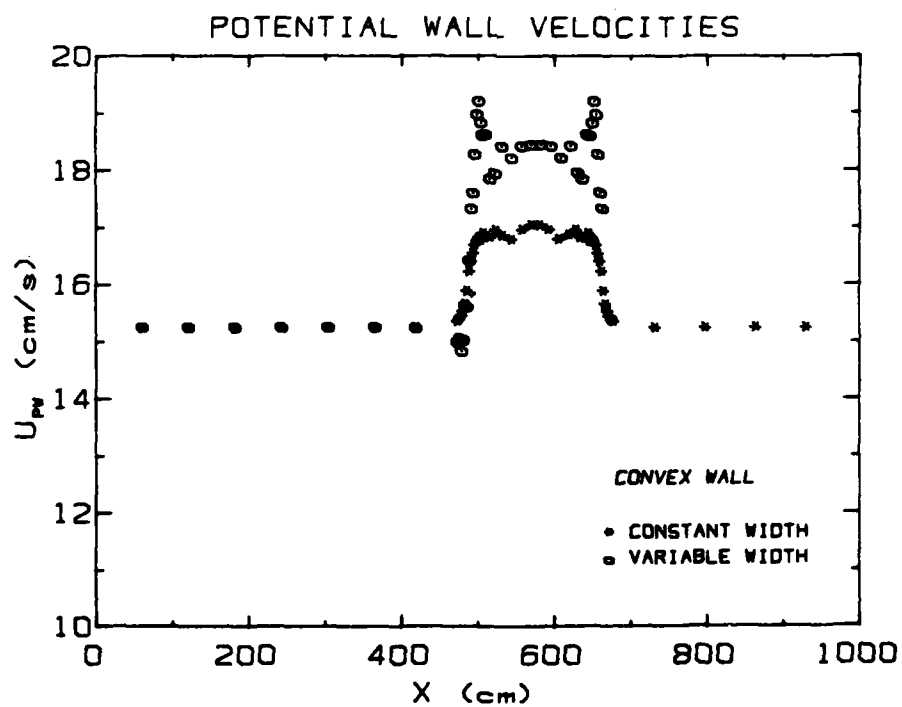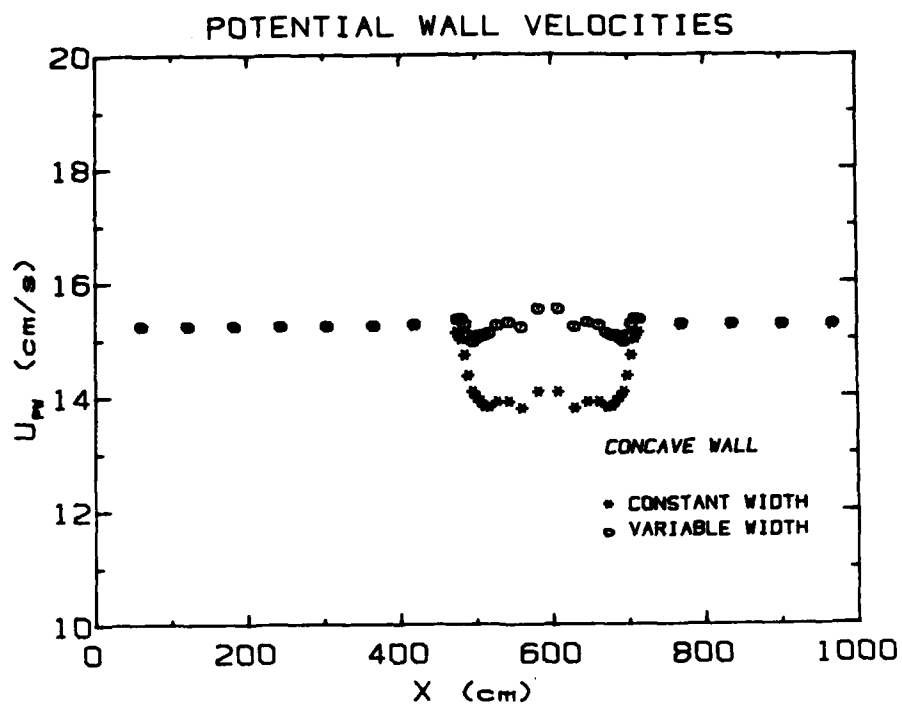
Figure 43: Computed potential wall velocities, constant and variable
width channels.

CALC. DISPLACEMENT THICKNESS

CALC. DISPLACEMENT THICKNESS
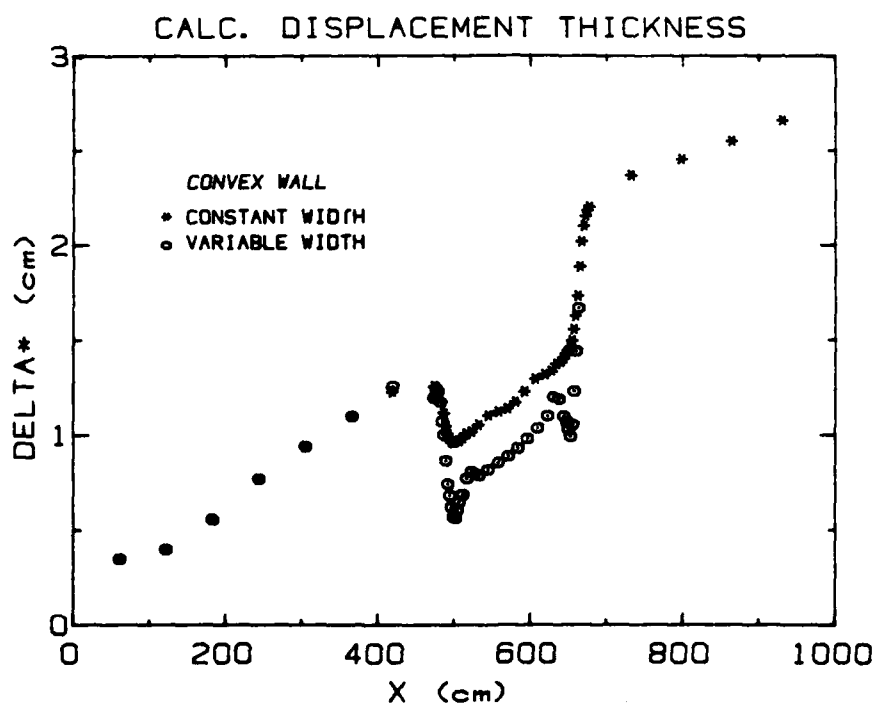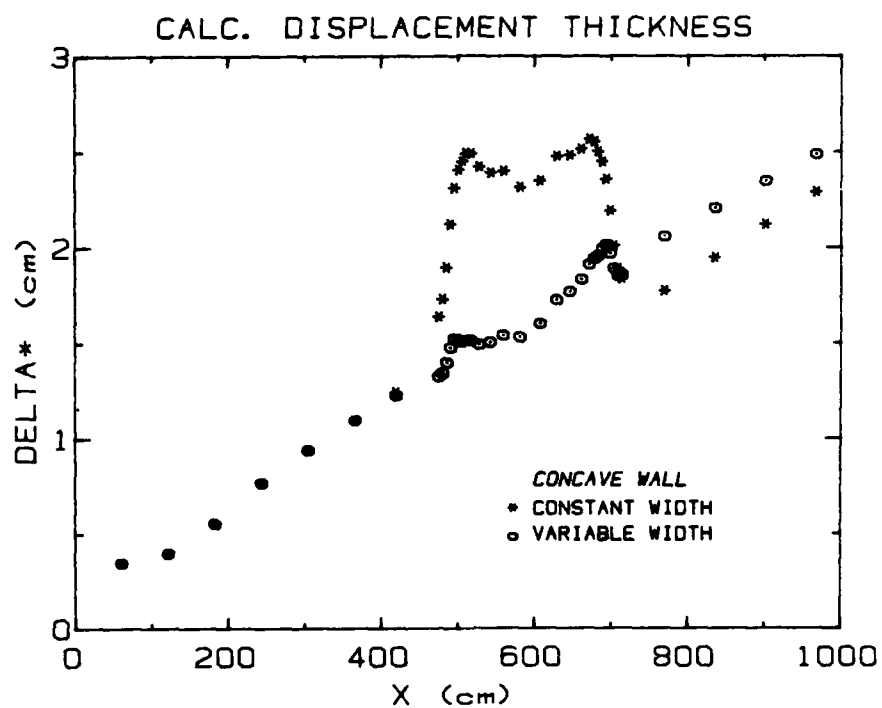
Figure 44: Computed displacement thicknesses for constant and variable width channels.

given x, or angle (in the bend), was then added to the width of the channel to obtain the final opposite wall geometry. This correction was at most about 5% of the channel width. The channel width including the displacement thickness correction is tabulated in Table 5. For the part of the channel downstream of the calculated separation point, no additional corrections were made.

TABLE 5

Channel width as a function of streamwise distance.

x, cm	w, cm	x, cm	w, cm
122	24.92	533	24.54
244	25.66	559	24.67
366	26.32	584	24.68
419	26.61	610	24.82
490	25.52	635	25.32
508	24.21	660	25.36

Admittedly, a flatplate code was used for curved flow; however, we felt that for a first approximation, the results would greatly reduce the streamwise pressure gradient on the test wall and would certainly be an improvement over no corrections at all.

The finished walls were anchored to the channel bottom by adjustable brass braces and to the top of the channel frame by threaded rods as shown in Fig. 45. This mounting system enabled us to position the walls very accurately. The various sections were attached to each other by screws.

(a)

(b)

Figure 45: Mounting devices at the (a) top and (b) bottom of the inner walls.

Appendix B

TRAVERSE DESIGN

B.1 HARDWARE

In order to accurately position probes within the channel a two-axis traverse had to be designed which could move probes about in the channel cross-plane (y-z). The large size of the rig and the potential availability of a computer led to a design incorporating digitally controlled stepper motors. The motors chosen for the job were capable of rotating their shafts in 0.9^{o} increments with an accuracy of $\pm 5\%$. Since positioning on the horizontal (y) axis had to be more accurate than on the vertical (z) axis, a lead-screw was used on the former and a rack and pinion on the latter. The wide range of gearing available made it possible to convert the rotation of the motor shafts into precise metric steps while still using American Standard gears, screw threads, etc. In the final design, 20 full (1.8^{o}) steps of the horizontal motor caused the traverse to move 0.1 mm with an error of 0.05%, and 4 steps of the vertical motor resulted in a 1.0 mm vertical displacement with an error of 0.25%. The parts specifications are shown in Table 6. Initially, the vertical portion of the traverse rode directly on the lead-screw. However, eccentricity of the screw threads and the shaft ends resulted in objectionable oscillations of the vertical axis, so linear bearings were added to take the vertical load off of the lead-screw. A close-up photo of the traverse appears in Fig. 46.

```
                         TABLE 6

                 Traverse Parts Specifications.


Horizontal Axis:
Gear     Teeth   Pitch    Tooth Angle   Pitch Dia.
drive    17      24         14.5°         0.708"
driven   27      24         14.5°         1.125"


Center distance=0.917".


Lead screw thread: 3/8-16 stainless steel (specially rolled).


Vertical Axis:
Gear     Teeth   Pitch    Tooth Angle   Pitch Dia.
pinion   20      32         14.5°         0.625"
rack     --      32         14.5°         ---
```

B.2 MOTOR CONTROLS

In order for a stepper motor to turn, its 4 leads must be energized in a
particular sequence. To do this manually would be tedious indeed, so
various electronic controllers are available to simplify the task.
Because we wanted to be able to position the probe without necessarily
relying on a computer, we purchased what are known as preset indexer
modules (PIM's). These devices send out the sequence of pulses necessary
to move the motor a user-specified number of steps.   The indexers were
available as unmounted pc boards; To save space and money, both indexers
were mounted in a common chassis along with the necessary power supplies
and switches. The various leads controlling the number of steps, the
initiation of a move, etc., while being wired internally to the switches
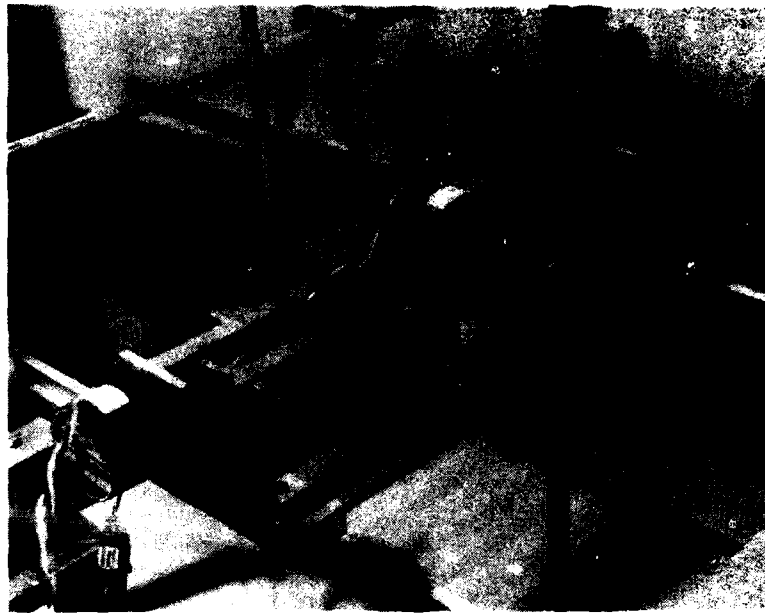
Figure 46: Two-axis traverse.

on the front panel, were also made accessible through multi-pin connec-
tors on the back panel for optional computer control.

B.3 COMPUTER CONTROLS

Shortly after the motor controller was built, we were able to obtain a
DEC MINC-11 microcomputer for our use. To enable the computer to control
the motors, an interface was needed between the indexers and the MINC.
In order to understand the workings of the interface, one must know
something about the requirements of the PIM's and the MINC.

Figure 47: Timing diagram for Preset Indexer Module.
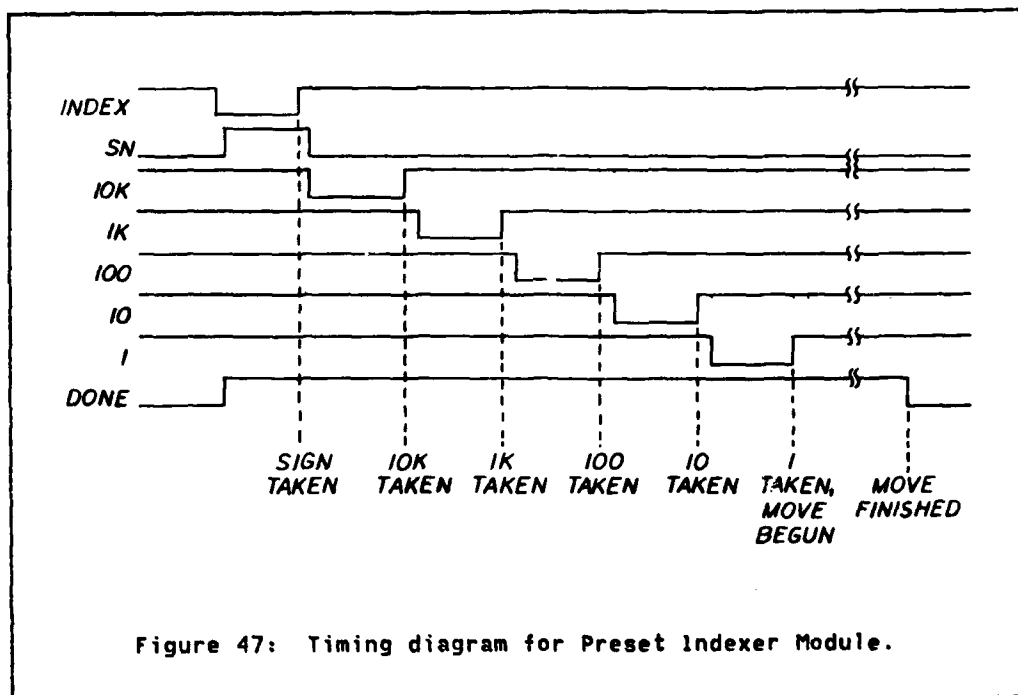
The PIM's require inputs to determine 5 decimal digits and a sign (for the number of steps and the direction of motion), and an input to start the indexed move. The PIM's provide a "done" signal on another line. Each digit is represented in binary coded decimal by the states of 4 leads (8-4-2-1). Rather than use 4 leads for each digit, all the digits use the same BCD lines (the sign uses line 8) and 6 other control (COM) lines determine the place of the digit (1's, 10's, etc. and the sign). All lines are active low except the sign (SN) line which is active high. A PIM operates in the following fashion: The user signals the PIM by pulling the INDEX line low. This causes the SN and DONE lines to go high (see timing diagram in Fig. 47). When the INDEX line is allowed to go high again, the PIM samples the 8 line for the sign. A

short time later, the SN line returns to its low state. The PIM then

sequentially strobes each of the 5 other COM lines and samples the BCD

lines on the rising edge of the COM signal to determine each digit.

After the last digit is acquired, the PIM starts the motor and causes it

to turn the required number of steps. When the move is completed the

DONE line is pulled low again.

The MINC Digital Out unit allows the user to output 16 bits under

computer control. In addition, two lines are available which signal when

the 16 bits are available on the lines, and a reply line is available to

signal the computer. The design problem facing me was to use these lines

to send the number of steps to the PIM's and initiate a move.

It was clear that somehow the BCD values for each digit would have to

be made available to the PIM's on demand. This could be done either by

having the MINC respond to each of the COM signals with the correct val-

ues or by having these values stored in an auxiliary memory addressed by

the COM lines. Because the PIM's strobed the COM lines at a fixed rate

with no dependence on any sort of reply line, it was better to use an

auxiliary random access memory (RAM) to minimize the possibility of tim-

ing problems. The MINC could then write data into the RAM at any rate,

and the PIM's could read the data at their own rate.

A block diagram and schematic of the final interface circuit are

shown in Figs. 48 and 49. The MINC writes the 4 bits of data for each of

the 6 digits into RAM locations addressed by 4 of the lines. The MINC

then signals the appropriate PIM using one of two INDEX lines. That PIM

strobes its COM lines, which feed an encoder which produces the address
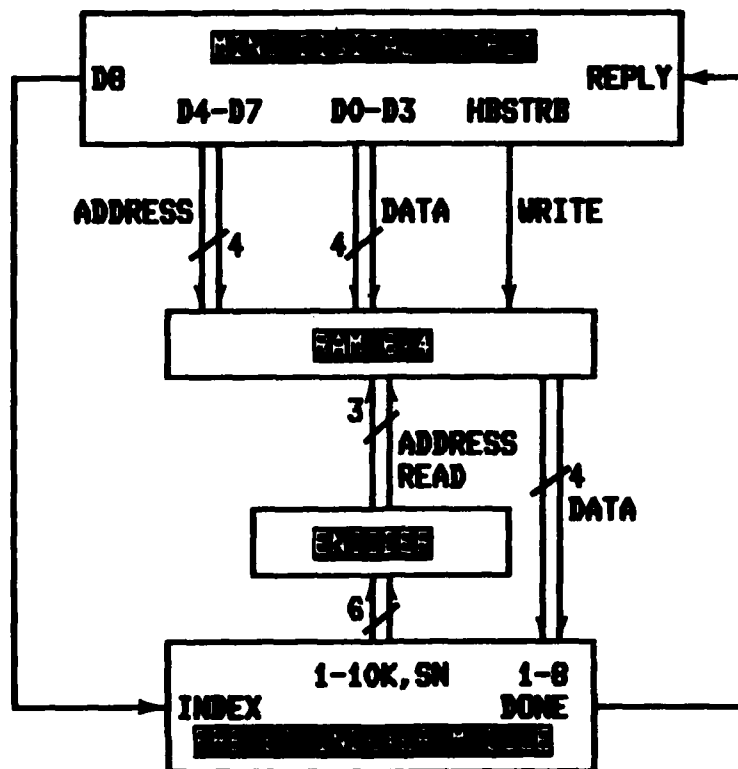
Figure 48: Block diagram of PIM/MINC Interface, only one PIM
            shown.

corresponding to the given COM line. Part of the address places the RAM

in read mode, and the 4 bits addressed appear on the RAM's output lines,

which are connected to the BCD lines of both PIM's. The DONE signal

produced by the PIM's goes back to the MINC, telling the program the

move has been completed. In the actual circuit many of the lines had to

be buffered and the duration of the "data ready" strobe produced by the

MINC lengthened.

Figure 49: Circuit diagram of PIM/MINC Interface.

DATA ACQUISITION PROGRAMS

What follows are the source listings for the BASIC programs written to

calibrate the hot film probe and acquire velocity profiles.

```
10 REM#################################################################
20 REM# Program to calibrate hot films under partial computer control. User
30 REM# must move probe and monitor speed; computer samples anemometer,
40 REM# requests speed, and stores calibration data. Computer s*ops sampling
50 REM# if anemometer output falls below a specified percentage of the mean.
60 REM# If user inputs a speed of zero, that calibration point is discarded.
70 REM# Flow speed is the nominal velocity in the channel during calibration.
80 REM# Results are graphed; clear screen by typing any character.
90 REM#################################################################
100 DIM V(20),U(20)
110 DIM X(1000)
120 PRINT "OUTPUT FILE";
130 LINPUT F$
140 OPEN F$ FOR OUTPUT AS FILE 1
150 PRINT "FLOW SPEED";
160 INPUT U0
170 PRINT "SAMPLING FREQUENCY AND DROPOUT LIMIT";
180 INPUT F,L
190 K=0 \ S1=0
200 PRINT "BEGIN BY TYPING RETURN";
210 LINPUT #0,A$
220 SET_GAIN(,1,8)
230 AIN('CONTINUOUS',X(),F,1/F,8)
240 WAIT_FOR_DATA(X(),I)
250 FOR J=I TO I-1+F/2
260 S1=S1+X(J)
270 K=K+1
280 M=S1/K
290 IF X(J)/M<L GO TO 330
300 NEXT J
310 PRINT USING "##.##",M
320 GO TO 240
330 PRINT "SPEED";
340 TERMINATE('IMMEDIATE',X())
350 INPUT S \ IF S=0 GO TO 190
360 S=S+U0
370 PRINT #1,USING "##.##,##.##",S,M
380 PRINT "ANOTHER SAMPLE";
390 LINPUT A$
```

```
400 IF SEG$(A$,1,1)="Y" GO TO 190
410 PRINT #1,USING "##.##,##.##",0,0
420 CLOSE #1
430 OPEN F$ FOR INPUT AS FILE 2
440 FOR I=1 TO 20
450 INPUT #2,U(I),V(I)
460 IF U(I)=0 GO TO 480
470 NEXT I
480 N=I-1
490 GRAPH("-HLINES",N,U(1),V(1))
500 LINPUT #0,A$
510 DISPLAY_CLEAR
520 END
```

```
10 REM *****************************************************************
20 REM *  Program to take mean and turbulence intensity profiles, to be used
30 REM *  with the DEC MINC-11 with PREAMP, A/D, DIGITAL OUT, and CLOCK LAB
40 REM *  MODULES, along with the specially designed stepper motor control
50 REM *  and interface units. U refers to velocities, V to voltages.
60 REM *****************************************************************
70 DIM L(2),T(1),X(1000)
80 DIM Y(1),U(50),V(50)
90 REM initialize axes indices, step-distance conversion factors, and
100 REM backlash constant.
110 READ Z0,Y0,C1(1),C1(2),B1
120 DATA 1,2,80,-4000,.1
130 L$="##.##, ###.##,  ##.##,  #.###"
140 REM get lists of coordinates for traverse
150 PRINT "Y AND Z COORDINATE FILES";
160 INPUT A$,B$
170 OPEN A$ FOR INPUT AS FILE 1
180 OPEN B$ FOR INPUT AS FILE 2
190 REM get name of output file for data
200 PRINT "OUTPUT FILE";
210 LINPUT A$
220 OPEN A$ FOR OUTPUT AS FILE 4
230 REM initialize probe location
240 PRINT "MOVE PROBE";
250 LINPUT A$
260 IF SEG$(A$,1,1)<>"Y" GO TO 350
270 PRINT "Y,Z COORDINATES";
280 INPUT Y,Z
290 C=Y0 \ P=Y \ GOSUB 3000
300 C=Z0 \ P=Z \ GOSUB 3000
310 PRINT "SET Y ORIGIN";
320 LINPUT A$
330 IF SEG$(A$,1,1)="Y" THEN L(2)=0
340 GO TO 240
350 PRINT "TAKE PROFILE";
360 LINPUT A$
370 IF SEG$(A$,1,1)="Y" GO TO 1000
380 REM termination sequence
390 PRINT "HALT";
400 LINPUT A$
410 IF SEG$(A$,1,1)<>"Y" GO TO 240
420 REM data file terminated with special sequence
430 PRINT #4,USING L$,-1,0,0,0
440 CLOSE #4
450 REM reposition probe at known location
460 C=Y0 \ P=12 \ GOSUB 3000
470 C=Z0 \ P=0 \ GOSUB 3000
480 STOP
1000 REM set-up calibration
1010 GOSUB 6000
1020 REM initialize graphics to display data
1030 WINDOW("EXACT",,,12,16)
1040 GRAPH("-HLINES",1,X(0),Y(0))
1050 F=6
```

```
1060 PRINT "SAMPLING FREQUENCY IS 6 HZ, WHAT IS DURATION";
1070 INPUT T
1080 PRINT ""
1090 PRINT "   Y         Z        U      <U'*U'>"
1100 PRINT "----------------------------"
1110 REM get coordinates to move probe to
1120 INPUT #2,Z
1130 REM coordinate list terminator is -99
1140 IF Z=-99 GO TO 390
1150 INPUT #1,Y
1160 IF Y>-99 GO TO 1200
1170 REM coordinates iterated on Y for each Z
1180 RESTORE #1
1190 GO TO 1120
1200 REM get freestream condition
1210 GOSUB 5000
1220 C=ZO \ P=Z \ GOSUB 3000
1230 C=YO \ P=Y \ GOSUB 3000
1240 REM sample a/d
1250 S1=0 \ S2=0
1260 SET_GAIN(,1,8)
1270 AIN("CONTINUOUS",X(),2*F,1/F,8)
1280 FOR I=1 TO T
1290 WAIT_FOR_DATA(X(),K1)
1300 REM process data
1310 FOR J=K1 TO K1+F-1
1320 X=X(J)*Q
1330 IF X>=V(0) GO TO 1360
1340 PRINT "OUT OF RANGE"
1350 GO TO 1400
1360 FOR K=1 TO N
1370 IF X<=V(K) GO TO 1390
1380 NEXT K
1390 U=U(K-1)+(U(K)-U(K-1))*(X-V(K-1))/(V(K)-V(K-1))
1400 S1=S1+U
1410 S2=S2+U*U
1420 NEXT J
1430 NEXT I
1440 TERMINATE("IMMEDIATE")
1450 REM calculate mean and mean square, type, and plot
1460 M=S1/(F*T)
1470 U2=S2/(F*T)-M*M
1480 PRINT USING L$,Y,Z,M,U2
1490 PRINT #4,USING L$,Y,Z,M,U2
1500 POINT(,Y,M)
1510 GO TO 1150
3000 REM*******************************************************************
3010 REM* Subroutine to move channel C (=Channel#)toP(=Place).
3020 REM*******************************************************************
3030 REM figure out displacement from current location then update position
3040 D=P-L(C)
3050 L(C)=P
3060 S=D*C1(C)
3070 GOSUB 4000
```

- 127 -

```
3080 IF D>=0 THEN RETURN
3090 REM correct for backlash if displacement is negative
3100 S=-B1*C1(C)
3110 GOSUB 4000
3120 S=-S
3130 GOSUB 4000
3140 RETURN
4000 REM*********************************************************************
4010 REM* Subroutine to index channel C, S steps.
4020 REM*********************************************************************
4030 REM set up addresses for step numbers
4040 FOR I=0 TO 7 \ A(I)=10*(I+4) \ NEXT I
4050 D(5)=0
4060 REM decompose number of steps into separate digits and sign
4070 S1=ABS(S)
4080 IF S1<>S THEN D(5)=9
4090 FOR I=4 TO 0 STEP -1
4100 D(I)=INT(S1/10^I)
4110 S1=S1-D(I)*(10^I)
4120 NEXT I
4130 REM add on address bits and convert to binary for output
4140 FOR I=0 TO 5 \ A(I)=A(I)+D(I) \ NEXT I
4150 A(6)=A(6)*C
4160 A(7)=A(6)
4170 FOR I=0 TO 7 \ MAKE_BCD(A(I),A(I)) \ NEXT I
4180 DOUT(,A(),8,.01,)
4190 REM send out dummy argument to start indexing and wait for controller's
4200 REM DONE signal
4210 DOUT(,T(),2,0)
4220 RETURN
5000 REM*********************************************************************
5010 REM* Subroutine to get freestream correction factor.
5020 REM*********************************************************************
5030 REM move probe to freestream conditions
5040 C=Y0 \ P=12 \ GOSUB 3000
5050 C=Z0 \ P=2 \ GOSUB 3000
5060 V1=0
5070 REM get mean bridge output
5080 SET_GAIN(,1,8)
5090 AIN(,X(),20*F,1/F,8)
5100 FOR I=0 TO 20*F-1
5110 V1=V1+X(I)
5120 NEXT I
5130 V1=V1/(20*F)
5140 Q=V0/V1
5150 PRINT USING "V1=#.###",V1
5160 RETURN
5170 REM*********************************************************************
5180 REM* Subroutine to read velocity off calibration curve using X.
5190 REM*********************************************************************
5200 IF X>V(N) GO TO 5270
5210 IF X<V(0) GO TO 5270
5220 FOR K=1 TO N
5230 IF X<=V(K) GO TO 5250
```

```
5240 NEXT K
5250 U=U(K-1)+(U(K)-U(K-1))*(X-V(K-1))/(V(K)-V(K-1))
5260 RETURN
5270 PRINT "OUT OF RANGE"
5280 RETURN
6000 REM*******************************************************
6010 REM* Subroutine to set-up calibration curve.
6020 REM*******************************************************
6030 PRINT "CALIBRATION FILE";
6040 LINPUT A$
6050 OPEN A$ FOR INPUT AS FILE 3
6060 FOR I=0 TO 50
6070 INPUT #3,U(I),V(I)
6080 IF U(I)=0 GO TO 6100
6090 NEXT I
6100 N=I-1
6110 PRINT "VELOCITY AT REFERENCE POINT";
6120 INPUT U0
6130 FOR I=1 TO 50
6140 IF U0<=U(I) GO TO 6160
6150 NEXT I
6160 V0=V(I-1)+(U0-U(I-1))*(V(I)-V(I-1))/(U(I)-U(I-1))
6170 RETURN
9000 END
```

Appendix D

HOT FILM NORMALIZATION PROCEDURE

Nomenclature

d sensor diameter

e bridge voltage

e_m bridge voltage at measurement station

e_n normalized bridge voltage, $e_m \dfrac{e_r}{e_r{}'}$

e_r bridge voltage at reference point

H rate of heat transfer from sensor to fluid

k_{eff} an effective thermal conductivity of the fluid, including the effects of dirt on the sensor

ℓ sensor length

Nu Nusselt number (defined below)

Re Reynolds number (defined below)

R_a sensor resistance at ambient temperature

R_c sensor cold resistance

R_{op} sensor operating resistance

u fluid velocity

u_m fluid velocity at measurement station

u_r fluid velocity at reference point

α temperature coefficient of resistivity of sensor

γ ratio of heat loss due to convection to total heat loss

ν kinematic viscosity of the fluid

θ_a ambient temperature of fluid

θ_c ambient temperature during cold resistance measurement

θ_{op} operating temperature of sensor

$()'$ quantity at some later time

Hot film anemometers have been widely used as an inexpensive means for
acquiring velocity measurements in fluid flows. Because of their dura-
bility, these probes are often used in water, where the relatively low
frequency response of the large-area sensor is not a problem. A common
problem one encounters when using a hot film probe is the drift of the
probe's calibration over time, due to the probe's acute sensitivity to
dirt on its surface and because of changes in the fluid temperature. In
the past, experimenters have sought to overcome these difficulties by
carefully filtering their water and by regulating the water temperature
or employing a temperature compensation probe. With the wide availabil-
ity of laboratory microcomputers, however, another approach is possible.
Here, an alternate method is described which enabled us to obtain
repeatable measurements in a low-speed water flow (u<15 cm/s).

Preliminary measurements showed that no reliable data could be
obtained from the hot film anemometer we were using unless something was
done to account for changes in the probe environment due to dirt and
temperature fluctuations. Fig.   50 shows the anemometer bridge output
over an hour's time with the probe operating at an overheat ratio of
1.08. The change in water temperature over this period was less than
$0.1^\circ C$, so the drift of the probe output is attributed to the accumula-
tion of dirt. The probe was held fixed in a constant velocity, 10 cm/s,

Figure 50: Anemometer output, fixed probe.
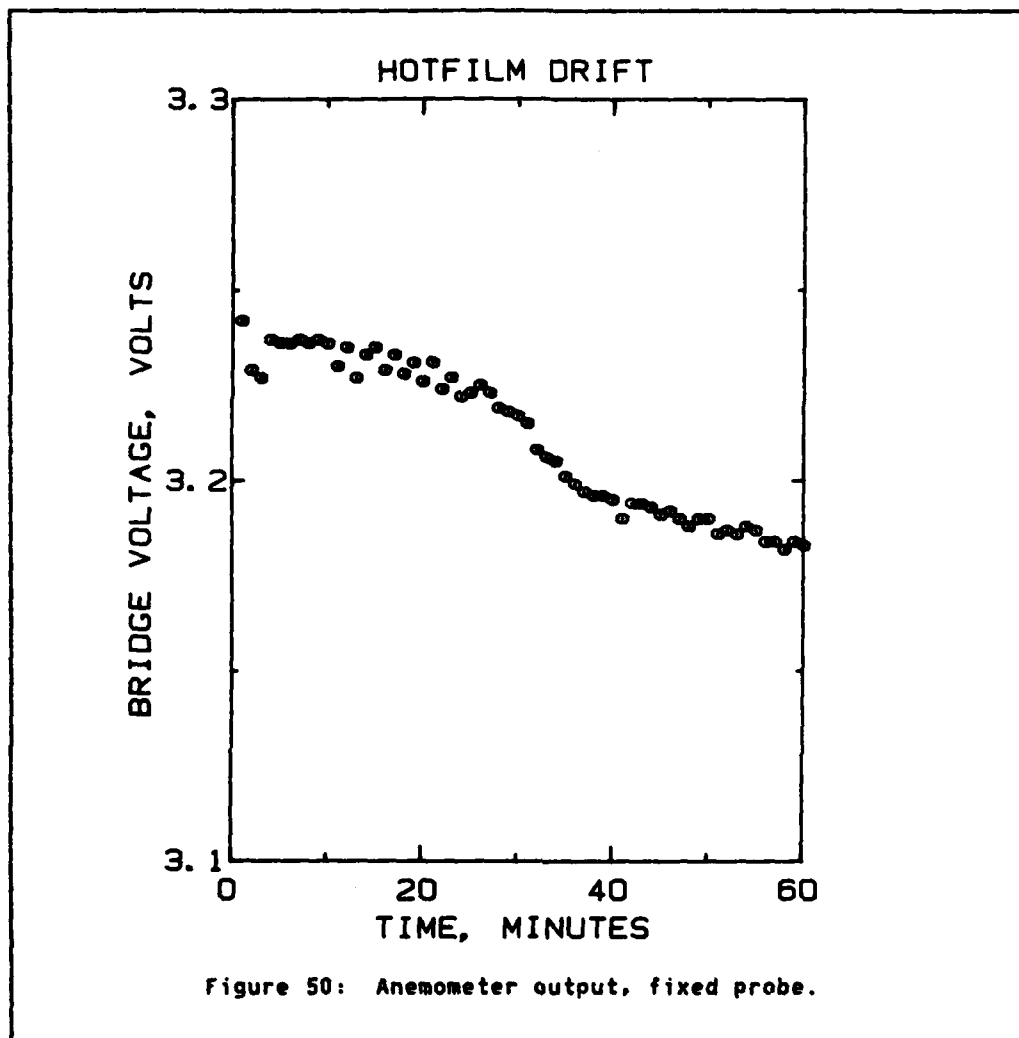
potential core region. Each point represents the average of 60 readings taken at 1 s intervals. Although the drop in voltage during the run is seen to be only a small percentage of the total voltage, a change in voltage of 0.1 V translates into an apparent change in velocity of 2 cm/s. which in this case is 20% of the mean velocity.

Figure 51: Variation of calibration with temperature (simulated by change in overheat ratio).
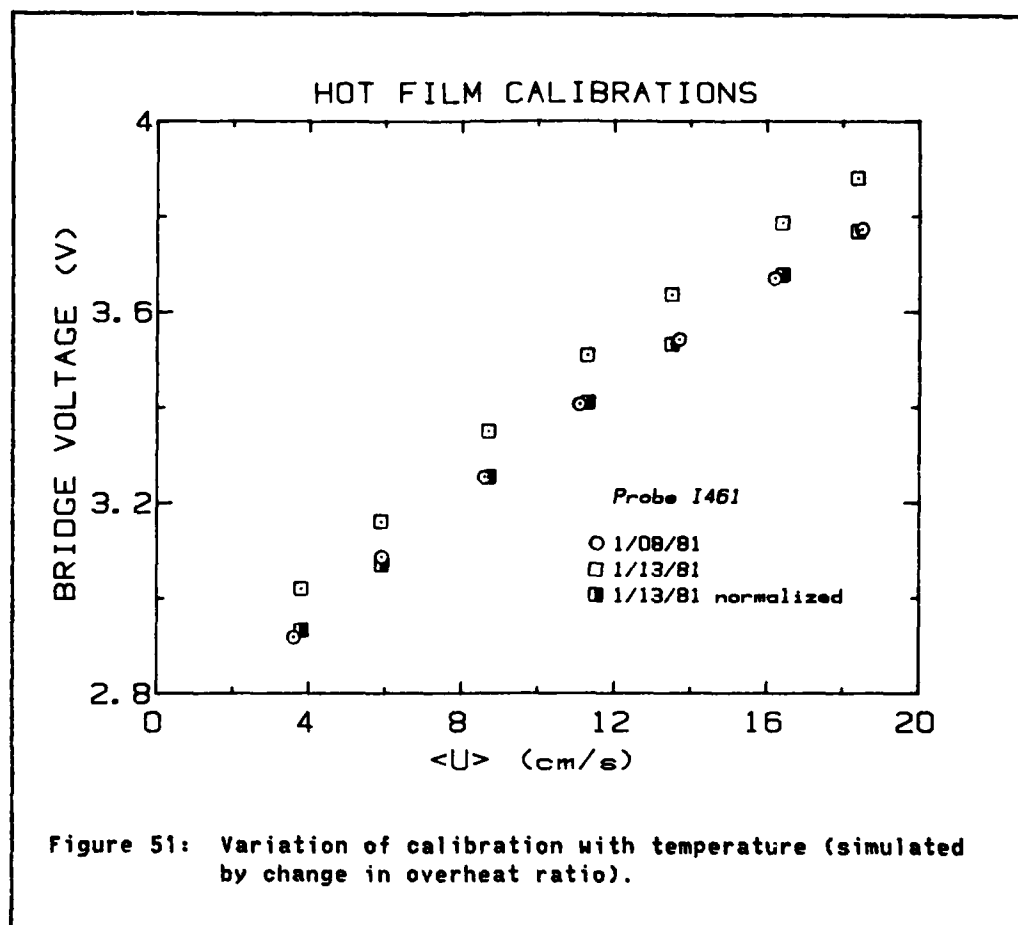
For the long running times needed to acquire stable, mean velocity profiles in our low speed flow, changes in the water temperature might also have a significant effect on the calibration, especially with the low overheat ratios that had to be used to prevent bubble formation on the sensor. Fig. 51 shows calibration curves taken on different days. The cold resistance of the probe was about 0.05 Ω higher on the 8th than on the 13th, but the operating resistance of the probe was set at 5.27 Ω on the 8th and 5.25 Ω on the 13th. Consequently, the probe was operated

at an overheat ratio of 1.07 on the 8th and 1.08 on the 13th. The results therefore simulate what would happen to the calibration curve of a probe if the fluid temperature were to decrease and emphasize the sensitivity of the probe to changes in the overheat ratio.

The similarity of the curves in Fig. 51, and the idea that small changes in the probe's response due to other factors, such as dirt build up, might also cause the calibration curve to shift slightly, suggested that a normalization procedure might be able to compensate for changes in the probe's response and thereby improve its reliability and utility.

The normalization procedure adopted corrects the anemometer's output using information about how the probe's response has changed at a location where the velocity is assumed not to change. Specifically, the normalized voltage, e_n, used to look up the flow speed from a calibration table, is obtained as follows:

$$e_n = e_m \frac{e_r}{e_r'}. \qquad (D.1)$$

The justification for this normalization procedure follows.

Wills[15] shows that for most situations of practical interest, the heat transfer from a cylindrical hot wire or hot film, expressed as a dimensionless Nusselt number, is a function of only the Reynold number viz.

$$Nu = f(Re). \qquad (D.2)$$

This was the case in our flow. Nu is defined as

----

[15] Wills, J. A. B. (1980) "Hot-wire and hot-film anemometry", National Maritime Institute, May 1980.

- 134 -

$$Nu=\frac{H}{\pi k_{eff}\ell(\theta_{op}-\theta_a)}$$
(D.3)

and

$$Re=\frac{ud}{\nu}.$$
(D.4)

The sensor is heated by the current which flows through it due to a voltage, e. Part of the heat is lost through conduction to the sensor supports. For hot films, this heat is probably not negligeable. The heat lost to the fluid by convection is therefore some fraction of the total heat generated in the sensor:

$$H=\gamma\frac{e^2}{R_{op}}.$$
(D.5)

Since the heat lost through conduction ultimately ends up back in the fluid, and the temperature gradient over which the conduction occurs is the same as for convection from the sensor, γ is not expected to vary significantly. Substituting Eqs. D.3-D.5 into Eq. D.2 gives

$$\frac{\gamma e^2}{R_{op}\pi k_{eff}\ell(\theta_{op}-\theta_a)}=f\left(\frac{ud}{\nu}\right).$$
(D.6)

Note that everything on the left hand side of Eq. D.6 except for e does not depend on u. We can then write

$$\Psi e^2=f\left(\frac{ud}{\nu}\right)$$
(D.7)

where Ψ depends on the operating conditions of the probe but not the fluid velocity. In the discussion which follows, the variation of ν with temperature (about 1% per °F) will be assumed negligeable; this was the case for our flow. Dirt accumulating on the sensor affects the effective

diameter of the sensor, but if we assume most of the larger dirt particles can be shaken off, then d should remain fairly constant.

We can now demonstrate how the normalization procedure works. Suppose we calibrate the probe under a certain set of conditions. The variation of bridge voltage with fluid velocity can be represented by Eq. D.7. In particular, the voltage at a reference point can be expressed as

$$\Psi e_r^2 = f\left(\frac{u_r d}{\nu}\right). \tag{D.8}$$

Now suppose at some later time, we measure a voltage under different operating conditions at some point in the flow. The voltage and velocity there are related by

$$\Psi' e_m^2 = f\left(\frac{u_m d}{\nu}\right) \tag{D.9}$$

where Ψ' is unknown as is u_m. Ψ' can be determined by returning to the reference point and measuring the voltage corresponding to u_r under the new operating conditions:

$$\Psi' e_r'^2 = f\left(\frac{u_r d}{\nu}\right). \tag{D.10}$$

Combining Eqs. D.8 and D.10 we obtain

$$\Psi' = \Psi \frac{e_r^2}{e_r'^2}. \tag{D.11}$$

Substituting Eq. D.11 into Eq. D.9 yields

$$\Psi e'^2 \frac{e_r^2}{e_r'^2} = f\left(\frac{u_m d}{\nu}\right). \tag{D.12}$$

Comparing Eq. D.12 with Eq. D.7, we see that everything in Eq. D.12 is known except for u_m, which can then be found by inverting the function

f. In practice what we do is look up the velocity corresponding to the normalized voltage using the old calibration curve. For example, by applying this procedure to one of the curves in Fig. 51 the third curve results. Consequently, the 2 cm/s error, which would have occurred had the unnormalized voltages been used with the older calibration curve, is substantially reduced.

It is instructive to examine the sensitivity of Ψ to various parameters. Recall that

$$\Psi = \frac{\gamma}{R_{op}\pi k_{eff}\ell(\theta_{op}-\theta_a)}. \qquad (D.13)$$

R_{op} is generally not varied by more that 1% in order to achieve the same overheat ratio on any given day. k_{eff} can have a large effect on Ψ, as demonstrated by Fig. 50 if dirt is allowed to accumulate on the sensor. In the present tests, the constant movement of the probe between the measurement stations and the reference point appeared to keep k_{eff} fairly constant. However, a thin film of dirt can accumulate with time and slowly lower k_{eff}.

θ_{op} depends on the resistance value at which the sensor is operated. The resistance of the sensor varies approximately linearly with temperature:

$$R_{op}=R_c[1+\alpha(\theta_{op}-\theta_c)]. \qquad (D.14)$$

α is about 0.002 per $^\circ$C for the probes used in this study. Solving for θ_{op} and substituting into Eq. D.13,

$$\Psi = \frac{\gamma}{R_{op}\pi k_{eff}\ell\left[\left(\frac{R_{op}}{R_c} - 1\right)\frac{1}{\alpha} + \theta_c-\theta_a\right]}. \qquad (D.15)$$

- 137 -

In our study $\theta_c-\theta_a$ was generally less than 1^0C if the cold resistance of the probe was measured at the ambient temperature at the beginning of a run. The other term in the brackets represents the difference between the temperature of the sensor and the temperature at which the cold resistance of the sensor is measured and is on the order of 50^0C. This term turns out to be quite sensitive to the overheat ratio, R_{op}/R_c. A drift or other small change in R_{op} of 0.01 Ω (0.2%) results in a 3% change in this temperature difference term. Fortunately, as long as Ψ is independent of the fluid velocity, its variations aree compensated for by the normalization procedure as shown above.

It should be noted that this normalization procedure also has some nonlinear effect on the measured velocities if the actual reference velocity in the freestream changes. Because of the nonlinearity of the basic correlation, Eq. D.2, velocity ratios are not scaled linearly with voltage ratios. For example, an increase in the freestream velocity over the nominal reference velocity will cause the anemometer to increase the voltage applied to the probe. The normalization procedure scales all of the measured voltages so that the voltage at the reference point after normalization remains constant. The measured velocity at the reference point therefore remains constant. However, it's not as if all of the other actual velocities were scaled on the freestream velocity too. The normalization procedure multiplies the measured voltages by a fraction, e_r/e_r'. Due to the nonlinearity of the calibration curve, this is not equivalent to multiplying all the velocities by U_r/U_r'. It can be shown that, depending on the shape of the calibration curve, velocities other than the reference velocity are either overcorrected or undercor-

rected. For example, if the actual freestream velocity increases by 10%, the normalization reduces the measured voltages by an amount, say 3%, corresponding to a 9.1% reduction in the measured velocity at the reference point. However, velocities at other locations will be reduced by more or less than 9.1% since a 3% change in voltage corresponds to different changes in velocity at different locations on the calibration curve. Since the freestream velocity in the present study was carefully regulated, this side effect of the normalization procedure was probably negligeable.

Appendix E

SPECIALIZED TOOLS

Several tools were designed and fabricated to perform special tasks in the assembly and operation of the water channel. Shown in Fig. 52 are (a) a flexible tip, ball driver for placing and driving the socket head screws used to hold the inner walls in place, (b) a remote manipulator for retrieving objects dropped into the channel, (c) a hydrogen bubble wire holder, and (d) a modified syringe.

The ball driver was made by attaching a conventional ball driver tip, taken from a screwdriver handle, to a miniature universal joint and an extra long handle. A piece of vinyl tubing slipped over the joint gave the joint some rigidity so that the tip could be positioned as desired. Besides being easier to use than slot or Phillips head screwdrivers, ball drivers also allow you to temporarily hold on to a screw because of the way in which the ball fits into the socket head of the screw.

The remote manipulator was fashioned from a bicycle brake outfitted with modified caliper arms. The manipulator possessed enough dexterity to pick up thin plastic rulers dropped on the channel floor.

The hydrogen bubble wire holder was designed to allow easy replacement of broken wires while also affording the safety needed. The holder was fabricated from nonconductive plexiglas. The spacing between the two

Figure 52: Specialized tools: (a) ball driver, (b) remote manipulator, (c) bubble wire holder, and (d) syringe.

prongs was adjustable. The electrical leads running down the center of the stem terminated at small screws sticking out of the base of each prong. A pair of nuts on each screw were used to clamp the wires in place. Parafin wax applied with a brush insulated terminals from the water. The vinyl tube wound around the stem, corkscrew fashion, kept the stem from oscillating in the flow by disrupting the vortices being shed.

Finally, the modified syringe, used for injecting dyes, was fabricated from two syringe bodies joined with a plexiglas adapter.

Appendix F

FILM NARRATIVE

"Turbulent Boundary Layers on Concave Walls" is a 16 mm, color, silent film, 430' long, which runs for 12 minutes if projected at 24 frames per second (sound speed). The film was produced by Albert H. Jeans and James P. Johnston of the Thermosciences Division of the Dept. of Mechanical Engineering, Stanford Univ. in 1981. The film gives some background information and then depicts systematic visual surveys of the flowfield using dyes and hydrogen bubbles. A scene-by-scene narrative follows.

1. Title and producers.

2. Schematic plan view of the concave flow facility. Water enters from an underground sump through a perforated pipe. The flow passes through a perforated plate, honeycomb, and screens to achieve uniformity and low turbulence levels. A nozzle with a contraction ratio of 4:1 accelerates the flow up to the nominal running speed of 15 cm/s. The laminar boundary layers are tripped about 1 m downstream of the nozzle exit. The flow passes through a 90° bend and a 2.5 m-long recovery region before returning to the sump.

3. Color diagram of the test section. The boundary layers are about 7.5 cm thick at the start of curvature with a momentum thickness Reynolds number of about 1300. The channel depth is about 1.1 m

and the radius of curvature 1.36 m. The opposing, convex wall was designed to minimize the streamwise pressure gradient at the test wall.

4. Diagram of dye injection technique. To visualize the flow near the wall, dye is injected through narrow slots into the viscous sublayer and lit from behind.

5. Diagram of hydrogen bubble technique. To visualize the flow away from the wall hydrogen bubbles are used to mark the flow. The diagram shows the effective viewing angle which will be seen in the movies. In reality, this viewing angle is accomplished using a mirror placed in the flow, downstream of the bubble wires.

6. The dye movies were shot at 24 frames per second, the hydrogen bubble movies at 45 frames per second.

7. A scale ruled in centimeters appears on the wall in many of the scenes. Diagram showing the location of the first region to be visualized: the flat plate region upstream of the curve.

8. This region is characterized by uniformly distributed streaks and bursts near the wall.

9. Dye is being injected through two slots about 20 cm apart. We see the usual streaky structure characteristic of turbulent boundary layers. The nondimensional streak spacing λ^+ agrees with the generally quoted value of 100. Velocity measurements made in this region also indicate a normal turbulent flatplate boundary layer.

10. Single bubble wire at y=0.6 cm (y^+=44), pulsed continuously. Typical eddies are 1 or 2 cm in size although larger ones occur occasionally. Streaks appear as low-speed regions which oscillate back and forth. Bursting disrupts the bubble lines soon after they are generated.

11. Single wire at y=1.0 cm (y^+=73), pulsed intermittently. This pulsing pattern does a better job of depicting the eddies as they travel downstream. Note the appearance of streamwise vorticity.

12. Dual bubble wires are always separated by 4 cm and are pulsed intermittently.

13. Dual wires, lower wire at y=1.0 cm. Note the lack of correlation between the two bubble lines, another indication that the eddies in this region are not very large. Turbulent activity seems to be diminishing farther from the wall.

14. Dual wires, lower wire at y=5.0 cm. The upper wire is now outside of the boundary layer. The bubble lines from the upper wire remain intact aside from occasional eddies from below.

15. Diagram showing the region in the curve which was observed, a region starting at about 30^0.

16. The flow in this region appears to be dominated by randomly distributed large-scale sweeps (inflows) and ejections (outflows).

17. Dye visualization. Note how the dye collects into large streamers, which are spaced about 10 cm apart on the average. The

boundary layer thickness is also about 10 cm here. The streamers are actually formed by sweeps from the outer flow which push aside the fluid near the wall. The sweeps appear randomly in position and time and seem to greatly reduce the bursting activity seen in the flatplate boundary layer.

18. Bubble wire at y=0.6 cm, pulsed continuously. Here again we see the wall fluid being pushed into piles by sweeps from the outer flow. Bursting is greatly diminished where the sweeps impinge on the wall.

19. Bubble wire at y=1.0 cm, pulsed intermittently. The vertical movement of the fluid is much greater here than in the flat plate region. Typical eddies are about 4 or 5 cm in size.

20. Dual wires, lower wire at y=1.0 cm. Motions depicted by the bubble lines appear highly correlated, indicating that the large-scale eddies extend a long distance through the boundary layer. The large-scale motions also appear to be promoting a lot of mixing and turbulence production far from the wall.

21. Dual wires, lower wire at y=5.0 cm. The upper wire is near the edge of the boundary layer. Many of the ejections appear quite strong at the upper wire position.

22. Wire at 9.0 cm, pulsed continuously. This visualization gives you a better idea of the planar distribution of the ejections. The ejections are irregularly shaped and randomly distributed. Note the intense longitudinal vorticity occasionally generated at the interfaces between the ejections and the outer flow.

23. The flow displays the same qualitative features at other stations
    around the curve, the differences being that the large-scale
    motions appear to intensify and grow somewhat larger.

24. In the recovery region downstream of the curve, bursting is
    greatly suppressed over large regions.

25. Diagram showing region visualized in recovery region.

26. Dye visualization. Note large regions of low turbulent activity.
    Perhaps, the large-scale motions in the curve have removed so
    much fluid from the wall that a new boundary layer is growing
    here.

27. Bubble wire at 0.6 cm, pulsed continuously. The large patches of
    laminar-like fluid alternate with patches of more conventional
    bursting activity.

28. Dual wires, lower wire at y=1.0 cm. Remnants of the large-scale
    motions still appear quite strong. Chunks of laminar-like fluid
    also appear. These may be remnants of the potential core or zones
    where relaminarization has occurred; at this time no definite
    conclusions can be drawn.

29. Dual wires, lower wire at y=5.0 cm. Large scale motions dominate
    the entire flowfield. The scale and inertia of these motions evi-
    dentally makes them very resistant to decay.

30. Single wire at y=9.0 cm, pulsed continuously. Again, we see large
    patches of laminar-like fluid. Velocity and turbulence

measurements show no sign of a potential core by the 75^0 location. Visualization gives us a better idea of what is happening.

31. This work was funded by the Air Force Office of Scientific Research.

Appendix G

DATA SETS

The data sets used in the graphs are listed below in two-column format. Except where noted, the anemometer was sampled at 6 Hz for a period T=300 s to obtain the mean velocity and turbulence intensity at each location. YO is a shift applied to the y-coordinates in order to partially compensate for positioning errors. YO was determined by examining the near-wall data and estimating the probable location of the wall by extrapolation. The value of YO given in the data sets is the amount that was added to the nominal y-coordinates to produce the coordinates shown. THETA, expressed in degrees, is the location in the curve at which some of the data sets were taken. W is the channel width at the streamwise location at which the cross-channel profiles were taken. TEMP is the water temperature, in degrees Fahrenheit, at the time the run was started. The integer following the title of each data set is the number of points in that set.

LAM9 5/11/81 X=400 CM T=20 SEC TEMP=76
27

Y CM	Z CM	<U> CM/S	<U'*U'>
2.000E-01	0.000E-01	1.130E+00	6.000E-03
4.000E-01	0.000E-01	1.530E+00	5.900E-03
6.000E-01	0.000E-01	1.850E+00	5.000E-03
8.000E-01	0.000E-01	2.140E+00	5.000E-03
1.000E+00	0.000E-01	2.500E+00	4.000E-03
1.200E+00	0.000E-01	2.920E+00	1.000E-02
1.400E+00	0.000E-01	3.070E+00	7.100E-02
1.600E+00	0.000E-01	3.450E+00	2.300E-02
1.800E+00	0.000E-01	3.710E+00	2.700E-02
2.000E+00	0.000E-01	4.280E+00	1.400E-02
2.200E+00	0.000E-01	4.630E+00	2.400E-02
2.400E+00	0.000E-01	4.790E+00	7.000E-03
2.600E+00	0.000E-01	5.150E+00	8.000E-03
2.800E+00	0.000E-01	5.110E+00	3.130E-01
3.000E+00	0.000E-01	5.520E+00	9.000E-03
3.300E+00	0.000E-01	5.670E+00	1.100E-02
3.600E+00	0.000E-01	5.770E+00	4.000E-03
4.000E+00	0.000E-01	5.860E+00	4.000E-03
4.400E+00	0.000E-01	5.800E+00	5.000E-03
5.000E+00	0.000E-01	5.810E+00	9.000E-03
6.000E+00	0.000E-01	5.840E+00	7.000E-03
7.000E+00	0.000E-01	5.840E+00	4.000E-03
8.000E+00	0.000E-01	5.800E+00	7.000E-03
1.000E+01	0.000E-01	5.780E+00	5.000E-03
1.200E+01	0.000E-01	5.740E+00	1.500E-02
1.400E+01	0.000E-01	5.750E+00	6.000E-03
1.600E+01	0.000E-01	5.720E+00	7.000E-03

LAM10 6/11/81 X=400 CM, CONTROL WALL
T=20 SEC TEMP=76
27

Y CM	Z CM	<U> CM/S	<U'*U'>
2.000E-01	0.000E-01	1.370E+00	8.000E-03
4.000E-01	0.000E-01	1.870E+00	7.000E-03
6.000E-01	0.000E-01	2.210E+00	3.000E-03
8.000E-01	0.000E-01	2.510E+00	4.000E-03
1.000E+00	0.000E-01	2.770E+00	2.000E-03
1.200E+00	0.000E-01	3.230E+00	7.000E-03
1.400E+00	0.000E-01	3.490E+00	6.000E-03
1.600E+00	0.000E-01	3.920E+00	6.000E-03
1.800E+00	0.000E-01	4.250E+00	5.000E-03
2.000E+00	0.000E-01	4.540E+00	6.000E-03
2.200E+00	0.000E-01	4.770E+00	8.000E-03
2.400E+00	0.000E-01	5.040E+00	5.000E-03
2.600E+00	0.000E-01	5.190E+00	3.000E-03
2.800E+00	0.000E-01	5.390E+00	4.000E-03
3.000E+00	0.000E-01	5.490E+00	4.000E-03
3.300E+00	0.000E-01	5.570E+00	7.000E-03
3.600E+00	0.000E-01	5.670E+00	3.000E-03
4.000E+00	0.000E-01	5.740E+00	6.000E-03
4.400E+00	0.000E-01	5.760E+00	8.000E-03

5.000E+00 | 0.000E-01 | 5.790E+00 | 5.000E-03
(continued, right column top)

Y CM	Z CM	<U> CM/S	<U'*U'>
5.000E+00	0.000E-01	5.790E+00	5.000E-03
6.000E+00	0.000E-01	5.760E+00	5.000E-03
7.000E+00	0.000E-01	5.770E+00	7.000E-03
8.000E+00	0.000E-01	5.760E+00	4.000E-03
1.000E+01	0.000E-01	5.740E+00	6.000E-03
1.200E+01	0.000E-01	5.730E+00	7.000E-03
1.400E+01	0.000E-01	5.790E+00	5.000E-03
1.600E+01	0.000E-01	5.750E+00	4.000E-03

LAM11 6/11/81 X=400 CM T=20 SEC TEMP=76
27

Y CM	Z CM	<U> CM/S	<U'*U'>
2.000E-01	0.000E-01	1.020E+00	0.000E-01
4.000E-01	0.000E-01	1.390E+00	6.000E-03
6.000E-01	0.000E-01	1.930E+00	3.000E-03
8.000E-01	0.000E-01	2.210E+00	2.000E-03
1.000E+00	0.000E-01	2.530E+00	3.000E-03
1.200E+00	0.000E-01	2.830E+00	4.000E-03
1.400E+00	0.000E-01	3.440E+00	8.300E-02
1.600E+00	0.000E-01	3.650E+00	9.000E-03
1.800E+00	0.000E-01	4.220E+00	5.000E-03
2.000E+00	0.000E-01	4.500E+00	1.000E-02
2.200E+00	0.000E-01	4.720E+00	5.000E-03
2.400E+00	0.000E-01	4.820E+00	4.000E-03
2.600E+00	0.000E-01	5.120E+00	5.000E-03
2.800E+00	0.300E-01	5.240E+00	6.000E-03
3.000E+00	0.000E-01	5.400E+00	3.000E-03
3.300E+00	0.000E-01	5.660E+00	4.000E-03
3.600E+00	0.000E-01	5.720E+00	6.000E-03
4.000E+00	0.000E-01	5.800E+00	8.000E-03
4.400E+00	0.000E-01	5.810E+00	5.000E-03
5.000E+00	0.000E-01	5.790E+00	7.000E-03
6.000E+00	0.000E-01	5.790E+00	7.000E-03
7.000E+00	0.000E-01	5.840E+00	6.000E-03
8.000E+00	0.000E-01	5.820E+00	5.000E-03
1.000E+01	0.000E-01	5.770E+00	5.000E-03
1.200E+01	0.000E-01	5.740E+00	7.000E-03
1.400E+01	0.000E-01	5.760E+00	4.000E-03
1.600E+01	0.000E-01	5.670E+00	5.000E-03

QUAL3 5/13/81 X=400 CM
Z=20 CM Y0=-.03 CM TEMP=76
22

Y CM	Z CM	<U> CM/S
7.000E-02	2.000E+01	3.500E+00
9.000E-02	2.000E+01	4.390E+00
1.100E-01	2.000E+01	5.230E+00
1.400E-01	2.000E+01	6.070E+00
1.700E-01	2.000E+01	6.730E+00
2.100E-01	2.000E+01	7.070E+00
2.700E-01	2.000E+01	8.120E+00
3.700E-01	2.000E+01	8.780E+00
4.900E-01	2.000E+01	9.270E+00
6.200E-01	2.000E+01	9.850E+00

Y CM	Z CM	<U> CM/S
7.900E-01	2.000E+01	1.005E+01
1.010E+00	2.000E+01	1.064E+01
1.270E+00	2.000E+01	1.096E+01
1.600E+00	2.000E+01	1.126E+01
2.000E+00	2.000E+01	1.173E+01
2.470E+00	2.000E+01	1.198E+01
3.160E+00	2.000E+01	1.250E+01
3.670E+00	2.000E+01	1.278E+01
4.280E+00	2.000E+01	1.333E+01
4.970E+00	2.000E+01	1.381E+01
5.970E+00	2.000E+01	1.429E+01
7.970E+00	2.000E+01	1.479E+01

Y CM	Z CM	<U> CM/S	<U'*U'>
1.280E+00	0.000E-01	1.107E+01	1.373E+00
1.610E+00	0.000E-01	1.144E+01	9.670E-01
2.010E+00	0.000E-01	1.191E+01	1.002E+00
2.486E+00	0.000E-01	1.236E+01	9.540E-01
3.170E+00	0.000E-01	1.303E+01	8.620E-01
3.680E+00	0.000E-01	1.347E+01	7.490E-01
4.290E+00	0.000E-01	1.377E+01	6.180E-01
4.980E+00	0.000E-01	1.418E+01	3.890E-01
5.980E+00	0.000E-01	1.461E+01	1.560E-01
7.980E+00	0.000E-01	1.515E+01	1.000E-02
9.980E+00	0.000E-01	1.482E+01	7.000E-03
1.198E+01	0.000E-01	1.481E+01	6.000E-03

QUAL1 5/13/81 X=400 CM
Z=10 CM YO=.05 CM TEMP=76
22

Y CM	Z CM	<U> CM/S
1.500E-01	1.000E+01	5.730E+00
1.700E-01	1.000E+01	6.360E+00
1.900E-01	1.000E+01	6.630E+00
2.200E-01	1.000E+01	7.100E+00
2.500E-01	1.000E+01	7.590E+00
2.900E-01	1.000E+01	8.240E+00
3.500E-01	1.000E+01	8.680E+00
4.500E-01	1.000E+01	9.390E+00
5.700E-01	1.000E+01	9.700E+00
7.000E-01	1.000E+01	1.007E+01
8.700E-01	1.000E+01	1.042E+01
1.090E+00	1.000E+01	1.066E+01
1.350E+00	1.000E+01	1.104E+01
1.680E+00	1.000E+01	1.150E+01
2.080E+00	1.000E+01	1.181E+01
2.550E+00	1.000E+01	1.224E+01
3.240E+00	1.000E+01	1.267E+01
3.750E+00	1.000E+01	1.314E+01
4.360E+00	1.000E+01	1.366E+01
5.050E+00	1.000E+01	1.417E+01
6.050E+00	1.000E+01	1.448E+01
8.050E+00	1.000E+01	1.484E+01

FLAT1 5/11/81 X=400 CM
Z=0 CM YO=-.02 CM TEMP=76
22

Y CM	Z CM	<U> CM/S	<U'*U'>
1.200E-01	0.000E-01	5.200E+00	2.935E+00
1.500E-01	0.000E-01	6.140E+00	3.435E+00
1.800E-01	0.000E-01	6.730E+00	3.211E+00
2.200E-01	0.000E-01	7.350E+00	3.379E+00
2.800E-01	0.000E-01	8.320E+00	2.873E+00
3.800E-01	0.000E-01	9.080E+00	2.423E+00
5.000E-01	0.000E-01	9.670E+00	2.010E+00
6.300E-01	0.000E-01	1.017E+01	1.711E+00
8.000E-01	0.000E-01	1.039E+01	1.486E+00
1.020E+00	0.000E-01	1.079E+01	1.332E+00

FLAT2 5/11/81 X=400 CM
Z=0 YO=-.02 TEMP=76
20

Y CM	Z CM	<U> CM/S	<U'*U'>
1.200E-01	0.000E-01	5.150E+00	3.264E+00
1.500E-01	0.000E-01	5.880E+00	3.273E+00
1.800E-01	0.000E-01	6.690E+00	3.433E+00
2.200E-01	0.000E-01	7.530E+00	3.184E+00
2.800E-01	0.000E-01	8.090E+00	2.747E+00
3.800E-01	0.000E-01	9.040E+00	2.474E+00
5.000E-01	0.000E-01	9.650E+00	2.122E+00
6.300E-01	0.000E-01	1.007E+01	1.609E+00
8.000E-01	0.000E-01	1.050E+01	1.561E+00
1.020E+00	0.000E-01	1.080E+01	1.224E+00
1.280E+00	0.000E-01	1.112E+01	1.281E+00
1.610E+00	0.000E-01	1.142E+01	1.200E+00
2.010E+00	0.000E-01	1.177E+01	1.037E+00
2.480E+00	0.000E-01	1.235E+01	9.130E-01
3.170E+00	0.000E-01	1.291E+01	9.260E-01
3.680E+00	0.000E-01	1.333E+01	8.790E-01
4.290E+00	0.000E-01	1.387E+01	6.230E-01
4.980E+00	0.000E-01	1.427E+01	3.460E-01
5.980E+00	0.000E-01	1.464E+01	1.780E-01
7.980E+00	0.000E-01	1.489E+01	1.900E-02

FLAT5 5/28/81 X=400 CM
Z=0 CM TEMP=81
26

Y CM	Z CM	<U> CM/S	<U'*U'>
1.000E-01	0.000E-01	4.870E+00	2.532E+00
1.200E-01	0.000E-01	4.920E+00	2.554E+00
1.400E-01	0.000E-01	5.580E+00	3.108E+00
1.700E-01	0.009E-01	5.910E+00	3.113E+00
2.000E-01	0.000E-01	6.600E+00	3.475E+00
2.400E-01	0.000E-01	7.180E+00	3.155E+00
3.000E-01	0.000E-01	8.010E+00	3.069E+00
4.000E-01	0.000E-01	8.960E+00	2.551E+00
5.200E-01	0.000E-01	9.490E+00	1.922E+00
6.500E-01	0.000E-01	9.720E+00	1.582E+00
8.200E-01	0.000E-01	1.026E+01	1.280E+00
1.040E+00	0.000E-01	1.056E+01	1.120E+00

1.300E+00	0.000E-01	1.096E+01	1.055E+00	3.700E-01	-2.000E+01	9.260E+00
1.630E+00	0.000E-01	1.128E+01	9.870E-01	4.900E-01	-2.000E+01	9.850E+00
2.030E+00	0.000E-01	1.173E+01	1.060E+00	6.200E-01	-2.000E+01	1.021E+01
2.500E+00	0.000E-01	1.208E+01	9.390E-01	7.900E-01	-2.000E+01	1.066E+01
3.190E+00	0.000E-01	1.265E+01	9.240E-01	1.010E+00	-2.000E+01	1.119E+01
3.700E+00	0.000E-01	1.301E+01	8.430E-01	1.270E+00	-2.000E+01	1.140E+01
4.310E+00	0.000E-01	1.350E+01	7.700E-01	1.600E+00	-2.000E+01	1.189E+01
5.000E+00	0.000E-01	1.401E+01	5.920E-01	2.000E+00	-2.000E+01	1.220E+01
6.000E+00	0.000E-01	1.455E+01	2.700E-01	2.470E+00	-2.000E+01	1.261E+01
8.000E+00	0.000E-01	1.493E+01	3.700E-02	3.160E+00	-2.000E+01	1.325E+01
1.000E+01	0.000E-01	1.485E+01	1.600E-02	3.670E+00	-2.000E+01	1.378E+01
1.200E+01	0.000E-01	1.473E+01	1.200E-02	4.260E+00	-2.000E+01	1.423E+01
1.400E+01	0.000E-01	1.477E+01	1.000E-02	4.970E+00	-2.000E+01	1.450E+01
1.600E+01	0.000E-01	1.471E+01	2.900E-02	5.970E+00	-2.000E+01	1.474E+01
				7.970E+00	-2.000E+01	1.490E+01

QUAL2 5/13/81 X=400 CM
Z=-10 CM Y0=0 CM TEMP=76
22

Y CM	Z CM	<U> CM/S
1.000E-01	-1.000E+01	4.410E+00
1.200E-01	-1.000E+01	4.710E+00
1.400E-01	-1.000E+01	5.670E+00
1.700E-01	-1.000E+01	5.960E+00
2.000E-01	-1.000E+01	6.670E+00
2.400E-01	-1.000E+01	7.470E+00
3.000E-01	-1.000E+01	8.500E+00
4.000E-01	-1.000E+01	9.130E+00
5.200E-01	-1.000E+01	9.520E+00
6.500E-01	-1.000E+01	1.008E+01
8.200E-01	-1.000E+01	1.049E+01
1.040E+00	-1.000E+01	1.091E+01
1.300E+00	-1.000E+01	1.119E+01
1.630E+00	-1.000E+01	1.169E+01
2.030E+00	-1.000E+01	1.194E+01
2.500E+00	-1.000E+01	1.237E+01
3.190E+00	-1.000E+01	1.290E+01
3.700E+00	-1.000E+01	1.342E+01
4.310E+00	-1.000E+01	1.390E+01
5.000E+00	-1.000E+01	1.427E+01
6.000E+00	-1.000E+01	1.464E+01
8.000E+00	-1.000E+01	1.490E+01

QUAL7 5/16/81 X=400 CM
Z=-20 CM Y0=-.03 CM TEMP=76
22

Y CM	Z CM	<U> CM/S
7.000E-02	-2.000E+01	3.570E+00
9.000E-02	-2.000E+01	4.150E+00
1.100E-01	-2.000E+01	4.920E+00
1.400E-01	-2.000E+01	6.190E+00
1.700E-01	-2.000E+01	6.690E+00
2.100E-01	-2.000E+01	7.430E+00
2.700E-01	-2.000E+01	8.320E+00

FL400=FLAT5+FLAT3 5/27-28/81
X=400 CM N=27.0 CM TEMP=81
54

Y CM	Z CM	<U> CM/S	<U'*U'>
1.000E-01	0.000E-01	4.870E+00	2.532E+00
1.200E-01	0.000E-01	4.920E+00	2.554E+00
1.400E-01	0.000E-01	5.580E+00	3.108E+00
1.700E-01	0.000E-01	5.910E+00	3.113E+00
2.000E-01	0.000E-01	6.600E+00	3.475E+00
2.400E-01	0.000E-01	7.180E+00	3.155E+00
3.000E-01	0.000E-01	8.010E+00	3.069E+00
4.000E-01	0.000E-01	8.960E+00	2.551E+00
5.200E-01	0.000E-01	9.490E+00	1.922E+00
6.500E-01	0.000E-01	9.720E+00	1.582E+00
8.200E-01	0.000E-01	1.026E+01	1.280E+00
1.040E+00	0.000E-01	1.056E+01	1.120E+00
1.300E+00	0.000E-01	1.096E+01	1.055E+00
1.630E+00	0.000E-01	1.128E+01	9.870E-01
2.030E+00	0.000E-01	1.173E+01	1.060E+00
2.500E+00	0.000E-01	1.208E+01	9.390E-01
3.190E+00	0.000E-01	1.265E+01	9.240E-01
3.700E+00	0.000E-01	1.301E+01	8.430E-01
4.310E+00	0.000E-01	1.350E+01	7.700E-01
5.000E+00	0.000E-01	1.401E+01	5.920E-01
6.001E+00	0.000E-01	1.430E+01	4.180E-01
8.000E+00	0.000E-01	1.493E+01	3.700E-02
8.001E+00	0.000E-01	1.477E+01	4.800E-02
1.000E+01	0.000E-01	1.485E+01	1.600E-02
1.001E+01	0.000E-01	1.478E+01	2.100E-02
1.200E+01	0.000E-01	1.473E+01	1.200E-02
1.201E+01	0.000E-01	1.472E+01	1.600E-02
1.400E+01	0.000E-01	1.477E+01	1.000E-02
1.401E+01	0.000E-01	1.478E+01	2.000E-02
1.600E+01	0.000E-01	1.471E+01	2.900E-02
1.601E+01	0.000E-01	1.475E+01	2.500E-02
1.800E+01	0.000E-01	1.466E+01	1.150E-01
2.000E+01	0.000E-01	1.377E+01	5.070E-01

Y CM	Z CM	<U> CM/S	<U'*U'>
2.100E+01	0.000E-01	1.329E+01	7.110E-01
2.169E+01	0.000E-01	1.281E+01	8.150E-01
2.230E+01	0.000E-01	1.246E+01	9.070E-01
2.281E+01	0.000E-01	1.216E+01	8.770E-01
2.350E+01	0.000E-01	1.175E+01	9.280E-01
2.397E+01	0.000E-01	1.125E+01	9.810E-01
2.437E+01	0.000E-01	1.092E+01	9.390E-01
2.470E+01	0.000E-01	1.080E+01	1.015E+00
2.496E+01	0.000E-01	1.042E+01	1.026E+00
2.518E+01	0.000E-01	1.017E+01	1.264E+00
2.535E+01	0.000E-01	9.900E+00	1.379E+00
2.548E+01	0.000E-01	9.600E+00	1.646E+00
2.560E+01	0.000E-01	9.260E+00	1.951E+00
2.570E+01	0.000E-01	8.580E+00	2.609E+00
2.576E+01	0.000E-01	8.190E+00	2.773E+00
2.580E+01	0.000E-01	8.130E+00	2.737E+00
2.583E+01	0.000E-01	7.310E+00	3.276E+00
2.586E+01	0.000E-01	6.880E+00	3.285E+00
2.588E+01	0.000E-01	6.570E+00	3.134E+00
2.590E+01	0.000E-01	6.370E+00	3.302E+00

CRV30=CURV1+CURV4 5/81
THETA=30 W=25.0 CM TEMP=81
49

Y CM	Z CM	<U> CM/S	<U'*U'>
1.200E-01	0.000E-01	3.930E+00	1.712E+00
1.400E-01	0.000E-01	4.630E+00	2.314E+00
1.700E-01	0.000E-01	5.890E+00	3.201E+00
2.000E-01	0.000E-01	7.080E+00	3.965E+00
2.400E-01	0.000E-01	8.130E+00	3.596E+00
3.000E-01	0.000E-01	8.660E+00	3.634E+00
4.000E-01	0.000E-01	9.710E+00	3.378E+00
5.200E-01	0.000E-01	1.032E+01	2.300E+00
6.500E-01	0.000E-01	1.050E+01	1.877E+00
8.200E-01	0.000E-01	1.078E+01	1.925E+00
1.040E+00	0.000E-01	1.106E+01	1.750E+00
1.300E+00	0.000E-01	1.120E+01	1.535E+00
1.630E+00	0.000E-01	1.147E+01	1.459E+00
2.030E+00	0.000E-01	1.181E+01	1.478E+00
2.500E+00	0.000E-01	1.198E+01	1.478E+00
3.190E+00	0.000E-01	1.247E+01	1.442E+00
3.700E+00	0.000E-01	1.260E+01	1.553E+00
4.310E+00	0.000E-01	1.312E+01	1.381E+00
5.000E+00	0.000E-01	1.353E+01	1.151E+00
5.001E+00	0.000E-01	1.354E+01	1.120E+00
6.000E+00	0.000E-01	1.411E+01	7.030E-01
7.000E+00	0.000E-01	1.461E+01	5.370E-01
8.000E+00	0.000E-01	1.491E+01	2.350E-01
9.000E+00	0.000E-01	1.510E+01	1.360E-01
1.100E+01	0.000E-01	1.553E+01	3.800E-02
1.300E+01	0.000E-01	1.568E+01	3.280E-02
1.500E+01	0.000E-01	1.602E+01	2.600E-02
1.700E+01	0.000E-01	1.602E+01	7.000E-02
1.900E+01	0.000E-01	1.573E+01	2.240E-01

Y CM	Z CM	<U> CM/S	<U'*U'>
2.000E+01	0.000E-01	1.559E+01	2.900E-01
2.069E+01	0.000E-01	1.517E+01	2.520E-01
2.130E+01	0.000E-01	1.513E+01	2.670E-01
2.181E+01	0.000E-01	1.488E+01	2.770E-01
2.250E+01	0.000E-01	1.467E+01	3.010E-01
2.297E+01	0.000E-01	1.438E+01	3.560E-01
2.337E+01	0.000E-01	1.410E+01	4.240E-01
2.370E+01	0.000E-01	1.374E+01	6.530E-01
2.396E+01	0.000E-01	1.312E+01	1.030E+00
2.418E+01	0.000E-01	1.264E+01	1.466E+00
2.435E+01	0.000E-01	1.187E+01	1.831E+00
2.448E+01	0.000E-01	1.110E+01	2.111E+00
2.460E+01	0.000E-01	9.920E+00	2.761E+00
2.470E+01	0.000E-01	8.750E+00	3.083E+00
2.476E+01	0.000E-01	7.620E+00	3.452E+00
2.480E+01	0.000E-01	6.750E+00	3.617E+00
2.483E+01	0.000E-01	6.350E+00	3.452E+00
2.486E+01	0.000E-01	5.690E+00	3.392E+00
2.488E+01	0.000E-01	4.570E+00	2.609E+00
2.490E+01	0.000E-01	3.810E+00	2.211E+00

CRV75=CURV3+CURV5 5/81
THETA=75 W=25.7 CM TEMP=81
49

Y CM	Z CM	<U> CM/S	<U'*U'>
1.200E-01	0.000E-01	6.560E+00	4.258E+00
1.400E-01	0.000E-01	7.620E+00	4.219E+00
1.700E-01	0.000E-01	8.010E+00	4.844E+00
2.000E-01	0.000E-01	8.600E+00	4.457E+00
2.400E-01	0.000E-01	9.310E+00	4.693E+00
3.000E-01	0.000E-01	1.028E+01	4.265E+00
4.000E-01	0.000E-01	1.086E+01	4.001E+00
5.200E-01	0.000E-01	1.135E+01	3.256E+00
6.500E-01	0.000E-01	1.171E+01	2.874E+00
8.200E-01	0.000E-01	1.211E+01	2.406E+00
1.040E+00	0.000E-01	1.245E+01	2.023E+00
1.300E+00	0.000E-01	1.299E+01	1.660E+00
1.630E+00	0.000E-01	1.287E+01	1.414E+00
2.030E+00	0.000E-01	1.302E+01	1.369E+00
2.500E+00	0.000E-01	1.325E+01	1.353E+00
3.190E+00	0.000E-01	1.354E+01	1.138E+00
3.700E+00	0.000E-01	1.368E+01	1.236E+00
4.310E+00	0.000E-01	1.357E+01	1.187E+00
5.000E+00	0.000E-01	1.393E+01	9.750E-01
6.000E+00	0.000E-01	1.410E+01	9.920E-01
8.000E+00	0.000E-01	1.474E+01	7.260E-01
1.080E+01	0.000E-01	1.536E+01	4.870E-01
1.200E+01	0.000E-01	1.583E+01	3.640E-01
1.400E+01	0.000E-01	1.609E+01	1.460E-01
1.570E+01	0.000E-01	1.657E+01	7.800E-02
1.600E+01	0.000E-01	1.650E+01	6.400E-02
1.770E+01	0.000E-01	1.630E+01	1.040E-01
1.800E+01	0.000E-01	1.642E+01	1.110E-01
1.970E+01	0.000E-01	1.568E+01	1.890E-01

2.070E+01	0.000E-01	1.524E+01	2.820E-01	2.200E+01	0.000E-01	1.086E+01	2.064E+00
2.139E+01	0.000E-01	1.489E+01	3.030E-01	2.269E+01	0.000E-01	1.039E+01	2.311E+00
2.200E+01	0.000E-01	1.448E+01	3.780E-01	2.330E+01	0.000E-01	9.700E+00	2.295E+00
2.251E+01	0.000E-01	1.409E+01	4.540E-01	2.381E+01	0.000E-01	9.250E+00	2.272E+00
2.320E+01	0.000E-01	1.341E+01	5.590E-01	2.450E+01	0.000E-01	8.540E+00	2.145E+00
2.367E+01	0.000E-01	1.271E+01	6.810E-01	2.497E+01	0.000E-01	7.950E+00	1.951E+00
2.407E+01	0.000E-01	1.191E+01	7.270E-01	2.537E+01	0.000E-01	7.690E+00	1.793E+00
2.440E+01	0.000E-01	1.123E+01	8.150E-01	2.570E+01	0.000E-01	7.470E+00	1.697E+00
2.466E+01	0.000E-01	1.063E+01	1.059E+00	2.596E+01	0.000E-01	7.080E+00	1.624E+00
2.488E+01	0.000E-01	1.007E+01	1.200E+00	2.618E+01	0.000E-01	6.940E+00	1.646E+00
2.505E+01	0.000E-01	9.390E+00	1.452E+00	2.635E+01	0.000E-01	6.500E+00	1.544E+00
2.518E+01	0.000E-01	8.810E+00	1.877E+00	2.648E+01	0.000E-01	6.300E+00	1.541E+00
2.530E+01	0.000E-01	8.180E+00	2.173E+00	2.660E+01	0.000E-01	6.160E+00	1.690E+00
2.540E+01	0.000E-01	7.300E+00	2.456E+00	2.670E+01	0.000E-01	5.330E+00	1.779E+00
2.546E+01	0.000E-01	6.570E+00	2.753E+00	2.676E+01	0.000E-01	5.110E+00	1.906E+00
2.550E+01	0.000E-01	5.870E+00	2.609E+00	2.680E+01	0.000E-01	4.600E+00	1.898E+00
2.553E+01	0.000E-01	5.530E+00	2.395E+00	2.683E+01	0.000E-01	3.990E+00	1.552E+00
2.556E+01	0.000E-01	4.710E+00	1.993E+00	2.686E+01	0.000E-01	3.440E+00	1.368E+00
2.558E+01	0.000E-01	4.090E+00	1.906E+00	2.688E+01	0.000E-01	2.790E+00	1.188E+00
2.560E+01	0.000E-01	3.260E+00	1.362E+00				

CORE4 5/28/81 X=400 CM TEMP=81
42

FL760=CURV6+CURV7 5/81
X=760 CM W=27.0 CM TEMP=81
48

Y CM	Z CM	(U) CM/S	(U'*U')	Y CM	Z CM	(U) CM/S	(U'*U')
				2.000E+00	-2.000E+01	1.179E+01	1.074E+00
				4.000E+00	-2.000E+01	1.355E+01	8.050E-01
1.200E-01	0.000E-01	4.580E+00	2.567E+00	2.000E+00	-1.800E+01	1.182E+01	1.003E+00
1.400E-01	0.000E-01	5.680E+00	3.662E+00	4.000E+00	-1.800E+01	1.348E+01	7.280E-01
1.700E-01	0.000E-01	7.330E+00	4.063E+00	2.000E+00	-1.600E+01	1.177E+01	9.730E-01
2.000E-01	0.000E-01	7.960E+00	4.407E+00	4.000E+00	-1.600E+01	1.354E+01	7.490E-01
2.400E-01	0.000E-01	9.150E+00	4.440E+00	2.000E+00	-1.400E+01	1.193E+01	9.890E-01
3.000E-01	0.000E-01	1.036E+01	4.281E+00	4.000E+00	-1.400E+01	1.352E+01	6.960E-01
4.000E-01	0.000E-01	1.168E+01	3.627E+00	2.000E+00	-1.200E+01	1.187E+01	9.770E-01
5.200E-01	0.000E-01	1.252E+01	3.518E+00	4.000E+00	-1.200E+01	1.359E+01	7.880E-01
6.500E-01	0.000E-01	1.332E+01	3.179E+00	2.000E+00	-1.000E+01	1.178E+01	1.019E+00
8.200E-01	0.000E-01	1.347E+01	2.860E+00	4.000E+00	-1.000E+01	1.354E+01	7.430E-01
1.040E+00	0.000E-01	1.406E+01	2.402E+00	2.000E+00	-8.000E+00	1.181E+01	9.820E-01
1.300E+00	0.000E-01	1.448E+01	2.002E+00	4.000E+00	-8.000E+00	1.337E+01	7.800E-01
1.630E+00	0.000E-01	1.460E+01	1.708E+00	2.000E+00	-6.000E+00	1.174E+01	9.740E-01
2.030E+00	0.000E-01	1.495E+01	1.366E+00	4.000E+00	-6.000E+00	1.340E+01	7.990E-01
2.580E+00	0.000E-01	1.479E+01	1.343E+00	2.000E+00	-4.000E+00	1.167E+01	1.035E+00
3.190E+00	0.000E-01	1.506E+01	1.037E+00	4.000E+00	-4.000E+00	1.341E+01	7.100E-01
3.700E+00	0.000E-01	1.517E+01	9.060E-01	2.000E+00	-2.000E+00	1.161E+01	8.800E-01
4.310E+00	0.000E-01	1.515E+01	9.380E-01	4.000E+00	-2.000E+00	1.327E+01	8.570E-01
5.000E+00	0.000E-01	1.527E+01	9.360E-01	2.000E+00	0.000E-01	1.170E+01	9.900E-01
6.000E+00	0.000E-01	1.524E+01	9.930E-01	4.000E+00	0.000E-01	1.341E+01	7.740E-01
8.000E+00	0.000E-01	1.558E+01	8.330E-01	2.000E+00	2.000E+00	1.169E+01	9.130E-01
1.000E+01	0.000E-01	1.584E+01	6.310E-01	4.000E+00	2.000E+00	1.331E+01	7.570E-01
1.200E+01	0.000E-01	1.599E+01	4.220E-01	2.000E+00	4.000E+00	1.160E+01	9.280E-01
1.300E+01	0.000E-01	1.582E+01	5.210E-01	4.000E+00	4.000E+00	1.327E+01	8.200E-01
1.400E+01	0.000E-01	1.582E+01	2.550E-01	2.000E+00	6.000E+00	1.164E+01	9.760E-01
1.500E+01	0.000E-01	1.566E+01	3.080E-01	4.000E+00	6.000E+00	1.343E+01	7.250E-01
1.700E+01	0.000E-01	1.497E+01	3.780E-01	2.000E+00	8.000E+00	1.160E+01	9.550E-01
1.900E+01	0.000E-01	1.353E+01	9.940E-01	4.000E+00	8.000E+00	1.326E+01	7.970E-01
2.100E+01	0.000E-01	1.151E+01	1.595E+00	2.000E+00	1.000E+01	1.183E+01	1.012E+00

```
4.000E+00   1.000E+01   1.324E+01   8.300E-01      1.550E+01   2.000E+00   1.474E+01
2.000E+00   1.200E+01   1.161E+01   9.560E-01      1.900E+01   2.000E+00   1.458E+01
4.000E+00   1.200E+01   1.329E+01   8.110E-01      8.000E+00   0.000E-01   1.488E+01
2.000E+00   1.400E+01   1.164E+01   9.190E-01      1.150E+01   0.000E-01   1.479E+01
4.000E+00   1.400E+01   1.321E+01   8.030E-01      1.550E+01   0.000E-01   1.476E+01
2.000E+00   1.600E+01   1.154E+01   9.460E-01      1.900E+01   0.000E-01   1.455E+01
4.000E+00   1.600E+01   1.322E+01   7.580E-01      8.000E+00  -2.000E+00   1.490E+01
2.000E+00   1.800E+01   1.161E+01   9.380E-01      1.150E+01  -2.000E+00   1.480E+01
4.000E+00   1.800E+01   1.328E+01   6.780E-01      1.550E+01  -2.000E+00   1.477E+01
2.000E+00   2.000E+01   1.165E+01   9.670E-01      1.900E+01  -2.000E+00   1.462E+01
4.000E+00   2.000E+01   1.324E+01   7.590E-01      8.000E+00  -4.000E+00   1.486E+01
                                                   1.150E+01  -4.000E+00   1.477E+01
CORE1   5/13/81   X=400 CM                         1.550E+01  -4.000E+00   1.474E+01
T=60 SEC   TEMP=76                                 1.900E+01  -4.000E+00   1.458E+01
84                                                 8.000E+00  -6.000E+00   1.489E+01
   Y CM       Z CM      <U> CM/S                    1.150E+01  -6.000E+00   1.481E+01
8.000E+00   2.000E+01   1.481E+01                  1.550E+01  -6.000E+00   1.474E+01
1.150E+01   2.000E+01   1.483E+01                  1.900E+01  -6.000E+00   1.454E+01
1.550E+01   2.000E+01   1.470E+01                  8.000E+00  -8.000E+00   1.488E+01
1.900E+01   2.000E+01   1.466E+01                  1.150E+01  -8.000E+00   1.473E+01
8.000E+00   1.800E+01   1.489E+01                  1.550E+01  -8.000E+00   1.473E+01
1.150E+01   1.800E+01   1.479E+01                  1.900E+01  -8.000E+00   1.450E+01
1.550E+01   1.800E+01   1.471E+01                  8.000E+00  -1.000E+01   1.492E+01
1.900E+01   1.800E+01   1.459E+01                  1.150E+01  -1.000E+01   1.476E+01
8.000E+00   1.600E+01   1.488E+01                  1.550E+01  -1.000E+01   1.472E+01
1.150E+01   1.600E+01   1.480E+01                  1.900E+01  -1.000E+01   1.454E+01
1.550E+01   1.600E+01   1.470E+01                  8.000E+00  -1.200E+01   1.487E+01
1.900E+01   1.600E+01   1.463E+01                  1.150E+01  -1.200E+01   1.479E+01
8.000E+00   1.400E+01   1.485E+01                  1.550E+01  -1.200E+01   1.472E+01
1.150E+01   1.400E+01   1.480E+01                  1.900E+01  -1.200E+01   1.456E+01
1.550E+01   1.400E+01   1.469E+01                  8.000E+00  -1.400E+01   1.486E+01
1.900E+01   1.400E+01   1.459E+01                  1.150E+01  -1.400E+01   1.480E+01
8.000E+00   1.200E+01   1.487E+01                  1.550E+01  -1.400E+01   1.473E+01
1.150E+01   1.200E+01   1.479E+01                  1.900E+01  -1.400E+01   1.458E+01
1.550E+01   1.200E+01   1.472E+01                  8.000E+00  -1.600E+01   1.493E+01
1.900E+01   1.200E+01   1.460E+01                  1.150E+01  -1.600E+01   1.478E+01
8.000E+00   1.000E+01   1.483E+01                  1.550E+01  -1.600E+01   1.475E+01
1.150E+01   1.000E+01   1.480E+01                  1.900E+01  -1.600E+01   1.446E+01
1.550E+01   1.000E+01   1.474E+01                  8.000E+00  -1.800E+01   1.492E+01
1.900E+01   1.000E+01   1.462E+01                  1.150E+01  -1.800E+01   1.477E+01
8.000E+00   8.000E+00   1.491E+01                  1.550E+01  -1.800E+01   1.475E+01
1.150E+01   8.000E+00   1.480E+01                  1.900E+01  -1.800E+01   1.444E+01
1.550E+01   8.000E+00   1.473E+01                  8.000E+00  -2.000E+01   1.488E+01
1.900E+01   8.000E+00   1.460E+01                  1.150E+01  -2.000E+01   1.479E+01
8.000E+00   6.000E+00   1.487E+01                  1.550E+01  -2.000E+01   1.474E+01
1.150E+01   6.000E+00   1.481E+01                  1.900E+01  -2.000E+01   1.453E+01
1.550E+01   6.000E+00   1.472E+01
1.900E+01   6.000E+00   1.459E+01
8.000E+00   4.000E+00   1.485E+01      CORE2   5/25/81   THETA=30   TEMP=81
1.150E+01   4.000E+00   1.477E+01          105
1.550E+01   4.000E+00   1.471E+01         Y CM       Z CM      <U> CM/S    <U'*U'>
1.900E+01   4.000E+00   1.457E+01      2.000E+00  -2.000E+01   1.141E+01   1.528E+00
8.000E+00   2.000E+00   1.488E+01      4.000E+00  -2.000E+01   1.270E+01   1.542E+00
1.150E+01   2.000E+00   1.479E+01      8.000E+00  -2.000E+01   1.501E+01   4.080E-01
                                       1.200E+01  -2.000E+01   1.571E+01   2.500E-02
```

Y CM	Z CM	<U> CM/S	<U'*U'>
1.600E+01	-2.000E+01	1.596E+01	8.200E-02
2.000E+00	-1.800E+01	1.153E+01	1.403E+00
4.000E+00	-1.800E+01	1.267E+01	1.697E+00
8.000E+00	-1.800E+01	1.490E+01	4.850E-01
1.200E+01	-1.800E+01	1.577E+01	2.200E-02
1.600E+01	-1.800E+01	1.601E+01	5.800E-02
2.000E+00	-1.600E+01	1.140E+01	1.603E+00
4.000E+00	-1.600E+01	1.251E+01	1.592E+00
8.000E+00	-1.600E+01	1.499E+01	4.640E-01
1.200E+01	-1.600E+01	1.578E+01	1.900E-02
1.600E+01	-1.600E+01	1.604E+01	7.300E-02
2.000E+00	-1.400E+01	1.137E+01	1.583E+00
4.000E+00	-1.400E+01	1.260E+01	1.615E+00
8.000E+00	-1.400E+01	1.506E+01	3.680E-01
1.200E+01	-1.400E+01	1.580E+01	1.800E-02
1.600E+01	-1.400E+01	1.604E+01	7.180E-02
2.000E+00	-1.200E+01	1.144E+01	1.510E+00
4.000E+00	-1.200E+01	1.267E+01	1.567E+00
8.000E+00	-1.200E+01	1.504E+01	4.170E-01
1.200E+01	-1.200E+01	1.585E+01	1.800E-02
1.600E+01	-1.200E+01	1.607E+01	6.200E-02
2.000E+00	-1.000E+01	1.150E+01	1.475E+00
4.000E+00	-1.000E+01	1.269E+01	1.576E+00
8.000E+00	-1.000E+01	1.497E+01	4.550E-01
1.200E+01	-1.000E+01	1.578E+01	1.800E-02
1.600E+01	-1.000E+01	1.606E+01	7.000E-02
2.000E+00	-8.000E+00	1.150E+01	1.548E+00
4.000E+00	-8.000E+00	1.277E+01	1.504E+00
8.000E+00	-8.000E+00	1.505E+01	4.390E-01
1.200E+01	-8.000E+00	1.579E+01	2.000E-02
1.600E+01	-8.000E+00	1.603E+01	8.900E-02
2.000E+00	-6.000E+00	1.158E+01	1.435E+00
4.000E+00	-6.000E+00	1.264E+01	1.563E+00
8.000E+00	-6.000E+00	1.505E+01	4.750E-01
1.200E+01	-6.000E+00	1.579E+01	2.000E-02
1.600E+01	-6.000E+00	1.602E+01	8.800E-02
2.000E+00	-4.000E+00	1.154E+01	1.483E+00
4.000E+00	-4.000E+00	1.278E+01	1.531E+00
8.000E+00	-4.000E+00	1.512E+01	3.500E-01
1.200E+01	-4.000E+00	1.585E+01	1.900E-02
1.600E+01	-4.000E+00	1.6?9E+01	7.200E-02
2.000E+00	-2.000E+00	1.139E+01	1.534E+00
4.000E+00	-2.000E+00	1.268E+01	1.575E+00
3.000E+00	-2.000E+00	1.501E+01	4.570E-01
1.200E+01	-2.000E+00	1.584E+01	1.600E-02
1.600E+01	-2.000E+00	1.616E+01	6.900E-02
2.000E+00	0.000E-01	1.134E+01	1.654E+00
4.000E+00	0.000E-01	1.256E+01	1.631E+00
8.000E+00	0.000E-01	1.502E+01	4.530E-01
1.200E+01	0.000E-01	1.582E+01	2.300E-02
1.600E+01	0.000E-01	1.609E+01	6.700E-02
2.000E+00	2.000E+00	1.131E+01	1.366E+00
4.000E+00	2.000E+00	1.262E+01	1.621E+00
8.000E+00	2.000E+00	1.499E+01	4.110E-01
1.200E+01	2.000E+00	1.585E+01	2.000E-02
1.600E+01	2.000E+00	1.621E+01	5.000E-02
2.000E+00	4.000E+00	1.129E+01	1.377E+00
4.000E+00	4.000E+00	1.258E+01	1.629E+00
8.000E+00	4.000E+00	1.497E+01	4.960E-01
1.200E+01	4.000E+00	1.585E+01	2.500E-02
1.600E+01	4.000E+00	1.612E+01	7.700E-02
2.000E+00	6.000E+00	1.157E+01	1.472E+00
4.000E+00	6.000E+00	1.262E+01	1.516E+00
8.000E+00	6.000E+00	1.496E+01	4.600E-01
1.200E+01	6.000E+00	1.585E+01	2.800E-02
1.600E+01	6.000E+00	1.612E+01	6.300E-02
2.000E+00	8.000E+00	1.140E+01	1.613E+00
4.000E+00	8.000E+00	1.261E+01	1.702E+00
8.000E+00	8.000E+00	1.484E+01	6.010E-01
1.200E+01	8.000E+00	1.586E+01	2.500E-02
!.600E+01	8.000E+00	1.616E+01	6.700E-02
2.000E+00	1.000E+01	1.146E+01	1.457E+00
4.000E+00	1.000E+01	1.260E+01	1.598E+00
8.000E+00	1.000E+01	1.486E+01	5.620E-01
1.200E+01	1.000E+01	1.584E+01	2.400E-02
1.600E+01	1.000E+01	1.614E+01	5.000E-02
2.000E+00	1.200E+01	1.146E+01	1.468E+00
4.000E+00	1.200E+01	1.264E+01	1.484E+00
8.000E+00	1.200E+01	1.485E+01	5.770E-01
1.200E+01	1.200E+01	1.580E+01	2.600E-02
1.600E+01	1.200E+01	1.617E+01	5.900E-02
2.000E+00	1.400E+01	1.136E+01	1.435E+00
4.000E+00	1.400E+01	1.244E+01	1.458E+00
8.000E+00	1.400E+01	1.475E+01	6.240E-01
1.200E+01	1.400E+01	1.581E+01	2.400E-02
1.600E+01	1.400E+01	1.612E+01	4.400E-02
2.000E+00	1.600E+01	1.129E+01	1.454E+00
4.000E+00	1.600E+01	1.251E+01	1.560E+00
8.000E+00	1.600E+01	1.474E+01	7.010E-01
1.200E+01	1.600E+01	1.585E+01	2.900E-02
1.600E+01	1.600E+01	1.614E+01	5.800E-02
2.000E+00	1.800E+01	1.105E+01	1.426E+00
4.000E+00	1.800E+01	1.210E+01	1.547E+00
8.000E+00	1.800E+01	1.453E+01	8.520E-01
1.200E+01	1.800E+01	1.584E+01	2.500E-02
1.600E+01	1.800E+01	1.618E+01	6.100E-02
2.000E+00	2.000E+01	1.106E+01	1.394E+00
4.000E+00	2.000E+01	1.211E+01	1.599E+00
8.000E+00	2.000E+01	1.454E+01	7.970E-01
1.200E+01	2.000E+01	1.588E+01	2.900E-02
1.600E+01	2.000E+01	1.616E+01	4.400E-02

CORE3 5/26/81 THETA=75 TEMP=81
105

Y CM	Z CM	<U> CM/S	<U'*U'>
2.000E+00	-2.000E+01	1.316E+01	1.685E+00
4.000E+00	-2.000E+01	1.419E+01	1.456E+00
8.000E+00	-2.000E+01	1.547E+01	8.318E-01

1.200E+01	-2.000E+01	1.615E+01	1.380E-01	1.600E+01	0.000E-01	1.657E+01	6.400E-02
1.600E+01	-2.000E+01	1.572E+01	1.910E-01	2.000E+00	2.000E+00	1.325E+01	1.759E+00
2.000E+00	-1.800E+01	1.313E+01	1.911E+00	4.000E+00	2.000E+00	1.380E+01	1.449E+00
4.000E+00	-1.800E+01	1.388E+01	1.655E+00	8.000E+00	2.000E+00	1.502E+01	1.054E+00
8.000E+00	-1.800E+01	1.540E+01	9.020E-01	1.200E+01	2.000E+00	1.604E+01	4.400E-01
1.200E+01	-1.800E+31	1.635E+01	1.880E-01	1.600E+01	2.000E+00	1.673E+01	6.700E-02
1.600E+01	-1.800E+01	1.586E+01	1.720E-01	2.000E+00	4.000E+00	1.297E+01	1.713E+00
2.000E+00	-1.600E+01	1.310E+01	1.731E+00	4.000E+00	4.000E+00	1.359E+01	1.615E+00
4.000E+00	-1.600E+01	1.359E+01	1.547E+00	8.000E+00	4.000E+00	1.474E+01	1.167E+00
8.000E+00	-1.600E+01	1.523E+01	9.800E-01	1.200E+01	4.000E+00	1.605E+01	3.920E-01
1.200E+01	-1.600E+01	1.635E+01	2.730E-01	1.600E+01	4.000E+00	1.667E+01	6.400E-02
1.600E+01	-1.600E+01	1.597E+01	1.620E-01	2.000E+00	6.000E+00	1.277E+01	1.649E+00
2.000E+00	-1.400E+01	1.290E+01	1.857E+00	4.000E+00	6.000E+00	1.342E+01	1.618E+00
4.000E+00	-1.400E+01	1.379E+01	1.360E+00	8.000E+00	6.000E+00	1.470E+01	1.080E+00
8.000E+00	-1.400E+01	1.511E+01	1.151E+00	1.200E+01	6.000E+00	1.590E+01	5.230E-01
1.200E+01	-1.400E+01	1.622E+01	2.750E-01	1.600E+01	6.000E+00	1.663E+01	8.700E-02
1.600E+01	-1.400E+01	1.623E+01	1.400E-01	2.000E+00	8.000E+00	1.258E+01	1.536E+00
2.000E+00	-1.200E+01	1.280E+01	1.726E+00	4.000E+00	8.000E+00	1.340E+01	1.575E+00
4.000E+00	-1.200E+01	1.360E+01	1.516E+00	8.000E+00	8.000E+00	1.463E+01	1.342E+00
8.000E+00	-1.200E+01	1.489E+01	1.179E+00	1.200E+01	8.000E+00	1.584E+01	5.920E-01
1.200E+01	-1.200E+01	1.620E+01	2.080E-01	1.600E+01	8.000E+00	1.661E+01	7.700E-02
1.600E+01	-1.200E+01	1.625E+01	1.390E-01	2.000E+00	1.000E+01	1.251E+01	1.943E+00
2.000E+00	-1.000E+01	1.325E+01	1.715E+00	4.000E+00	1.000E+01	1.324E+01	1.596E+00
4.000E+00	-1.000E+01	1.356E+01	1.523E+00	8.000E+00	1.000E+01	1.462E+01	1.480E+00
8.000E+00	-1.000E+01	1.490E+01	1.072E+00	1.200E+01	1.000E+01	1.597E+01	6.450E-01
1.200E+01	-1.000E+01	1.610E+01	4.180E-01	1.600E+01	1.000E+01	1.668E+01	9.200E-02
1.600E+01	-1.000E+01	1.630E+01	1.170E-01	2.000E+00	1.200E+01	1.255E+01	1.665E+00
2.000E+00	-8.000E+00	1.298E+01	1.571E+00	4.000E+00	1.200E+01	1.324E+01	1.534E+00
4.000E+00	-8.000E+00	1.362E+01	1.563E+00	8.000E+00	1.200E+01	1.461E+01	1.266E+00
8.000E+00	-8.000E+00	1.494E+01	1.155E+00	1.200E+01	1.200E+01	1.584E+01	5.920E-01
1.200E+01	-8.000E+00	1.619E+01	3.000E-01	1.600E+01	1.200E+01	1.672E+01	1.100E-01
1.600E+01	-8.000E+00	1.641E+01	1.090E-01	2.000E+00	1.400E+01	1.260E+01	1.858E+00
2.000E+00	-6.000E+00	1.290E+01	1.664E+00	4.000E+00	1.400E+01	1.333E+01	1.498E+00
4.000E+00	-6.000E+00	1.365E+01	1.503E+00	8.000E+00	1.400E+01	1.433E+01	1.364E+00
8.000E+00	-6.000E+00	1.489E+01	1.134E+00	1.200E+01	1.400E+01	1.570E+01	8.650E-01
1.200E+01	-6.000E+00	1.615E+01	3.510E-01	1.600E+01	1.400E+01	1.677E+01	9.900E-02
1.600E+01	-6.000E+00	1.656E+01	9.300E-02	2.000E+00	1.600E+01	1.252E+01	1.792E+00
2.000E+00	-4.000E+00	1.307E+01	1.601E+00	4.000E+00	1.600E+01	1.293E+01	1.778E+00
4.000E+00	-4.000E+00	1.358E+01	1.472E+00	8.000E+00	1.600E+01	1.435E+01	1.345E+00
8.000E+00	-4.000E+00	1.518E+01	1.028E+00	1.200E+01	1.600E+01	1.559E+01	9.100E-01
1.200E+01	-4.000E+00	1.611E+01	2.980E-01	1.600E+01	1.600E+01	1.661E+01	1.580E-01
1.600E+01	-4.000E+00	1.661E+01	8.500E-02	2.000E+00	1.800E+01	1.218E+01	1.792E+00
2.000E+00	-2.000E+00	1.290E+01	1.648E+00	4.000E+00	1.800E+01	1.292E+01	1.719E+00
4.000E+00	-2.000E+00	1.391E+01	1.445E+00	8.000E+00	1.800E+01	1.414E+01	1.482E+00
8.000E+00	-2.000E+00	1.499E+01	1.103E+00	1.200E+01	1.800E+01	1.567E+01	8.960E-01
1.200E+01	-2.000E+00	1.612E+01	3.350E-01	1.600E+01	1.800E+01	1.655E+01	1.810E-01
1.600E+01	-2.000E+00	1.660E+01	7.100E-02	2.000E+00	2.000E+01	1.215E+01	1.827E+00
2.000E+00	0.000E-01	1.289E+01	1.616E+00	4.000E+00	2.000E+01	1.301E+01	1.562E+00
4.000E+00	0.000E-01	1.356E+01	1.387E+00	8.000E+00	2.000E+01	1.419E+01	1.548E+00
8.000E+00	0.000E-01	1.488E+01	1.081E+00	1.200E+01	2.000E+01	1.559E+01	9.660E-01
1.200E+01	0.000E-01	1.617E+01	3.450E-01	1.600E+01	2.000E+01	1.666E+01	2.260E-01

ATE
ME